Aus dem Departement für Physik
Universität Freiburg (Schweiz)

Magnetic Induction in High-T_c Superconductor / Ferromagnet Heterostructures

INAUGURAL-DISSERTATION

zur Erlangung der Würde eines
Doctor rerum naturalium
der Mathematisch-Naturwissenschaftlichen Fakultät
der Universität Freiburg in der Schweiz

vorgelegt von

Justin Hoppler

aus

Winterthur (Schweiz)

N° of Thesis: 1638
Uniprint
2009

Von der Mathematisch-Naturwissenschaftlichen Fakultät der Universität Freiburg in der Schweiz angenommen, auf Antrag von

Prof. Dr. Antoine Weis (Präsident der Jury),
Prof. Dr. Dionys Baeriswyl (Gutachter),
Dr. Jochen Stahn (externer Gutachter),
PD Dr. Christof Niedermayer (externer Gutachter) und
Prof. Dr. Christian Bernhard (Leiter der Dissertation).

Freiburg, den 15. Juni 2009

Leiter der Dissertation:

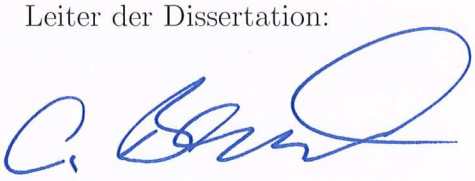

Prof. Dr. Christian Bernhard

Dekan:

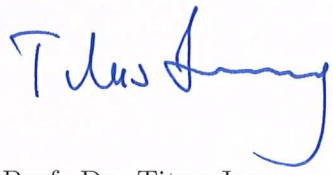

Prof. Dr. Titus Jenny

Abstract

The magnetic induction in superlattices comprising thin layers of the high-T_c superconductor $YBa_2Cu_3O_7$ (YBCO) and the ferromagnet $La_{2/3}Ca_{1/3}MnO_3$ (LCMO) has been investigated by polarised neutron reflectometry measurements. The data provide evidence for a surprisingly strong mutual interaction of the superconducting and the ferromagnetic order parameters. In the region of the interfaces a deviation of the magnetic induction depth profile from the structural depth profile has been observed. Furthermore, a coupling of the magnetisation in the ferromagnetic layers through the superconducting layers has been found. The most pronounced coupling phenomenon has been observed in samples, where underdoped YBCO ($Y_{0.6}Pr_{0.4}Ba_2Cu_3O_7$) was substituted for optimally doped YBCO. There, below the superconducting phase transition temperature T_{sc} a giant modulation of the magnetic induction depth profile evolves. This coupling of the ferromagnetic layers depends sensitively on the strain conditions in the superlattices. Supplementary hard x-ray scattering measurements revealed that the structural phase transitions in the (001)-oriented $SrTiO_3$ (STO) substrates lead to an extrinsic strain pattern in the superlattices. This strain modifies most likely the energy levels of the nearly degenerate electronic states in LCMO and enables or disables the observed coupling mechanisms.

The deviation of the magnetic induction depth profile from the structural one evolves below $T' \approx 120$ - 150 K and is confined to a region of about 1 - 2 nm around the interfaces. Its occurrence is independent of the individual layer thickness in the superlattices. Most likely, it consists of a reduced magnetic moment on the LCMO side of the interfaces and of a ferromagnetic moment induced on the YBCO side of the interfaces. The latter is oriented antiparallel to the moment in the LCMO layers and amounts to less than $0.2\,\mu_B$ per Cu atom. Its occurrence may be related to a precursor superconductivity or to a Cu-O-Mn super exchange which couples the spins of the Cu-atoms and the Mn-atoms antiparallel through the interfaces. The reduced magnetic moment on the LCMO side of the interfaces may be caused by a coupling of the ferromagnetic order to a precursor superconductivity, a charge transfer across the interfaces, a change in the oxygen stochiometry or a strain due to a small lateral lattice mismatch with the YBCO layers.

A coupling of the ferromagnetic layers through the superconducting layers has been observed during the magnetisation reversal process. In the sample plane, the magnetisation is segregated into zones with an extent of at least several tens of micrometers. Within each such zone, the magnetisation reverses in most, if not in all layers at the same time. Throughout the sample, it reverses successively in one zone after the other. This is a remarkable result, since LCMO is known to segregate into domains in a ferromagnetic state and domains in a non-magnetic or antiferromagnetic state. These domains have a diameter of some hundred nanometers, which is much less than the lateral extent of the observed zones. Thus, the magnetic domains seem to be laterally coupled within the LCMO layers on the area of one zone. In addition, they are vertically coupled from one LCMO layer to the next through the YBCO layers. The segregation of the magnetisation into such large zones is most likely induced extrinsically by the STO substrate, which undergoes a structural phase transition at $T_{STO}^{II} \approx 65$ K. Below this temperature, crystal-

lites with a rhombohedral structure evolve in the otherwise tetragonal crystal matrix. They lead to a stress which is relaxed by a bending of the substrate and the formation of anisotropic surface facets which are tilted by up to 0.5° with respect to each other. Along their shorter extent, they have a minimum length of several tens of micrometers. Due to the heteroepitaxial growth of the superlattice on the substrate surface, the extrinsic strain conditions will be homogeneous on the surface facets. At the borders of the facets, there will be a distortion in the structural properties in the substrate which is most likely passed to the superlattice. Therefore, it is conceivable that there is a strain pattern in the superlattice which follows the facet's boundaries and segregates the magnetisation laterally into the observed zones. Since the measurements have been performed at 5 K only, it is so far unclear, whether the observed vertical coupling of the ferromagnetic layers is yielded by superconductivity, by dipolar fields originating from the interface roughness or by a more exotic phenomenon like for example a spin density wave in the YBCO layers.

A coupling of the ferromagnetic layers through the superconducting ones has also been observed, if underdoped YBCO was substituted for optimally doped YBCO. Then, a modulation of the magnetic moment from one LCMO layer to the next occurs below the superconducting phase transition temperature $T_{\mathrm{sc}} \approx 40\,\mathrm{K}$. This modulation is superposed to the depth profile of the magnetic induction above T_{sc} and most often exhibits a periodicity of two YBCO / LCMO double layers. Supplermentary stress dependent measurements revealed that a uniaxial pressure of at least 400 kPa is required to be applied laterally on the substrate during the cooling for the modulation to occur. Even then, the modulation only evolves on some of the surface facets formed by the substrate. This implies that very specific stress conditions are necessary to enable the modulation. Most likely, the pressure applied to the substrate either aligns the crystallites with rhombohedral structure that evolve below $T_{\mathrm{STO}}^{\mathrm{II}}$ or it increases their volume fraction in the substrate. Only then, the subtle strain conditions are fulfilled which are necessary for the modulation. These observations lead to the conclusion that the modulation is related to the highly versatile electronic and magnetic properties of LCMO. It is conceivable that the specific strain conditions modify the energy levels of the electronic states close to the ground state and enable the superconductivity to cause the modulation in the magnetic induction depth profile.

Zusammenfassung

Die magnetische Induktion in Übergittern bestehend aus dem hochtemperatur Supraleiter $YBa_2Cu_3O_7$ (YBCO) und dem Ferromagneten $La_{2/3}Ca_{1/3}MnO_3$ (LCMO) wurde mittels Reflektometriemessungen mit polarisierten Neutronen untersucht. Dabei wurde eine erstaunlich grosse gegenseitige Beeinflussung der Ordnungsparameter des Supraleiters und des Ferromagneten beobachtet. Diese äusserte sich einerseits durch eine Abweichung des Tiefenprofils der magnetischen Induktion vom strukturellen Tiefenprofil in der Grenzflächenregion zwischen den beiden Materialien und andererseits durch eine Kopplung der Magnetisierung der ferromagnetischen Schichten durch die Supraleiterschichten hindurch. Die stärkste Kopplung wurde in Proben beobachtet, in welchen die Schichten mit optimal dotiertem YBCO durch unterdotiertes YBCO ($Y_{0.6}Pr_{0.4}Ba_2Cu_3O_7$) ersetzt sind. In diesen Proben setzt unterhalb der supraleitenden Phasenübergangstemperatur T_{sc} eine starke Modulierung des Tiefenprofils der magnetischen Induktion ein, welche empfindlich von den Stressverhältnissen in den Übergittern abhängt. Zusätzliche Streuexperimente mit harten Röntgenstrahlen haben gezeigt, dass die strukturellen Phasenübergänge der $SrTiO_3$ (STO) Substrate mit (001)-Orientierung zu einem Stress in den Übergittern führen. Dieser Stress verändert höchstwahrscheinlich die Energieniveaus der fast entarteten elektronischen Zustände im LCMO und ermöglicht oder verhindert so die beobachteten Kopplungsmechanismen.

Das Tiefenprofil der magnetischen Induktion weicht unterhalb von $T' \approx 120$ - 150 K vom strukturellen Tiefenprofil ab. Diese Abweichung ist auf eine Region von 1 - 2 nm beidseitig der Grenzflächen begrenzt und hängt nicht von den Dicken der YBCO und LCMO Schichten ab. Höchstwahrscheinlich besteht sie aus einer reduzierten Magnetisierung am Rand der LCMO Schichten und aus einem ferromagnetischen Moment, welches am Rand der YBCO Schichten induziert ist und antiparallel zur Magnetisierung der LCMO Schichten gerichtet ist. Dieses antiparallele Moment ist kleiner als $0.2\,\mu_B$ pro Cu Atom. Es kann sowohl durch eine Vorstufe des supraleitenden Zustandes, als auch durch einen Cu-O-Mn Superaustausch verursacht sein, welcher die Spins der Cu und Mn Atome beidseitig der Grenzflächen antiparallel koppelt. Das reduzierte magnetische Moment am Rand der LCMO Schichten kann durch vier verschiedene Mechanismen verursacht sein. Es könnte sich dabei um eine Kopplung der Magnetisierung an eine Vorstufe des supraleitenden Zustandes, um einen Ladungstransfer durch die Grenzflächen, um eine veränderte Sauerstoffstöchiometrie oder um Stress durch den unterschiedlichen Gitterparameter der LCMO und YBCO Schichten handeln.

Während des Magnetisierungsumkehrprozesses wurde eine Kopplung der ferromagnetischen Schichten durch die Supraleiterschichten hindurch festgestellt. Die Beobachtung war, dass die Magnetisierung der LCMO Schichten in der Probenebene in Zonen unterteilt ist, welche mindestens einige zehn Mikrometer Ausdehnung haben. Innerhalb dieser Zonen dreht die Magnetisierung in allen oder zumindest in den meisten Schichten gleichzeitig um, während sie über die Probe verteilt Zone für Zone umdreht. Dies ist ein bemerkenswertes Resultat, weil LCMO intrinsisch einen Domänenzustand aufweist, der sowohl aus ferromagnetischen als auch aus nicht-magnetischen oder antiferromagnetischen Domänen besteht.

Der Durchmesser dieser Domänen ist einige hundert Nanometer und somit wesentlich kleiner als derjenige der beobachteten Zonen. Es scheint daher, dass die Domänen innerhalb der Zonen sowohl in der Probenebene als auch von einer LCMO Schicht zur nächsten gekoppelt sind. Die Zonen sind dabei höchstwahrscheinlich extrinsisch durch einen strukturellen Phasenübergang der STO Substrate bei $T_{\mathrm{STO}}^{\mathrm{II}} \approx 65\,\mathrm{K}$ verursacht. Unterhalb dieser Temperatur entstehen in der ansonsten tetragonalen Kristallmatrix von STO Kristallite mit einer rhombohedrischen Struktur. Die Bildung dieser Kristallite führt zu einem Stress im Substrat, welcher mit einer Verbiegung des Substrates relaxiert. An der Oberfäche des Substrates entstehen dabei Oberflächenfacetten, welche um bis zu 0.5° zueinander verkippt sind. Diese Facetten sind anisotrop und besitzen eine Breite von mindestens mehreren zehn Mikrometern. Da die Übergitter heteroepitaktisch auf den Substraten gewachsen sind, ist der vom Substrat verursachte Stress in den magnetischen Schichten innerhalb der Facettenflächen homogen. An den Grenzen der Facetten ist die Ebene der Substratoberfläche jedoch gebrochen. Dieser Bruch wird an die Übergitter weitergegeben und führt zu einem Stressmuster, welches die Magnetisierung der LCMO Schichten in die beobachteten Zonen unterteilt. Da die Messungen nur bei 5 K durchgeführt wurden, ist es bis jetzt unklar, ob die vertikale Kopplung der ferromagnetischen Schichten durch die Supraleitung, die Dipolfelder aufgrund der Grenzflächenrauhigkeit oder ein exotischeres Phänomen, wie etwa eine Spindichtewelle in den YBCO Schichten, verursacht wird.

In Proben, in welchen das optimal dotierte YBCO durch unterdotiertes YBCO ersetzt ist, wurde eine weitere Form von Kopplung der ferromagnetischen Schichten durch die supraleitenden Schichten hindurch beobachtet. In diesen Proben entstand unterhalb von T_{sc} eine Modulierung im Tiefenprofil der magnetischen Induktion, welche eine sehr grosse Amplitude aufweist. Diese Modulierung besass meistens eine Periode von zwei YBCO / LCMO Doppelschichten. Zusätzliche, druckabhängige Messungen haben gezeigt, dass ein uniaxialer Mindestdruck von 400 kPa lateral am Substrat angelegt werden muss, damit die Modulierung auftritt. Selbst dann entsteht sie nur auf ein paar wenigen der Oberflächenfacetten des Substrates. Dies zeigt, dass sehr spezifische Druckverhältnisse für die Modulierung benötigt werden. Vermutlich richtet der angelegte Druck die Kristallite, welche unterhalb von $T_{\mathrm{STO}}^{\mathrm{II}}$ im Substrat entstehen, aus, oder er erhöht ihren Volumenanteil im Substrat. Nur so werden die spezifischen Stressverhältnisse im Übergitter erzeugt, welche für die magnetische Modulation benötigt werden. Diese Beobachtungen lassen darauf schliessen, dass die Modulation mit den vielfältigen elektromagnetischen Eigenschaften von LCMO zusammenhängt, da die Stressbedingungen im Übergitter die Energieniveaus der elektronischen Zustände nahe am Grundzustand verändern. Dementsprechend ermöglichen bestimmte Stressverhältnisse der Supraleitung unterhalb von T_{sc} das Hervorrufen der magnetischen Modulation.

Contents

Symbols and Abbreviations

$\|+\rangle$	spin up neutrons
$\|-\rangle$	spin down neutrons
2θ	total scattering angle ($2\theta = \alpha_\mathrm{i} + \alpha_\mathrm{f}$)
α_f	angle between the scattered beam and the sample surface
α_i	angle between the incident beam and the sample surface
$\Delta\alpha_\mathrm{f}$	divergence of the scattered beam in α_f
$\Delta\alpha_\mathrm{i}$	divergence of the incident beam in α_i
$\Delta\lambda$	uncertainty of the wavelength
$\Delta\chi_\mathrm{f}$	divergence of the incident beam perpendicular to the scattering plane
$\Delta\chi_\mathrm{f}$	divergence of the scattered beam perpendicular to the scattering plane
ΔE_ex	ferromagnetic exchange energy induced by the exchange field h
$\Delta\boldsymbol{q}$	instrument resolution in $\boldsymbol{q}$
Δq_x, Δq_y, Δq_z	components of $\Delta\boldsymbol{q}$; Δq_z may also be the distance between two intensity maxima in a reflectivity curve
ΔR	difference in resistance
λ	wavelength
μ_0	vacuum permeability ($\mu_0 = 1.256637 \cdot 10^{-6}\,\mathrm{TmA^{-1}}$)
μ_B	Bohr magneton ($\mu_\mathrm{B} = 9.274009 \cdot 10^{-24}\,\mathrm{JT^{-1}}$)
μ_n	magnetic moment of a neutron ($\mu_\mathrm{n} = 9.662 \cdot 10^{-27}\,\mathrm{Am^2}$)
ξ_FM	length scale over which the superconducting order parameter changes in a ferromagnet
$\xi_\mathrm{FM}^{\uparrow\uparrow}$	length scale over which the triplet component of the superconducting order parameter changes in a ferromagnet
ξ_N	length scale over which the superconducting order parameter changes in a normal metal
ξ_sc	length scale over which the superconducting order parameter changes in a superconductor with a reduced superconducting phase transition temperature
ξ_sc0	length scale over which the superconducting order parameter changes in a superconductor
ρ	density
$\bar{\rho}(z)$	scattering length density as a function of z
$\bar{\rho}_\mathrm{el}$	electron density

$\bar{\rho}_\mathrm{n}$	nuclear scattering length density
$\bar{\boldsymbol{\rho}}_\mathrm{m}$	magnetic scattering length density
σ	statistical roughness
τ	magnetic scattering time ($\tau \propto 1/\Delta E_\mathrm{ex}$)
ω_L	larmor precession frequency
$\mathbf{B}$, B	magnetic induction and its strength
$\mathbf{B}_\perp$	projection of the magnetic induction $\mathbf{B}$ on the plane perpendicular to $\boldsymbol{q}$
c	speed of light ($2.99792458 \cdot 10^8\,\mathrm{ms}^{-1}$)
d	thickness of a thin layer
D	diffusion coefficient
E	energy
FM	ferromagnet
h	ferromagnetic exchange field
$\hbar$	Planck's constant divided by 2π ($\hbar = 1.0545716 \cdot 10^{-34}\,\mathrm{Js}$)
H_coerc	coercive field
$\boldsymbol{H}_\mathrm{appl}$, H_appl	magnetic field applied at the position of the sample and its field strength
I	intensity
k_0	projection of the probe beam's wave vector on the surface normal of the sample
k_B	Boltzmann's constant ($k_\mathrm{B} = 1.3806504 \cdot 10^{-23}\,\mathrm{JK}^{-1}$)
$\boldsymbol{k}_\mathrm{f}$	wave vector of the scattered beam
$\boldsymbol{k}_\mathrm{i}$	wave vector of the incident beam
l_x, l_y, l_z	coherence lengths of the probe beam
LCMO	$La_{2/3}Ca_{1/3}MnO_3$
LSMO	$La_{2/3}Sr_{1/3}MnO_3$
m_n	mass of a neutron ($m_\mathrm{n} = 1.675 \cdot 10^{-27}\,\mathrm{kg}$)
N	normal metal
P	polarisation of the neutron beam
$P(x)$	probability distribution
$\boldsymbol{p}$	momentum
$\boldsymbol{q}$	momentum transfer vector
q_c	position of the edge of total reflection
q_x, q_y, q_z	x-, y- and z-component of $\boldsymbol{q}$
R	reflectivity
$R(q_z)$	reflectivity as a function of q_z
r_el	classical electron radius ($r_\mathrm{el} = 2.8179 \cdot 10^{-15}\,\mathrm{m}$)
SC	superconductor
STO	$SrTiO_3$
T	temperature
T^*	temperature, where possibly a precursor superconductivity with a short coherence length occurs
T'	temperature, where a deviation of the magnetic induction depth profile from the structural depth profile has been observed.
T_Curie	ferromagnetic phase transition temperature

T_{PG}	temperature, where the pseudogap opens in high-T_{c} superconductors
T_{sc}	superconducting phase transition temperature
T_{sc0}	superconducting phase transition temperature in a bulk superconductor
$T_{\mathrm{sc}}^{\mathrm{red}}$	reduced superconducting phase transition temperature
$T_{\mathrm{STO}}^{\mathrm{I}}$	cubic-to-tetragonal phase transition in bulk $SrTiO_3$ ($T_{\mathrm{STO}}^{\mathrm{I}} = 104\,\mathrm{K}$)
$T_{\mathrm{STO}}^{\mathrm{I'}}$	cubic-to-tetragonal phase transition in the near-surface region of $SrTiO_3$ ($T_{\mathrm{STO}}^{\mathrm{I'}} \approx 150\,\mathrm{K}$)
$T_{\mathrm{STO}}^{\mathrm{II}}$	transition temperature, below which crystallites with a rhombohedral structure evolve in the otherwise tetragonal crystal matrix of $SrTiO_3$ ($T_{\mathrm{STO}}^{\mathrm{II}} \approx 65\,\mathrm{K}$)
$T_{\mathrm{STO}}^{\mathrm{III}}$	transition temperature, below which changes of the local electric field gradients of the Ti-ions in $SrTiO_3$ have been observed with NMR ($T_{\mathrm{STO}}^{\mathrm{III}} \approx 30\,\mathrm{K}$)
YBCO	$YBa_2Cu_3O_{7-\delta}$
YPr0.4BCO	$Y_{0.6}Pr_{0.4}Ba_2Cu_3O_{7-\delta}$

1 Introduction

Ferromagnetism and superconductivity are phenomena in modern solid state physics that have been separately investigated for several decades. Even though ferromagnetism has been known already by the ancient Greeks, its origin remained a complete mystery for centuries. Only some ninety years ago, when quantum theory was being developed, the first experiments and theoretical work shined some light on it [1, 2, 3, 4, 5, 6]. Ever since, ferromagnetism has attracted a lot of attention and motivated researchers for countless studies. Different magnetic materials have been discovered and new theories have been developed [7, 8, 9]. Compared to this, superconductivity has a much shorter history: It has been discovered in 1911 by H.K. Onnes [10], soon after the liquefaction of helium became possible. Despite of intense research, it has not been understood until 1957, when a quantum mechanical theory was introduced by J. Bardeen, L.N. Cooper and J.R. Schrieffer [11]. In the following years, this formalism has been extended and different boundary conditions have been applied to it [12, 13]. In 1986, a tremendous increase of research activities on superconductivity has been triggered by the discovery of the so-called high temperature superconductors by J.G. Bednorz and K.A. Müller [14]. This hype has not ended, when towards the end of 2007 iron-based pnictides have been found to become superconducting as well [15, 16, 17].

Since 1957, the antagonistic characters of the superconducting and the ferromagnetic order parameters have been known. Nonetheless, not much attention has been paid on heterostructures comprising these two systems. The attention increased only with the technical advances that made the growth of artificial superconductor / ferromagnet multilayers possible. It increased considerably after 1986, when a non-linear behaviour of the superconducting transition temperature in dependence of the ferromagnetic layer thickness had been reported [18]. This was the motivation for several experimental and theoretical studies on conventional superconductor / ferromagnet heterostructures. Coupling phenomena have been reported like a π-phase shift of the order parameter in one superconducting layer to the order parameter in next superconducting layer or an oscillation of the superconducting phase transition temperature in dependence of the ferromagnetic layer thickness [19, 20, 21]. Common to these heterostructures was that the energy gain of the ferromagnetic ordering was much larger than the energy gain of the superconducting condensation. Thus, the influence of the ferromagnetism on the superconductivity was stronger than vice versa.

In the late 1990's, first studies on non-conventional superconductor / ferromagnet heterostructures have been reported [22, 23]. The use of high temperature superconductors and ferromagnetic manganese-oxides promised a possible application in devices due to

the high transition temperatures and the spin-injection into the superconductor enabled by the half-metallic properties of the manganese-oxides. Soon, novel proximity-induced effects were discovered that have a much larger length scale than the ones observed in conventional heterostructures [24, 25]. Subsequently, more and more studies indicated a strong mutual interaction between the superconducting and the ferromagnetic order parameters [26, 27, 28] and motivated researchers to further investigate such heterostructures.

The goal of this thesis was the in-depth investigation of the magnetic induction in $YBa_2Cu_3O_7$ / $La_{2/3}Ca_{1/3}MnO_3$ heterostructures. The depth profile of the magnetic induction was to be determined from polarised neutron reflectometry measurements and corresponding simulation calculations. A preliminarily reported deviation of the magnetic depth profile from the structural depth profile [28] and a possible coupling of the ferromagnetic layers through the superconducting $YBa_2Cu_3O_7$ layers was to be investigated in more detail. The latter was to be investigated by changing the doping of the $YBa_2Cu_3O_7$ layers and by studying the magnetisation.

During the work on this thesis, the nature of the deviation of the magnetic depth profile from the structural depth profile has been investigated in more detail. Further, a strong coupling of the ferromagnetic layers through underdoped $Y_{0.6}Pr_{0.4}Ba_2Cu_3O_7$ layers in the superconducting state has been investigated. This coupling depended strongly on extrinsic, uniaxial stress on the heterostructures that is induced by the $SrTiO_3$ substrate. The underlying structural phase transitions of the $SrTiO_3$ substrates motivated additional x-ray diffraction measurements, where the structural changes in the substrates and subsequently in the heterostructures have been determined. The coupling of the ferromagnetic layers through $YBa_2Cu_3O_7$ has been further investigated by polarised neutron reflectometry measurements during the magnetisation reversal process of a heterostructure comprising optimally doped $YBa_2Cu_3O_7$.

2 Background

In this chapter, the scientific background is presented. The involved physics is introduced in section 2.1 and the investigation method of polarised neutron reflectometry is discussed in section 2.2. A short description of the magnetometer which has been used for the sample characterisation is given in section 2.3.

2.1 Structural and Electromagnetic Properties

The physical background of this work is introduced here. In the first part, the structural and electromagnetic properties are discussed separately for each of the investigated materials. Then, some general aspects of thin layer systems and heterostructures are described and some relevant theoretical studies of proximity effects in superconductor / ferromagnet heterostructures are introduced. Finally, the various phenomena that have previously been observed by different groups on $YBa_2Cu_3O_{7-\delta}$ / $La_{2/3}Ca_{1/3}MnO_3$ heterostructure are discussed.

2.1.1 Perovskites

Perovskite is the name of the mineral calcium titanium oxide, $CaTiO_3$. It also refers to any other material with this crystal structure and the chemical formula ABX_3, where A and B are cations and X are anions that bond the cations. The B-cations are smaller than the A-cations and are located in the centre of octahedrons formed by the X-anions. The A-cations are located in the free spaces between these octahedrons (see Figure 2.3 and 2.6). Depending on the size of the A- and B-cations, the anion octahedrons are distorted and the bonding angles and distances between the anions and cations vary. This can change the electronic and magnetic properties of the material dramatically.

The term *perovskite* is sometimes also used for structures with a unit cell that is composed of several ABX_3 unit cells which comprise different cations. In the following, these structures are referred to as *perovskite-like*.

2.1.2 Properties of the Manganites

Manganese-oxides with a perovskite structure are often referred to as *manganites* in solid state physics, even though in chemistry this term is only used for salts containing MnO_x-anions. Nonetheless, the term *manganites* will be used here according to the habits in solid state physics.

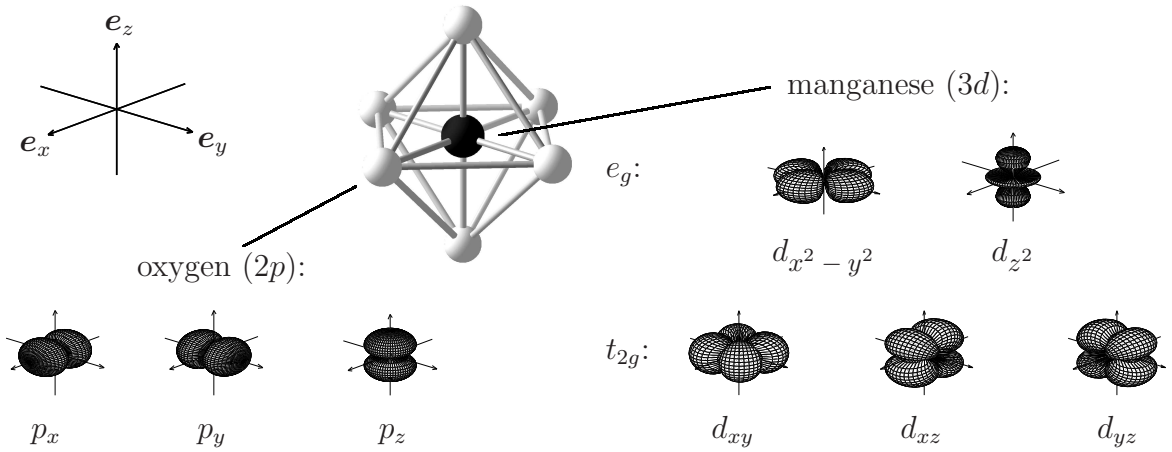

Figure 2.1: The $2p$-orbitals of oxygen and the $3d$-orbitals of manganese are responsible for the chemical bonds in the oxygen octahedron inherent to the manganites with perovskite structure. The spatial overlap of the orbitals depends on the orientation of the affected orbitals. Hence the orbital dependent Coulomb repulsion leads to a splitting of the energy levels of the five Mn $3d$-orbitals into two e_g-levels with increased energy and three t_{2g}-levels with decreased energy.

Manganites have been investigated with increasing interest after the discovery of the *colossal magnetoresistance* effect in 1993 [29]. They show a broad spectrum of electronic and magnetic properties which results from their structure (see Figure 2.3): Their chemical formula is $A_{1-x}B_x\mathrm{MnO_3}$, where A is a trivalent cation, B is a divalent cation and Mn is a trivalent or tetravalent cation. The ratio of $\mathrm{Mn^{3+}}$ to $\mathrm{Mn^{4+}}$ is tuned by the ratio x of tri- and divalent cations. The atoms are arranged in the crystal in a way that the Mn-cations are octahedrally coordinated by oxygen. These octahedrons form a lattice with the A- and B-cations in the gaps. Therefore any change in the ratio of A- and B-cations and corresponding change of the atomic radii influences the distortion of the oxygen octahedrons. Inside of the octahedrons, the Mn $3d$-orbitals overlap spatially with the oxygen $2p$-orbitals. The amount of overlapping depends on the orientation of the affected orbitals and on the distortion of the oxygen octahedrons (see Figure 2.1). It determines the Coulomb repulsion between the electrons occupying the orbitals and thus modifies the energy levels of the orbitals. In the case of undistorted oxygen octahedrons, this leads to a *crystal field splitting* of the five Mn $3d$-orbital levels into two e_g-levels with increased energy and three t_{2g}-levels with reduced energy (see Figure 2.2). In the case of three Mn $3d$-electrons ($\mathrm{Mn^{4+}}$), only the t_{2g}-levels are occupied. Due to the Hund's coupling, these electrons have parallel aligned spins. The total spin of such a $\mathrm{Mn^{4+}}$ is coupled antiparallel to the one of the next nearest $\mathrm{Mn^{4+}}$ via a small orbital overlap with the oxygen $2p$-electrons (*super exchange*) [30]. In the case of four Mn $3d$-electrons ($\mathrm{Mn^{3+}}$), the strong Hund's coupling leads to the occupation of three t_{2g}-orbitals and one e_g-orbital. It can then be energetically favourable for the crystal to stretch the oxygen octahedron along the z-axis and reduce the energy of the d_{z^2}-orbital while increasing the energy of the $d_{x^2-y^2}$-orbital (*Jahn-Teller effect*) [30].

$\mathrm{LaMnO_3}$ is the mother compound of one family of manganites with perovskite structure. It is a Mott insulator and A-type antiferromagnet with a ferromagnetic order in

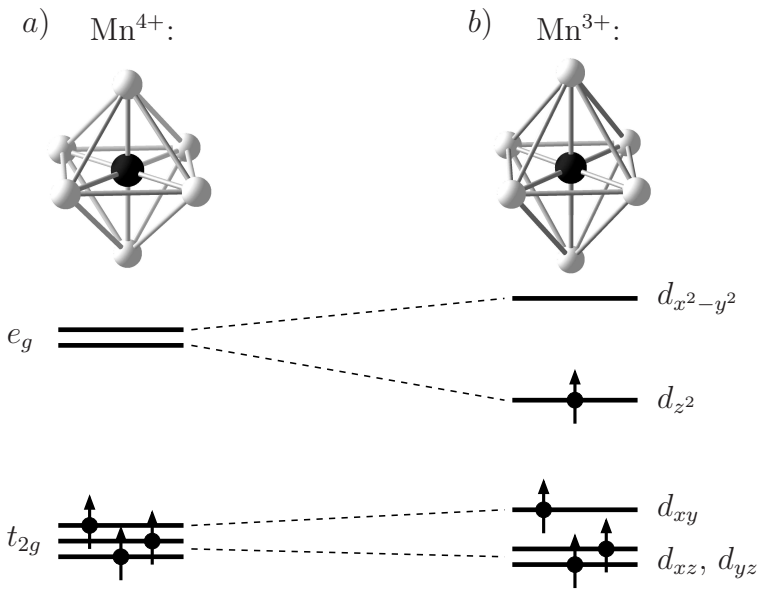

Figure 2.2: Orbital occupancies and energy levels in Mn^{4+} and Mn^{3+}: *a*) In the case of three Mn 3*d*-electrons, the t_{2g}-orbitals are filled with one electron each and the oxygen octahedron remains undistorted. *b*) In the case of four Mn 3*d*-electrons, three t_{2g}-orbitals and one e_g-orbital are filled. It can then be energetically favourable for the system to form a Jahn-Teller polaron i. e. to stretch the octahedron along the *z*-axis and subsequently modify the energy levels of the orbitals.

the *ab*-plane and an antiferromagnetic order along the *c*-axis. The Mn^{3+} are in the ionic state $t_{2g}^3\ e_g^1$ (d^4) and have a total spin of $S = 2$. The substitution of a divalent cation like Ca^{2+}, Sr^{2+} or Ba^{2+} for a fraction $0 < x < 1$ of La^{3+} results in x of the Mn ions being in the ionic state t_{2g}^3 (d^3) and having a total spin of $S = 3/2$. These Mn^{4+} are randomly distributed in the crystal and have empty e_g-levels. Due to the high-spin state of the Mn-cations and the Hund's coupling, e_g-electrons can only hop from neighbouring Mn-cations to the empty e_g-levels, if the spins of the t_{2g}-electrons at the two sites are aligned in parallel. This so-called *double exchange* mechanism gives rise to a fully spin-polarised e_g-conduction band and to a ferromagnetic order of the t_{2g}-electrons [30]. Therefore, the transition from a paramagnetic state at high temperatures to a double exchange induced ferromagnetic state at lower temperatures involves an insulator-to-metal transition at the same time. At temperatures close to the transition temperature, the resistance in such a material can change by three orders of magnitude by the simple application of an external magnetic field which aligns the spins of the t_{2g}-electrons and subsequently allows for the hopping of the e_g-electrons [29, 31]. This effect is called *colossal magnetoresistance*.

A further complication arises, if the oxygen octahedrons are tilted with respect to each other due to the ionic radii of the di- and trivalent cations. Then, the Mn e_g-orbitals and the oxygen 2*p*-orbitals are tilted with respect to each other, which reduces the hopping rate of the e_g-electrons. This partial localisation of the itinerant e_g-electrons can change the ground state from a double exchange state to a different ground state.

Several studies on $La_{1-x}B_xMnO_3$ with $B = Sr^{2+}$, Ca^{2+} and Ba^{2+} have shown that spatially separated different electronic and magnetic states coexist at the same time for a broad range of x [31, 32]. This phase separation indicates how delicate the balance between the different states close to the ground state is and how easily the ground state can be changed [33].

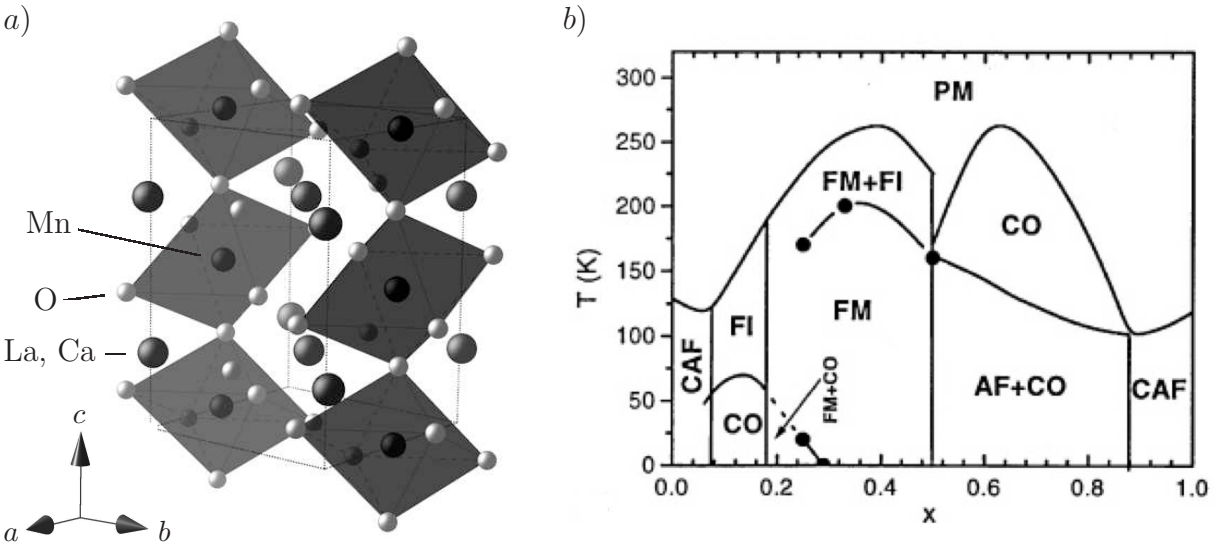

Figure 2.3: *a*): Orthorhombic unit cell of $La_{2/3}Ca_{1/3}MnO_3$. *b*) : Phase diagram of $La_{1-x}Ca_xMnO_3$. Antiferromagnetic orders are indicated by AF, while specified C-type antiferromagnetic orders are indicated by CAF. Paramagnetic metallic, ferromagnetic metallic and ferromagnetic insulating phases are indicated by PM, FM and FI, respectively. Charge ordered phases are indicated by CO. Figure *b*) has been taken from [31].

$La_{2/3}Ca_{1/3}MnO_3$

$La_{1-x}Ca_xMnO_3$ (LCMO) has an orthorhombic unit cell with the space group $Pbnm$ (Figure 2.3 *a*). Its lattice parameters are $a = 5.4683\,\text{Å}$, $b = 5.4524\,\text{Å}$ and $c = 7.7220\,\text{Å}$ [34]. It exhibits a very rich phase diagram with phases reaching from a paramagnetic insulator or a paramagnetic metal to a ferromagnetic insulator, a ferromagnetic metal and even an antiferromagnet (Figure 2.3 *b*). Because of the strong buckling of the Mn-O-Mn bonds, the e_g-electron hopping parameter and band width are reduced compared to $La_{1-x}Sr_xMnO_3$. Subsequently, the energy level of the double exchange ground state is increased in LCMO and lifted to the vicinity of the energy levels of a paramagnetic or antiferromagnetic state which is Jahn-Teller distortion stabilised and an antiferromagnetic state which is dominated by the super exchange. Accordingly, LCMO is highly susceptible to the formation of different electronic ground states and shows also tendencies towards orbital and charge ordered phases. These tendencies cannot be explained with a simple double exchange model. For a proper description of these phases, at least the introduction of the super exchange coupling is needed in addition to the double exchange [35, 36]. This way, the antiferromagnetic, charge and orbital ordered states competing with the ferromagnetic, metallic state can be taken into account.

At $x = 1/3$, LCMO is a paramagnet and has a conductivity which decreases as the temperature is lowered towards T_{Curie}. It becomes ferromagnetic at $T_{\text{Curie}} = 265\,\text{K}$, even though a phase separation into metallic and insulating domains has been observed. Only below 200 K, it becomes purely ferromagnetic metallic [32]. The saturation moment is at low temperature $3.7\,\mu_B$ per Mn ion [37].

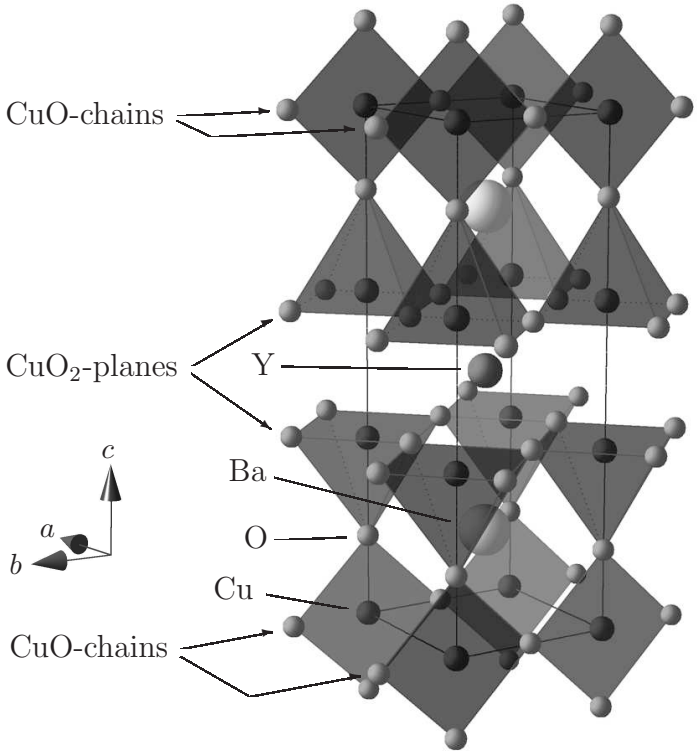

Figure 2.4: The crystal structure of $YBa_2Cu_3O_7$. One unit cell is shown together with oxygen atoms from the adjacent unit cells to illustrate the CuO_2-planes and CuO-chains. The hole-doping of the CuO_2-planes is either controlled indirectly by the number of O-vacancies in the CuO-chains or directly by replacing a fraction of the Y-ions with Pr-ions.

2.1.3 Properties of the High-T_c Superconductor $YBa_2Cu_3O_{7-\delta}$

The structure of yttrium barium copper oxide (YBCO) is a stacking of three perovskite unit cells that are oxygen deficient. Two $CuBaO_2$ or $CuBaO_{2.5}$ unit cells with one $CuYO_2$ unit cell in between form a perovskite-like structure with the stochiometry $YBa_2Cu_3O_6$ or $YBa_2Cu_3O_7$, respectively (see Figure 2.4). The resulting unit cell comprises two parallel CuO_2-planes that are oriented perpendicular to the crystallographic (001)-direction. These planes are only separated by one layer of Y-ions and thus arranged in so-called *bilayers*. The spacing between the bilayers of two neighbouring unit cells consists of two BaO-layers and one layer of CuO-chains. The variable oxygen content in $YBa_2Cu_3O_{6+x}$ is successively implemented into these CuO-chains until they are completely filled at $x = 1$. For $x < 0.36$, $YBa_2Cu_3O_{6+x}$ has a tetragonal structure and a space group $P4/mmm$, while it has an orthorhombic structure and a space group $Pmmm$ for $x \geq 0.36$. The length of its c-axis lattice parameter decreases with increasing x. For $x = 0.18$, the lattice parameters are $a = b = 3.8587\,\text{Å}$ and $c = 11.8064\,\text{Å}$. For $x = 0.96$, they are $a = 3.8227\,\text{Å}$, $b = 3.8872\,\text{Å}$ and $c = 11.6802\,\text{Å}$ [38].

The electronic and magnetic properties of $YBa_2Cu_3O_{6+x}$ depend strongly on the oxygen content x in the CuO-chains: $YBa_2Cu_3O_{6+x}$ is insulating and antiferromagnetic for $x < 0.36$, while it is superconducting for $x \geq 0.36$. Its superconducting transition temperature T_{sc} increases with increasing oxygen content until it reaches a maximum of 92 K at the so called *optimal doping* of $x = 0.92$. For this reason, $YBa_2Cu_3O_{6+x}$ is often denoted by the chemical formula $YBa_2Cu_3O_{7-\delta}$, where δ is the oxygen deficiency of optimal doping as compared to $YBa_2Cu_3O_7$.

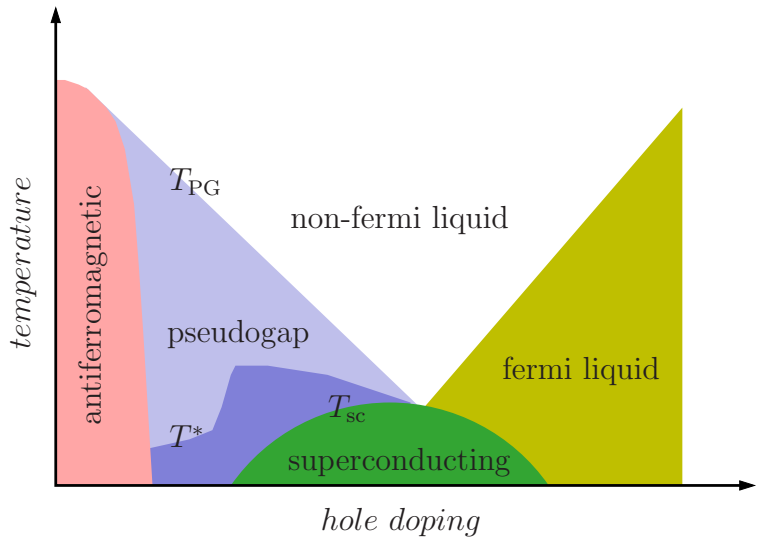

Figure 2.5: Phase diagram of the high-T_c superconductors. The different electronic and magnetic states and the phase transition temperatures between them are denoted. T_{PG} marks the temperature, where the pseudogap develops and T_{sc} marks the superconducting transition temperature. T^* denotes the temperature where a precursor superconducting state develops that is lacking macroscopic phase coherence.

Besides YBCO, there are several related superconducting materials with a similar structure containing one or more CuO_2-planes. They all have a T_{sc} higher than 30 K, show an anisotropic superconducting gap with *d*-wave symmetry and a high anisotropy between the electronic and superconducting properties along the *ab*-plane and the *c*-axis direction [39]. These materials are generally called *cuprates* or *high-T_c superconductors*. Those compounds which contain only one CuO_2-plane per unit cell are referred to as *single layer compounds*, while those containing two CuO_2-planes are referred to as *bilayer compounds*.

To date, there exists no satisfactory theoretical understanding of the high-T_c superconductors. Nevertheless, it is generally accepted that superconductivity has its origin in the CuO_2-planes and is closely related to the charge mobility therein: According to local density approximation band calculations, $YBa_2Cu_3O_6$ should be a metal with one electron per Cu-ion in the half-filled $3d_{x^2-y^2}$ band. However, it is found to be an insulator with a long range antiferromagnetic order because of the strong Coulomb repulsion between the charge carriers which prevents a double occupancy on the Cu sites. This correlation-induced, antiferromagnetic insulating state is called a *Mott insulator*. It can be destroyed by introducing electron holes in the CuO_2-planes. At a sufficiently large hole concentration (*doping*), the superconducting state is established. If the doping level is below the level of optimal doping, one speaks of the *underdoped* regime, while one speaks of the *overdoped* regime if the doping level is above the optimal doping one (Figure 2.5). In the special case of YBCO, electrons are removed from the CuO_2-planes with increasing oxygen content via the apical oxygen atoms located between the CuO_2-planes and CuO-chains [40]. The additional oxygen atoms in the CuO-chains act as *acceptors*. This indirect hole-doping process is the reason for the odd oxygen content of 6.92 for optimal doping in YBCO [41].

Instead of varying the oxygen content, the doping level of YBCO can also be changed by partial substitution of Pr for Y ($Y_{1-x}Pr_xBa_2Cu_3O_7$). As the *c*-axis response in far-

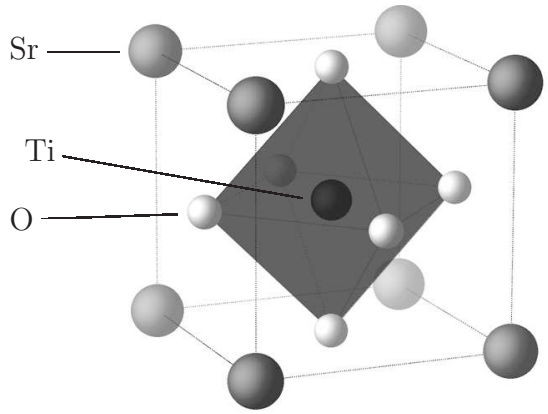

Figure 2.6: Unit cell of $SrTiO_3$ in the pseudocubic phase.

infrared spectral ellipsometry has shown, the electronic properties are very similar for both doping methods [42]. Despite this observation, the fundamental mechanism of doping by Pr-substitution has not yet been understood [43, 42]. Currently, two possible mechanisms are discussed: Either the Pr-ions localise the holes in the CuO_2-planes or they act as *donors* and supply the CuO_2-planes with additional electrons, i. e. compensate the acceptors.

All high-T_c superconductors show the opening of a second gap at the Fermi level already above T_{sc}. This second gap is called *pseudogap* and has a different energy scale and symmetry than the superconducting gap [44]. Its origin is strongly debated. It may be explained in terms of a precursor superconductivity which becomes macroscopically coherent below T_{sc} or in terms of a spin or charge density wave state. For example, there is a model for a precursor superconducting state with low coherence which comprises the Josephson effects between the two CuO_2-planes in one bilayer and between neighbouring bilayers [45, 46]. This model reveals the onset of a precursor superconducting state with a short coherence length at $T^* \approx 120$ - 160 K. This temperature appears to be well distinguishable from the temperature where the pseudogap opens. This distinction is in agreement with more recent experimental results which even suggest that a precursor superconducting gap and a spin or charge density wave gap are realised in the normal state of underdoped cuprates [47].

2.1.4 Properties of the Substrate $SrTiO_3$

$SrTiO_3$ (STO) has a perovskite crystal structure. At room temperature it has a pseudocubic structure with a lattice parameter of 3.905 Å and the space group *Pnma* (Figure 2.6). It is diamagnetic and at low temperatures close to a ferroelectric phase that can be stabilised by ^{18}O-substitution [48]. The termination of STO surfaces with (001)-orientation can be controlled with chemical etching [49]. For these reasons and because it is readily available in the form of large single crystals, STO is a commonly used substrate material for growing heteroepitaxial thin films and multilayers with perovskite-like structure. Nonetheless, it has fairly complex structural properties with a series of structural phase transitions [50, 48]. Besides the antiferrodistortive cubic-to-tetragonal phase

transition at $T^{\mathrm{I}}_{\mathrm{STO}} = 104\,\mathrm{K}$, there are at least two more transitions: The second transition at $T^{\mathrm{II}}_{\mathrm{STO}} = 65\,\mathrm{K}$ gives rise to a heterogeneous state with crystallites with a rhombohedral structure that are embedded in the otherwise tetragonal crystal matrix. The nature of the third transition reported at $T < 30\,\mathrm{K}$ [50] is less well understood. Measurements with nuclear magnetic resonance (NMR) have revealed changes in the local electric field gradients of the Ti-ions that are spatially inhomogenous. The effect is sample dependent and is strongly affected by oxygen isotope substitution [48, 51] or by the application of uniaxial stress [52].

The most extensively investigated transition is the cubic-to-tetragonal transition at $T^{\mathrm{I}}_{\mathrm{STO}}$ [53, 54, 55, 56, 57, 58, 59]. For the near-surface region it has been reported that this transition can occur at significantly higher temperatures of $T^{\mathrm{I}'}_{\mathrm{STO}} \approx 150\,\mathrm{K}$ [55, 56, 57, 58, 59]. Furthermore, x-ray diffraction measurements suggest that the near-surface region at $T^{\mathrm{I}'}_{\mathrm{STO}} > T > T^{\mathrm{I}}_{\mathrm{STO}}$ consists of a heterogeneous mixture of cubic and tetragonal crystallites [59]. This observation highlights that the surface structural properties of $SrTiO_3$ substrates are subject to complex relaxation phenomena and related structural domain states. Further investigations on the properties of STO (001)-substrates were performed within the context of this work and are presented in section 4.1.

2.1.5 General Properties of Thin Film Systems and Heterostructures

Thin layers can have considerably different physical properties than the corresponding bulk materials. This change in properties can have several reasons. One possibility is the increased importance of the layer surfaces which can be free surfaces or interfaces to other materials. In the former case, a reconstruction of the surface or a chemical change due to air contact can induce a change in properties, while in the latter case a lattice mismatch with the adjacent material can lead to strain induced effects. A second possibility is that the proximity to another material with a different or even competing order gives rise to new electronic or magnetic properties due to the mutual interaction of the two orders.

Proximity effects can therefore be of structural or of electronic or magnetic origin. The structural, strain induced proximity effects are often intentionally reduced to a minimum in order to investigate the electronic and magnetic proximity effects. This is achieved by using materials with a minimal lateral lattice mismatch which allows for a heteroepitaxial growth of the heterostructures and a tailoring of atomically flat interfaces. Technical advances in the past years have made the growth of such heteroepitaxial heterostructures possible as is shown in the prominent example of a high conductivity observed at the interfaces between two insulators [60, 61].

Besides the intentional reduction of the structural proximity effects one can choose materials with suitable properties like for example materials, where the electronic and magnetic orders of the individual materials are competing. Ferromagnet / superconductor heterostructures are therefore promising candidates because the electron spins couple parallel in ferromagnets and antiparallel in the Cooper pairs of superconductors.

2.1.6 Literature on Proximity Effects in Ferromagnet / Superconductor Heterostructures

A large number of experimental and theoretical studies has been published on ferromagnet / superconductor heterostructures. A limited selection of them is briefly discussed here in order to introduce some concepts that are used later in this work.

FFLO-State: P. Fulde, R.A. Ferrell, A.I. Larkin and Y.N. Ovchinnikov presented a theory for a superconductor in the presence of a strong, spatially homogeneous magnetic exchange field h [62, 63]. Their model is based on the BCS-theory [11], where the electrons form so-called *Cooper pairs*. These quasiparticles are spin singlets and consist of two electrons with equal energy E_F and opposite momentum ($\boldsymbol{k}_\mathrm{F}^\uparrow = -\boldsymbol{k}_\mathrm{F}^\downarrow$). Thus, the momentum of the Cooper pairs vanishes: $\boldsymbol{k}_\mathrm{Cooper} = \boldsymbol{k}_\mathrm{F}^\uparrow + \boldsymbol{k}_\mathrm{F}^\downarrow = 0$.

The presence of a ferromagnetic exchange field h gives rise to a Zeeman splitting ΔE_ex of the energies of the spin down and spin up electron states. Subsequently, the properties of the Cooper pairs become modified: The electrons still have the same energy E_F, but the momentum of the spin up electron is reduced by $\boldsymbol{k}_{1/2\,\Delta E_\mathrm{ex}}$, while the one of the spin down electron is increased by $\boldsymbol{k}_{1/2\,\Delta E_\mathrm{ex}}$. Since the electron momentums point in opposite directions, the Cooper pairs obtain a finite momentum $\boldsymbol{k}_\mathrm{Cooper} = 2\boldsymbol{k}_{1/2\,\Delta E_\mathrm{ex}}$. Due to this momentum, the superconducting order parameter becomes spatially modulated on a length scale of $\frac{2\pi}{k_\mathrm{Cooper}}$. Therefore, spatially inhomogeneous states can be expected in ferromagnet / superconductor heterostructures.

Oscillating T_sc: Z. Radović *et al.* predicted an oscillatory dependence of the superconducting transition temperature T_sc on the ferromagnet layer thickness d_FM [21]. Assuming both the ferromagnet and the superconductor to be dirty (i. e. a small mean free path and therefore nearly isotropic movement of the electrons), they used Usadel's dirty limit version of the quasiclassical theory of superconductivity [13]. In that case, the characteristic length scale over which the superconducting order parameter decays into the ferromagnet is

$$\xi_\mathrm{FM} = \sqrt{\frac{4\hbar D_\mathrm{FM}}{\Delta E_\mathrm{ex}}}, \tag{2.1}$$

where D_FM is the diffusion coefficient in the ferromagnet and ΔE_ex the exchange energy of the ferromagnet (Zeeman splitting of the spin up and spin down conduction band's energies due to the magnetic exchange field h). Since the exchange energy favours one of the spin orientations, it acts as a pair breaker for the spin singlet Cooper pairs and reduces the value of ξ_FM. In a normal metal, where there is no such exchange energy, the corresponding length scale over which the superconducting order parameter decays is

$$\xi_\mathrm{N} = \sqrt{\frac{\hbar D_\mathrm{N}}{2\pi k_\mathrm{B} T}}, \tag{2.2}$$

where D_N is the diffusion coefficient in the normal metal.

In the calculations of Z. Radović *et al.*, the superconducting order parameter is also assumed to be reduced on the superconductor side of the interface. This characteristic length scale is for a bulk superconductor

$$\xi_{\mathrm{sc0}} = \sqrt{\frac{\hbar D_{\mathrm{sc}}}{2\pi k_{\mathrm{B}} T_{\mathrm{sc0}}}}, \tag{2.3}$$

where D_{sc} is the diffusion coefficient in the superconductor and T_{sc0} is the transition temperature of the bulk superconductor. Since the transition temperature of a superconductor becomes reduced in a thin layer in proximity to a ferromagnet, Z. Radović *et al.* use a corresponding length scale ξ_{sc} which depends on the reduced transition temperature $T_{\mathrm{sc}}^{\mathrm{red}}$:

$$\xi_{\mathrm{sc}} = \sqrt{\frac{\hbar D_{\mathrm{sc}}}{2\pi k_{\mathrm{B}} T_{\mathrm{sc}}^{\mathrm{red}}}}. \tag{2.4}$$

The value of ξ_{sc} is thus larger than the one of ξ_{sc0}. It gives a lower limit below which no superconductivity occurs: $T_{\mathrm{sc}}^{\mathrm{red}}$ vanishes if the thickness of the superconductor d_{sc} is smaller than twice the length ξ_{sc} over which the superconducting order parameter changes ($d_{\mathrm{sc}} < 2\xi_{\mathrm{sc}}$). In the opposite case, $T_{\mathrm{sc}}^{\mathrm{red}}$ is finite.

If $T_{\mathrm{sc}}^{\mathrm{red}}$ is finite and the ferromagnetic layer thickness is of the same order as the coherence length of the superconducting order parameter in the ferromagnetic layer ($d_{\mathrm{FM}}/\xi_{\mathrm{FM}} \approx 1$), an oscillatory behaviour of $T_{\mathrm{sc}}^{\mathrm{red}}$ is expected in superconductor / ferromagnet / superconductor heterostructures: In the limit of $d_{\mathrm{FM}} < \xi_{\mathrm{FM}}$, the phase of the superconducting order parameter remains the same in the two superconducting layers. In this limit, the exchange energy ΔE_{ex} acting on the superconductor increases with increasing d_{FM}. Therefore $T_{\mathrm{sc}}^{\mathrm{red}}$ decreases with increasing d_{FM}. If d_{FM} is about the same as ξ_{FM}, it becomes more favourable for the superconducting order parameter to introduce a π-phase shift from one superconducting layer to the next one. This reduces the pair-breaking effect of the exchange energy ΔE_{ex} on the superconducting order parameter. Therefore $T_{\mathrm{sc}}^{\mathrm{red}}$ is enhanced even though the thickness of the ferromagnetic layer has been increased. With further increasing d_{FM}, $T_{\mathrm{sc}}^{\mathrm{red}}$ becomes again reduced, as the phase of the superconducting order parameter changes over a length scale of ξ_{FM}. This oscillatory behaviour of $T_{\mathrm{sc}}^{\mathrm{red}}$ as a function of d_{FM} has been confirmed in several experiments on ferromagnet / superconductor heterostructures based on conventional, non-oxide materials [64, 20, 65].

Condensation Energy: I. Baladié and A.I. Buzdin went a step further and calculated the thermodynamic properties of ferromagnet / superconductor / ferromagnet nanostructures as a function of the ferromagnetic layer thickness d_{FM} and the interface transparency [66]. They assumed the superconducting layer thickness d_{sc} to be smaller than the superconducting coherence length ξ_{sc} and assumed the dirty limit for all layers in order to use the Usadel's equations [13] like Z. Radović *et al.* in

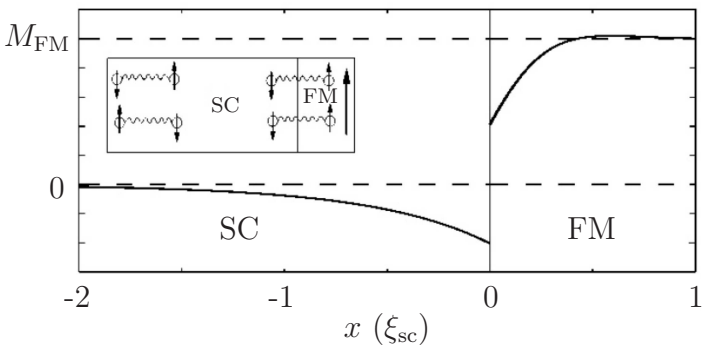

Figure 2.7: Inverse proximity effect: One electron of a Cooper pair which resides mainly in the ferromagnet aligns its spin parallel to the ferromagnetic moment. The second electron of the same Cooper pair which resides mainly in the superconductor aligns its spin antiparallel to conserve the Cooper pair's singlet state. This figure was taken from [69].

Ref. [21]. For the limit of a high interface transparency, they calculated the superconducting transition temperature as

$$T_{\mathrm{sc}}^{\mathrm{red}} = T_{\mathrm{sc0}} \left(1 - \frac{\pi}{2\tau T_{\mathrm{sc0}}} \right), \tag{2.5}$$

where τ is the magnetic scattering time ($\tau \propto 1/\Delta E_{\mathrm{ex}}$) which reduces T_{sc}. If the influence of magnetism on the superconductivity is weak, i. e. if $1/\tau T_{\mathrm{sc0}} \ll 1$, the superconducting condensation energy can be approximated as

$$E_{\mathrm{cond}} = -\gamma_0 \left(\frac{T_{\mathrm{sc}}^{\mathrm{red}} - T}{T_{\mathrm{sc0}}} \right), \tag{2.6}$$

where γ_0 is a constant. The parameter γ_0 is specified in [66]. Here, it is not of specific interest.

Inverse Proximity Effect: F.S. Bergeret, A.F. Volkov and K.B. Efetov published calculations following a different motivation than Z. Radović *et al.* or I. Baladié and A.I. Buzdin: They explained the surprisingly high conductance observed in metallic ferromagnets in proximity to a superconductor in the superconducting state [67] with a spin-triplet contribution to the superconducting order parameter. They assumed a small value of the anomalous quasiclassical Green's function (low interface transparency) in order to linearise the Usadel's equations. They showed that an inhomogeneity in the magnetisation at an interface can induce such a triplet component of the superconducting order parameter that corresponds to Cooper pairs with parallel electron spins [68, 69, 70]. The penetration depth of this triplet component into the ferromagnetic layer is eventually much larger than the one of the singlet component ξ_{FM}:

$$\xi_{\mathrm{FM}}^{\uparrow\uparrow} = \sqrt{\frac{\hbar D_{\mathrm{FM}}}{2\pi k_{\mathrm{B}} T}} > \sqrt{\frac{4\hbar D_{\mathrm{FM}}}{\Delta E_{\mathrm{ex}}}} = \xi_{\mathrm{FM}}. \tag{2.7}$$

The length $\xi_{\mathrm{FM}}^{\uparrow\uparrow}$ is in fact of the same order as the penetration depth of the singlet

component into a normal metal (see Equation (2.2)). Following the idea of a triplet component of the superconducting order parameter, they calculated the influence of the conduction electrons on the magnetisation of the ferromagnet and on the magnetisation induced in the superconductor. In Ref. [69] they used a simple mean field approximation model where they assume the ferromagnetic exchange energy ΔE_{ex} to be smaller than the Fermi energy and assumed a low interface transparency. They concluded that the magnetisation in the ferromagnet can be reduced and that a magnetic moment aligned antiparallel to the one in the ferromagnet can be induced in the superconductor over the length scale of the superconducting coherence length ξ_{sc} [69, 70]. In an extremely simplified picture, one can imagine Cooper pair singlets of which one of the electrons penetrates into the ferromagnetic layer, while the second one is more localised in the superconductor. The electron in the ferromagnet will align its spin along the local magnetic field. Subsequently, the spin of the second electron has to align antiparallel in order to sustain the singlet state of the Cooper pair (see Figure 2.7). F.S. Bergeret, A.F. Volkov and K.B. Efetov called this effect the *inverse proximity effect* because there is a magnetic moment induced in the superconductor which is antiparallel aligned to the ferromagnetic moment.

2.1.7 Previous Experimental Works on YBCO / LCMO Heterostructures

The first studies on YBCO / LCMO heterostructures have been reported in the late 1990ies. They were motivated by the findings that LCMO is a half-metal with a fully spin polarised conduction band and thus ideally suited for an efficient spin injection into adjacent materials, while YBCO is a superconductor with a complex *d*-wave symmetry order parameter and a very high transition temperature. YBCO / LCMO heterostructures were thus expected to be suitable candidates for spintronic devices [23]. Additionally, it had become technically possible to grow YBCO and LCMO heteroepitaxially on top of each other [22, 71, 72]. Further interests came from the fact, that the two competing order parameters of YBCO and LCMO have a similar energy scale (i. e. similar phase transition temperatures), which may lead to new, proximity-induced physics.

A sizeable number of studies on YBCO / LCMO heterostructures has been published since then. Those studies which used different techniques than this work and which have been published before 2006 are introduced below. The other relevant studies are introduced in the respective sections of the chapter on the experiments.

Z. Sefrioui *et al.* (2003): Z. Sefrioui and co-workers reported a new proximity effect [24]. They observed by transport (resistance) and by magnetisation measurements with a superconducting quantum interference device (SQUID) that superconductivity survives even in 3.5 nm thick YBCO layers that are adjacent to a ferromagnet. These are considerably thinner superconducting layers than achievable with conventional superconductors. They also observed that T_{sc} changes with varying ferromagnetic layer thickness in heterostructures with a ferromagnetic layer thickness of up to 100 nm. This value is much larger than in conventional heterostructures.

The former observation can be explained by the short superconducting coherence length in YBCO of 0.1 - 0.3 nm (along the c-axis), while the latter remains subject to speculations. According to the theory of Z. Radović *et al.* [21], a coupling of the superconducting order parameter through a ferromagnetic layer should only be possible if the ferromagnetic layer is thinner than two times the decay length of the superconducting order parameter into the ferromagnet ($d_{\mathrm{FM}} < 2\xi_{\mathrm{FM}}$). T_{sc} should then only be dependent on the thickness of the ferromagnetic layers. The observed length scale is specially remarkable, since the exchange energy in LCMO is very large (about 3 eV [73]) and therefore ξ_{FM} small. Z. Sefrioui and co-workers propose that a reduced magnetic moment in the LCMO layers and a high interface transparency are the main reasons for the unusually large value of ξ_{FM}. A different explanation which has not been discussed by Z. Sefrioui and co-workers would be a triplet component of the superconducting order parameter as described by F.S. Bergeret, A.F. Volkov and K.B. Efetov [68]: The value of $\xi_{\mathrm{FM}}^{\uparrow\uparrow}$ can be considerably larger than the one of ξ_{FM} since the ferromagnetic exchange coupling in the ferromagnetic layers does not give rise to a pair breaking of a triplet.

T. Holden *et al.* (2004): T. Holden and co-workers reported that even the normal state electronic properties of YBCO / LCMO superlattices exhibit an unusual dependence on the layer thickness [25]. They investigated the electronic properties of YBCO / LCMO superlattices with spectral ellipsometry and observed that the metallic response is reduced for superlattices with a layer thickness of less than 16 nm in the far infrared range (100 - 700 cm^{-1}). This effect was strongest, when the YBCO and the LCMO layers were equally thick. The authors did not observe this reduction of the metallic response if they used samples with a paramagnetic metal like $LaNiO_3$ or an insulator like $PrBa_2Cu_3O_7$ instead of LCMO.

N. Haberkorn *et al.* (2004): N. Haberkorn and co-workers observed an exchange bias in YBCO / LCMO superlattices grown on MgO at low temperatures if the samples were cooled in an applied magnetic field of 1 T [26]. They attributed this effect to a thin layer in interface vicinity which is ordered antiferromagnetically. They expected this layer to be located in the LCMO layers and to consist of antiferromagnetically ordered Mn-ions, because they measured a reduced net magnetic moment of the LCMO layers as compared to the bulk value and because H_{coerc} did not obey the inverse proportionality to the film thickness that is expected for thin magnetic films [74]. The antiferromagnetic layers could arise due to interdiffusion of Mn- or Cu-cations, due to stress or due to a different oxygen concentration at the interfaces. Antiferromagnetism is by orders of magnitude less sensitive to direction changes of an applied magnetic field than ferromagnetism. An antiferromagnetic layer at the interfaces could therefore induce an easy direction for the adjacent moments in the ferromagnetic ordered centre of the LCMO layers and lead to the observed exchange bias.

V. Peña *et al.* (2005): V. Peña and co-workers measured an unconventional giant magnetoresistance effect in LCMO / YBCO / LCMO trilayers in the superconducting

state [27]. If the magnetic moments were in the layer plane and the temperature was close to T_{sc}, they found a maximum magnetoresistance $\Delta R/R = (R_{max} - R_{min})/R_{min}$ of up to 1600%, which was decreasing exponentially when getting closer to T_{sc}. The only precondition for this effect was a working temperature below T_{sc}. The most important difference compared to a conventional giant magnetoresistance effect was, that they measured the highest resistance for an antiparallel alignment of the magnetic moments in the LCMO layers and the lowest one for a parallel alignment. This is opposite to the systems with conventional superconductors that are discussed by I. Baladié and A.I. Buzdin in Ref. [66]. The effect observed by V. Peña and co-workers occurred in heterostructures with a YBCO layer thickness of up to 30 nm, which is considerably larger than the fraction of a nanometer of the superconducting coherence length ξ_{sc} in YBCO along the c-axis. This is opposite to the assumption made by I. Baladié and A.I. Buzdin, where the thickness of the superconducting layer was smaller than ξ_{sc}. It seems therefore, that there is an additional length scale which has to be considered in order to explain the observed physical phenomena. V. Peña and co-workers gave an explanation without focussing on an additional length scale. They argued with the injection of spin-polarised carriers into the YBCO layer: In case of an antiparallel alignment, the injected charge carriers find a high potential barrier to leave the superconductor at the interface to the second ferromagnetic layer and therefore accumulate in the YBCO layer. The superconducting current density can subsequently be reduced by the accumulated spins. In the case of a parallel alignment, this spin accumulation does not take place and the resistance through the layers remains low.

An alternative explanation could be the formation of a spin density wave in the YBCO layer that is similar to the one which can be induced by the application of an external magnetic field in underdoped $La_{2-x}Sr_xCuO_4$ single crystals [75, 76, 77]. Such a spin density wave may couple the ferromagnetic layers through longer distances than superconductivity.

2.2 Polarised Neutron Reflectometry

The technique of polarised neutron reflectometry is discussed here. In the first part, the theoretical background is explained. Therefore, the underlying concept is introduced and the experimental geometry is shown with all the notations that are used in this work. Then, two different experimental modes are briefly introduced and the mathematical description of specular reflectometry experiments is worked out for simulation purposes and extended to simulate polarised neutron reflectometry measurements. Surface and interface roughnesses are included in the formalism. The instrument resolution is discussed and subsequently included as well. Based on the instrument resolution, the coherence volume of the probing radiation is estimated. Subsequently, the influence of the lateral and vertical coherence length on lateral and vertical correlations in the sample are discussed together with the limitations of the mathematical formalism for reflectometry simulations. In the second part of this section, the principle of a polarised neutron reflectometer

is briefly explained. Therefore, the characteristics of a neutron beam are discussed by starting from the neutron source. Subsequently, the geometry of a reflectometer and the setup required for the neutron polarisation are discussed. Finally, a formalism is introduced which corrects polarised neutron reflectometry data for a non-perfect neutron polarisation.

2.2.1 Theoretical Background

The technique reflectometry probes the depth profile of the potential in the sample. It is used to investigate surfaces, single layers, multilayers and even thin films of liquids. The underlying concept of this method is that a probe beam experiences in each medium a potential which corresponds to a certain refraction index. Therefore, an interface between two different media is experienced as a potential step which corresponds to a change of the refraction index. This causes a partial reflection and a partial transmission and refraction of the probe beam at the interface. The ratio of the reflected and the transmitted part of the beam does not only depend on the two refraction indices but also on the wavelength of the probe beam and the angle of incidence of the probe beam with respect to the interface. Thus, one can investigate the potential of a material by measuring the reflected part of the probe beam as a function of angle or wavelength.

If the investigated sample does not only consist of one material but of several layers of different materials, the surface and all interfaces reflect and transmit parts of the beam. This leads to a wave field in the sample which may constructively or destructively interfere when leaving the surface of the sample. Accordingly, interference effects can be observed as angular and wavelength dependent intensity variations of the reflected beam. These intensity variations contain the information on the depth profile of the potential in the sample.

What kind of potential is investigated in a reflectometry experiment depends on the probe beam. With each type of beam, a different potential and thus different property of the sample is probed. In most reflectometry experiments, either an x-ray or a neutron beam is used. The former investigates the electron density and the x-ray absorption, while latter probes the nuclear scattering length density, the in-plane magnetic induction and the neutron absorption which is in most cases negligible.

Figure 2.8 shows the experimental geometry used for reflectometry measurements and indicates the notations that are used in this work: The incident probe beam with wave vector $\boldsymbol{k}_\mathrm{i}$ touches the sample surface at the angle α_i. The scattered part of the beam leaves the sample with the wave vector $\boldsymbol{k}_\mathrm{f}$ at the angle α_f with respect to the surface. The angle between $\boldsymbol{k}_\mathrm{i}$ and $\boldsymbol{k}_\mathrm{f}$ is called the *total scattering angle* 2θ. It is usually smaller than 3 - 5°. The plane which is defined by $\boldsymbol{k}_\mathrm{i}$ and $\boldsymbol{k}_\mathrm{f}$ is called the *scattering plane*. It is oriented perpendicular to the *sample plane* because one integrates in reflectometry over the intensity which is scattered along the y-direction. The momentum transfer experienced by the probe beam at the sample is denoted as $\boldsymbol{q} = \boldsymbol{k}_\mathrm{f} - \boldsymbol{k}_\mathrm{i}$ and lies in the scattering plane. The intensity which is scattered (reflected) at the sample is mainly caused by elastic

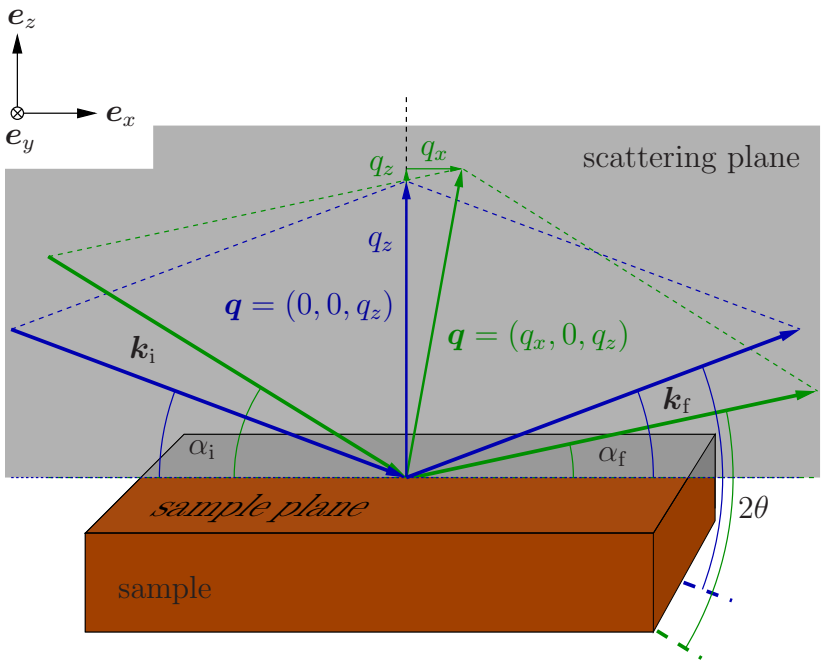

Figure 2.8: Sketch of the experimental geometry used for reflectometry measurements. The incident beam with wave vector $\boldsymbol{k}_\mathrm{i}$ touches the surface at the angle α_i. The scattered part of the beam has the wave vector $\boldsymbol{k}_\mathrm{f}$ and leaves the sample at the angle α_f. The momentum transfer experienced by the beam at the sample is $\boldsymbol{q}$. For specular reflectometry ($\alpha_\mathrm{i} = \alpha_\mathrm{f}$), the momentum transfer points along the surface normal $\boldsymbol{e}_z$. For off-specular reflectometry ($\alpha_\mathrm{i} \neq \alpha_\mathrm{f}$), an additional component of the momentum transfer along $\boldsymbol{e}_x$ is probed. This component is lying in the sample plane and in the scattering plane.

processes. Accordingly, the values of $|\boldsymbol{k}_\mathrm{i}|$ and $|\boldsymbol{k}_\mathrm{f}|$ are the same in a good approximation. Thus, the components of the momentum transfer vector $\boldsymbol{q}$ are

$$q_x = \frac{2\pi}{\lambda}\left(\cos\alpha_\mathrm{f} - \cos\alpha_\mathrm{i}\right) \tag{2.8}$$

$$q_y := 0 \tag{2.9}$$

$$q_z = \frac{2\pi}{\lambda}\left(\sin\alpha_\mathrm{f} + \sin\alpha_\mathrm{i}\right), \tag{2.10}$$

where λ is the wavelength of the probing beam.

If the angles α_i and α_f are kept the same, the momentum transfer has solely a component along the z-axis: $\boldsymbol{q} = (0, 0, q_z)$. This angular setting is called *specular reflectometry*. Such measurements are usually displayed as a function of q_z. If the angles α_i and α_f are different, the momentum transfer has also a component parallel to the sample surface and parallel to the x-axis: $\boldsymbol{q} = (q_x, 0, q_z)$. Measurements as a function of q_x and q_z are called *off-specular reflectometry* measurements. They enable the observation of structures or roughnesses that are correlated laterally and vertically to the sample plane. They are usually displayed as mappings of the parameters α_i and α_f or q_x and q_z.

Experimental Modes

According to Equations (2.8) and (2.10), the momentum transfer vector $\boldsymbol{q}$ depends on the angle of incidence α_i, on the final angle α_f and on the beam's wavelength λ. Due to these dependencies, two different modes can be used to perform reflectometry measurements:

Angle Dispersive Mode: The probe beam is monochromatic, i. e. has a well known single wavelength λ. The reflected intensity of the beam is measured at various angles α_i and α_f.

Energy Dispersive Mode: The probe beam is polychromatic. The measurement is performed for fixed angles α_i and α_f by detecting the reflected intensity as a function of the wavelength. If the $\boldsymbol{q}$-range of interest is larger than the range of available wavelengths, measurements have to be performed at different angles α_i and α_f.

In x-ray reflectometry, the angle dispersive mode is more often used because the x-ray absorption is highly wavelength dependent and because x-ray sources (except for synchrotrons) do not provide a broad enough range of wavelengths for energy dispersive measurements.

In neutron reflectometry, the experimental mode that is used depends on the neutron source and on the purpose of the instrument. At continuous neutron sources, the angle dispersive mode is more often realised: A specific wavelength for the experiment is selected with a monochromator. At pulsed sources, the neutron pulses are short and consist of a wavelength continuum. Therefore, a reflectometer in the energy dispersive mode can use all neutrons by measuring for each pulse the time the neutrons need to reach the detector. The energy dispersive mode has the advantage that a measurement can be performed without moving or rotating the sample. This allows also for reflectometry measurements on liquid / liquid or liquid / gas interfaces.

Theory of Specular Reflectometry

A mathematical formalism that describes the specular reflectivity from a perfectly flat surface and from perfectly flat interfaces has been introduced by L.G. Parratt in 1954 [78]. This formalism is one dimensional because the momentum transfer experienced by the probe beam at the sample is in specular reflectometry parallel to the surface normal, which implies that the beam's momentum is conserved in the sample plane. Therefore, the formalism works with the projections of the incident and final wave vectors on the surface normal (z-axis): The projection of the incident wave vector is

$$k_0 = -k_\mathrm{i} \sin \alpha_\mathrm{i}, \tag{2.11}$$

while the projection of the final wave vector is

$$\begin{aligned} -k_0 &= k_\mathrm{f} \sin \alpha_\mathrm{f} \\ &= k_\mathrm{i} \sin \alpha_\mathrm{i}. \end{aligned} \tag{2.12}$$

Therefore, the normalised, one dimensional incident wave is described as a plane wave $e^{ik_0 z}$. A sample consisting of one material that reaches from $-\infty$ to z_1 is experienced by this

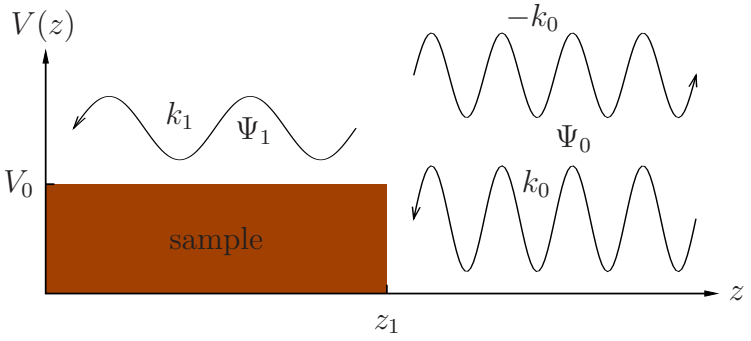

Figure 2.9: A plane wave with the wave vector k_0 is incident on a potential step V_0 at the position z_1. The wave is partially reflected ($-k_0$) and partially transmitted (k_1). The sum of the absolute squares of the transmitted and the reflected wave amplitude is equal to the absolute square of the incident wave amplitude.

wave as a potential step at the sample surface at $z = z_1$. From there, one part of the wave is reflected with the amplitude r_0 and the wave vector $-k_0$. The other part of the wave is transmitted through the sample with the amplitude t_1 and the wave vector k_1 (see Figure 2.9). The wave outside of the sample $\Psi_0(z)$ and the wave within the sample $\Psi_1(z)$ are thus described by the ansatz

$$\begin{aligned} \Psi_0(z) &= e^{ik_0 z} + r_0 e^{-ik_0 z} \\ \Psi_1(z) &= t_1 e^{ik_1 z}. \end{aligned} \tag{2.13}$$

The wave vector k_1 in the sample depends on the incoming wave vector k_0 and on the potential V_1 experienced by the beam in the sample. In the case of x-rays, no mass is associated with the wave and k_1 is given by

$$k_1 = \sqrt{k_0^2 - \frac{k_0}{\hbar c} V_1^{\mathrm{x}}}, \tag{2.14}$$

where $\hbar$ is the Planck's constant divided by 2π ($\hbar = 1.054571596 \cdot 10^{-34}\,\mathrm{Js}$) and where $c = 2.99792458 \cdot 10^8\,\frac{\mathrm{m}}{\mathrm{s}}$ is the speed of light. The potential for the x-rays is

$$V_1^{\mathrm{x}} = \frac{4\pi\hbar c}{k_0} r_{\mathrm{el}} \bar{\rho}_{\mathrm{el}}, \tag{2.15}$$

where $r_{\mathrm{el}} = 2.8179 \cdot 10^{-15}\,\mathrm{m}$ is the classical electron radius and $\bar{\rho}_{\mathrm{el}}$ the mean electron density in the sample material. Equation (2.14) can therefore be simplified to

$$k_1 = \sqrt{k_0^2 - 4\pi r_{\mathrm{el}} \bar{\rho}_{\mathrm{el}}}. \tag{2.16}$$

The electron density $\bar{\rho}_{\mathrm{el}}$ of the sample material is calculated by

$$\bar{\rho}_{\mathrm{el}} = \sum_j \rho_j (Z_j + f_j' + i f_j''), \tag{2.17}$$

where the sum is running over all elements occurring in the sample material. ρ_j and Z_j are the number density and the atomic number of the different elements. f_j' is the

real part of the anomalous dispersion factor of element j and takes inelastic scattering processes, i. e. resonance effects into account. f_j'' is the imaginary part of the anomalous dispersion factor and takes the absorption into account. Therefore, the electron density becomes a complex number. Subsequently, k_1 becomes a complex number as well. Only if the absorption is neglected, the electron density and k_1 remain real numbers.

In the case of neutrons as probe beam, a mass is associated with the wave and k_1 becomes

$$k_1 = \sqrt{k_0^2 - \frac{2m_\mathrm{n}}{\hbar^2} V_1^\mathrm{n}}, \tag{2.18}$$

where $m_\mathrm{n} = 1.675 \cdot 10^{-27}\,\mathrm{kg}$ is the neutron mass and where

$$V_1^\mathrm{n} = \frac{2\pi\hbar^2}{m_\mathrm{n}} \bar{\rho}_\mathrm{n} \tag{2.19}$$

is the potential experienced by the neutrons. The latter is a function of the mean nuclear scattering length density $\bar{\rho}_\mathrm{n}$ of the sample material which can be calculated by

$$\bar{\rho}_\mathrm{n} = \sum_l \rho_l b_l. \tag{2.20}$$

As compared to Equation (2.17), this sum contains not only the different elements but also all isotopes. This is due to the fact that the scattering length b_l differs not only from element to element, but also from isotope to isotope. Similarly to the case of x-rays, Equation (2.18) can be simplified to

$$k_1 = \sqrt{k_0^2 - 4\pi\bar{\rho}_\mathrm{n}}. \tag{2.21}$$

The comparison of Equation (2.16) and Equation (2.21) shows that in this formalism for the neutrons the mean nuclear scattering length density plays the same role as the mean electron density times the classical electron radius does in the formalism for the x-rays. In analogy to the x-rays, the neutron absorption is included in the formalism by an imaginary part of the nuclear scattering length density, i. e. an imaginary part of the scattering lengths b_l. This imaginary part is even though often neglected, since the neutron absorption is tiny in most materials.

At the potential step at $z = z_1$ (sample surface), the following boundary conditions apply to the ansatz for the wave function of Equation (2.13):

$$\begin{aligned} \Psi_0(z)\big|_{z=z_1} &= \Psi_1(z)\big|_{z=z_1} \\ \frac{d}{dz}\Psi_0(z)\big|_{z=z_1} &= \frac{d}{dz}\Psi_1(z)\big|_{z=z_1}. \end{aligned} \tag{2.22}$$

Subsequently, one obtains the Fresnel coefficients r_0 and t_1 of the reflected and the transmitted wave:

$$\begin{aligned} r_0 &= \frac{k_0 - k_1}{k_0 + k_1} e^{i2k_0 z_1} \\ t_1 &= \frac{2k_0}{k_0 + k_1} e^{i(k_0 - k_1)z_1}. \end{aligned} \tag{2.23}$$

The sum of the absolute squares of the two coefficients is normalised to the absolute square of the incident wave amplitude ($|r_0|^2 + |t_1|^2 = 1$).

If the sample does not only consist of one single material but of $N-1$ layers on top of a half-infinite substrate, the ansatz given in Equation (2.13) can be extended to

$$\begin{aligned} \Psi_0(z) &= e^{ik_0 z} + r_0 e^{-ik_0 z} \\ \Psi_1(z) &= t_1 e^{ik_1 z} + r_1 e^{-ik_1 z} \\ &\dots \\ \Psi_{N-1}(z) &= t_{N-1} e^{ik_{N-1} z} + r_{N-1} e^{-ik_{N-1} z} \\ \Psi_N(z) &= t_N e^{ik_N z}. \end{aligned} \tag{2.24}$$

Here as in Equation (2.13), the index 0 stands for the vacuum or air outside of the sample. The index N stands for the half-infinite substrate with the $N-1$ layers on top. The intermediate indices are counting through the layers from top to bottom. In analogy to Equation (2.22), the boundary conditions apply to each potential step (interface) at the position z_l as

$$\begin{aligned} t_l e^{ik_l z_l} + r_l e^{-ik_l z_l} &= t_{l-1} e^{ik_{l-1} z_l} + r_{l-1} e^{-ik_{l-1} z_l} \\ ik_l (t_l e^{ik_l z_l} - r_l e^{-ik_l z_l}) &= ik_{l-1} (t_{l-1} e^{ik_{l-1} z_l} - r_{l-1} e^{-ik_{l-1} z_l}), \end{aligned} \tag{2.25}$$

where l is the larger one of the indices of the two adjacent materials. z_1 corresponds in this notation to the position of the surface and z_N corresponds to the position of the interface between the stack of layers and the substrate. This set of boundary conditions can be conveniently translated into a matrix formalism which links the Fresnel coefficients of the material with index $l-1$ to the ones of the material with index l:

$$\begin{pmatrix} e^{ik_l z_l} & e^{-ik_l z_l} \\ ik_l e^{ik_l z_l} & -ik_l e^{-ik_l z_l} \end{pmatrix} \begin{pmatrix} t_l \\ r_l \end{pmatrix} = \begin{pmatrix} e^{ik_{l-1} z_l} & e^{-ik_{l-1} z_l} \\ ik_{l-1} e^{ik_{l-1} z_l} & -ik_{l-1} e^{-ik_{l-1} z_l} \end{pmatrix} \begin{pmatrix} t_{l-1} \\ r_{l-1} \end{pmatrix} \tag{2.26}$$

$$\Rightarrow \begin{pmatrix} t_{l-1} \\ r_{l-1} \end{pmatrix} = \frac{1}{2} \begin{pmatrix} \left(1 + \frac{k_l}{k_{l-1}}\right) e^{i(k_l - k_{l-1}) z_l} & \left(1 - \frac{k_l}{k_{l-1}}\right) e^{-i(k_l + k_{l-1}) z_l} \\ \left(1 - \frac{k_l}{k_{l-1}}\right) e^{i(k_l + k_{l-1}) z_l} & \left(1 + \frac{k_l}{k_{l-1}}\right) e^{-i(k_l - k_{l-1}) z_l} \end{pmatrix} \begin{pmatrix} t_l \\ r_l \end{pmatrix}. \tag{2.27}$$

Hence, the matrix for the respective potential step (interface) is given by

$$Q_{l-1,l} = \frac{1}{2} \begin{pmatrix} \left(1 + \frac{k_l}{k_{l-1}}\right) e^{i(k_l - k_{l-1}) z_l} & \left(1 - \frac{k_l}{k_{l-1}}\right) e^{-i(k_l + k_{l-1}) z_l} \\ \left(1 - \frac{k_l}{k_{l-1}}\right) e^{i(k_l + k_{l-1}) z_l} & \left(1 + \frac{k_l}{k_{l-1}}\right) e^{-i(k_l - k_{l-1}) z_l} \end{pmatrix}. \tag{2.28}$$

Consequently, the Fresnel coefficients of the vacuum and the substrate are linked in the following way with a multiplication of the $Q_{l-1,l}$-matrices:

$$\begin{pmatrix} t_0 \\ r_0 \end{pmatrix} = Q_{0,1} Q_{1,2} \dots Q_{N-2,N-1} Q_{N-1,N} \begin{pmatrix} t_N \\ r_N \end{pmatrix} = \prod_{l=1}^{N} Q_{l-1,l} \begin{pmatrix} t_N \\ r_N \end{pmatrix}. \tag{2.29}$$

The wave in the substrate (index N) consists only of a transmitted component, since the substrate is assumed to be half-infinite. This yields the additional condition $r_N = 0$:

$$\begin{pmatrix} t_0 \\ r_0 \end{pmatrix} = \prod_{l=1}^{N} Q_{l-1,l} \begin{pmatrix} t_N \\ 0 \end{pmatrix} = M \begin{pmatrix} t_N \\ 0 \end{pmatrix} = \begin{pmatrix} M_{11} & M_{12} \\ M_{21} & M_{22} \end{pmatrix} \begin{pmatrix} t_N \\ 0 \end{pmatrix}. \tag{2.30}$$

Here, the notation has been simplified by introducing the matrix M as the product of the $Q_{l-1,l}$-matrices. The elements of M link the two Fresnel coefficients of the wave in the vacuum or in the air above the sample with

$$r_0 = \frac{M_{21}}{M_{11}} t_0. \tag{2.31}$$

As the incoming radiation is normalised to one, $|t_0| = 1$ and the specular reflectivity becomes

$$R = |r_0|^2 = \frac{|M_{21}|^2}{|M_{11}|^2}. \tag{2.32}$$

The reflectivity R is a function of k_0. It is usually plotted versus the momentum transfer q_z, which is according to Equations (2.11) and (2.12) defined for specular reflectometry by

$$q_z = k_\mathrm{i} \sin \alpha_\mathrm{i} + k_\mathrm{f} \sin \alpha_\mathrm{f} = -2k_0. \tag{2.33}$$

In specular reflectometry, the condition $\alpha_\mathrm{i} = \alpha_\mathrm{f} = \frac{2\theta}{2}$ applies. Therefore, Equation (2.33) for q_z can be reduced to

$$q_z = 2k \sin \frac{2\theta}{2} = \frac{4\pi}{\lambda} \sin \frac{2\theta}{2}, \tag{2.34}$$

where λ is the wavelength of the probe beam.

In the following, the formalism introduced above is applied and discussed by means of some examples. The corresponding, calculated reflectivity curves are shown in Figure 2.10:

Substrate (*a*): The reflectivity curve of a substrate without any layers on top corresponds to a single interface. The corresponding potential step is positive in the case of x-rays (the potential in the substrate is larger than in vacuum or air). In the case of neutrons, it can be positive or negative, since the sign of the scattering length density of the substrate can be positive or negative, depending on the substrate's isotopic composition. In the case of a positive potential step, the entire probe beam is reflected for $q_z < q_\mathrm{c} \approx 4\sqrt{\pi \bar{\rho}_\mathrm{n}}$. The maximum value of q_z, where total reflection still occurs, is called the *edge of total reflection* and is denoted as q_c. At q_z-values larger than q_c, the reflectivity R decays rapidly. At $q_z > 3q_\mathrm{c}$, it decays with $R \propto q_z^{-4}$. This makes it clear, that the experimental conditions in reflectometry must allow for the measurement of the reflected intensity over several orders of magnitude in order to obtain the most information possible. Figure 2.10 *a* shows the neutron reflectivity curve calculated for a $SrTiO_3$ substrate.

Single Layer (*b*): A single layer on top of a substrate contains a potential step at the surface and at the interface between the substrate and the layer. Hence an interference pattern is observed in the reflectivity curve at $q_z > q_c$. Figure 2.10 *b* shows the neutron reflectivity curves calculated for a 100 Å and a 200 Å thick $YBa_2Cu_3O_7$ layer, respectively. The distance between the oscillation maxima in q_z can be estimated at $q_z > 4q_c$ as $\Delta q_z \approx \frac{2\pi}{d}$, where d is the thickness of the layer. At q_z-values closer to q_c, refraction effects reduce the value of Δq_z and thus falsify this estimate.

Double Layer (*c*): In reflectometry, two layers on top of a substrate show an interference pattern which corresponds to all the length scales given in the system. If the two layers are equally thick, the observed pattern is a play between the pattern corresponding to a layer with the thickness of one single layer and the pattern corresponding to a layer with the thickness of the two layers together. Figure 2.10 *c* shows the neutron reflectivity curve calculated for a 100 Å thick $YBa_2Cu_3O_7$ layer on a $SrTiO_3$ substrate with a 100 Å thick $La_{2/3}Ca_{1/3}MnO_3$ layer on top. Therefore, the length scales 100 Å and 200 Å are involved in the observed interference pattern. The positions of the minima of the 100 Å length scale coincide with the positions of the even order minima of the 200 Å length scale. In this example, the odd order minima of the 200 Å length scale are more pronounced (indicated by black arrows). If the potentials (scattering length densities) of the two layers would be exchanged, these minima would become maxima. Hence it depends on the order of the potential steps, whether minima or maxima occur.

Superlattice (*d*): If several double layers are repeated as a stack, a periodic potential occurs along the surface normal. Such a stack is called a *superlattice*. Figure 2.10 *d* shows the neutron reflectivity curve calculated for a superlattice consisting of ten $YBa_2Cu_3O_7$ / $La_{2/3}Ca_{1/3}MnO_3$ double layers on a $SrTiO_3$ substrate, where each layer is 100 Å thick (the double layers are thus 200 Å thick). Due to the repetition of the double layers, the maxima in the reflectivity curve become more pronounced. These maxima are called *superlattice Bragg reflexes*. They are identified by a numbering that is starting at the first one after the edge of total reflection. Due to the equal thickness of the two layers within a double layer, every even order superlattice Bragg reflex is suppressed. This can be understood in the sense of the common minima for the 100 Å and the 200 Å length scale shown in Figure 2.10 *b* and *c*. The tiny oscillations in the reflectivity curve for the superlattice are induced by an interference term between the surface and the interface between the substrate and the superlattice. They are called *Kiesig fringes*.

Theory of Polarised Specular Neutron Reflectometry

The formalism described above can be extended to account for the interaction of the neutrons with the magnetic induction in the sample: Neutrons carry a magnetic moment of $\mu_n = 9.662 \cdot 10^{-27}\,\mathrm{Am}^2$ and a spin 1/2. The latter can be either aligned parallel or

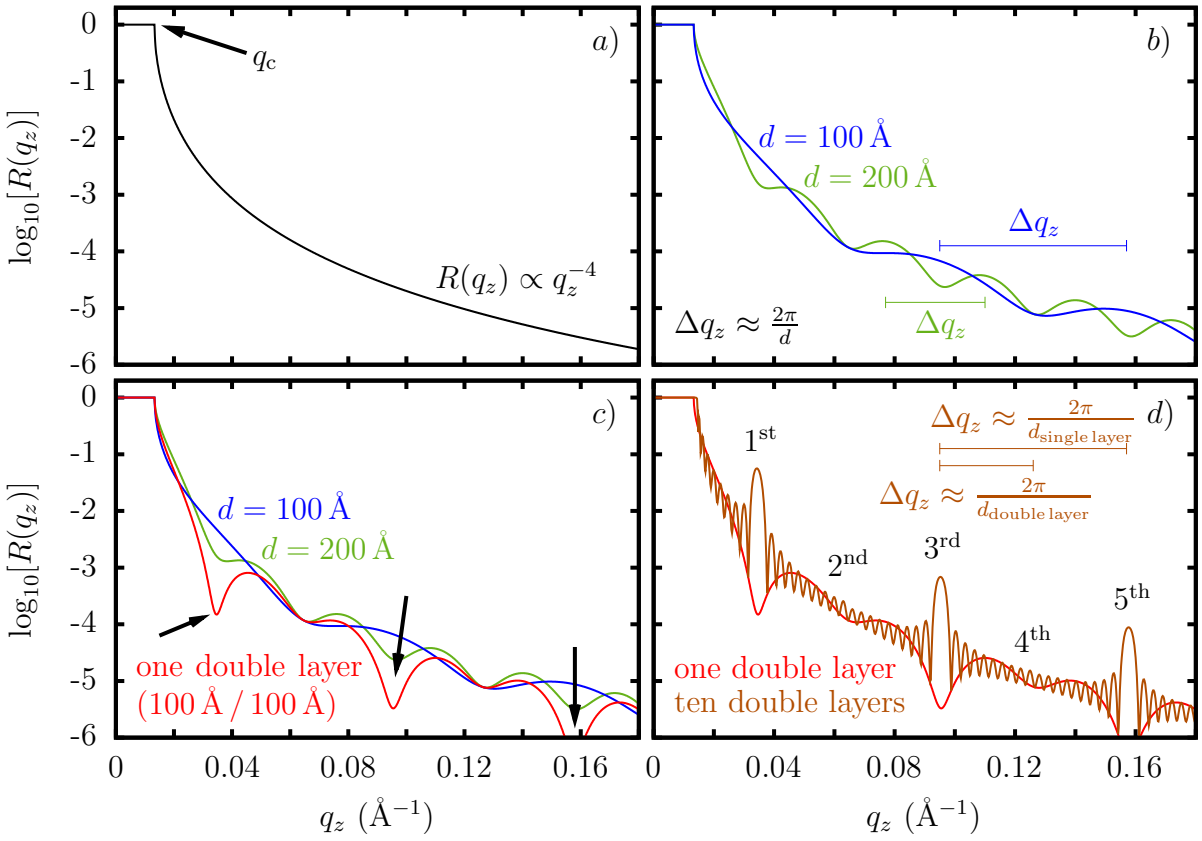

Figure 2.10: Calculated neutron reflectivity curves. *a*) Reflectivity curve for a single $SrTiO_3$ substrate ($\bar{\rho}_n = 3.525 \cdot 10^{-6}$ Å^{-2}). For $q_z < q_c = 0.0134$ Å^{-1}, total reflection occurs. At $q_z > 3q_c$, the reflectivity R decays proportional to q_z^{-4}. *b*) Neutron reflectivity curves for a single $YBa_2Cu_3O_7$ layer ($\bar{\rho}_n = 4.68 \cdot 10^{-6}$ Å^{-2}) on a $SrTiO_3$ substrate with a layer thickness of 100 Å (*blue*) and 200 Å (*green*), respectively. The oscillations are induced by the interference between the wave reflected from the surface and the wave reflected from the interface between the layer and the substrate. The spacing between the oscillation maxima can be estimated by $\Delta q_z \approx \frac{2\pi}{d}$, where d is the thickness of the layer. *c*) Same as *b*) together with a reflectivity curve for a $YBa_2Cu_3O_7$ (100 Å, $\bar{\rho}_n = 4.68 \cdot 10^{-6}$ Å^{-2}) / $La_{2/3}Ca_{1/3}MnO_3$ (100 Å, $\bar{\rho}_n = 3.58 \cdot 10^{-6}$ Å^{-2}) double layer on a $SrTiO_3$ substrate (*red curve*). The black arrows mark the extrema that are induced by the presence of the two length scales corresponding to the individual layer and the double layer thickness. Depending on the scattering length density contrast between the two layers, these extrema may be minima or maxima. Note, that they are located at the positions of the maxima of the 100 Å single layer reflectivity curve. *d*) The reflectivity curve for a double layer shown in *c*) is compared with a reflectivity curve for a stack of ten such double layers (a so-called *superlattice*). The main interference maxima are in analogy to Bragg scattering called *superlattice Bragg reflexes*, even though in reflectometry the refraction at the interfaces plays an important role. These superlattice Bragg reflexes are numbered starting from q_c and spaced according to the double layer thickness. If the individual layers have the same thickness, every even order superlattice Bragg reflex is suppressed, since the minima corresponding to the individual and the double layer thickness match at these positions (see *b* and *c*). The tiny interference maxima in the curve for the superlattice originate from the interference between the surface and the interface between the substrate and the first layer. They are called *Kiesig fringes*.

antiparallel to a given quantisation axis. Hence the neutron wave function is described as a two dimensional vector

$$|\Psi\rangle = \begin{pmatrix} \Psi_\uparrow \\ \Psi_\downarrow \end{pmatrix}, \tag{2.35}$$

where the two components describe the states of the neutron with spin parallel and antiparallel to the quantisation axis. Depending on its spin orientation, the neutron couples differently to the magnetic induction in a material. Accordingly, the potential seen by the neutrons given in Equation (2.19) becomes spin dependent and hence four dimensional [79]. It describes the potentials that conserve the neutron spin states as well as the potentials that flip the neutron spin from up ($|+\rangle$) to down ($|-\rangle$) and $|-\rangle$ to $|+\rangle$, respectively:

$$V_l^{\text{total}} = \begin{pmatrix} V_l^{++} & V_l^{-+} \\ V_l^{+-} & V_l^{--} \end{pmatrix} = \begin{pmatrix} V_l^{\text{n}} + \mu_{\text{n}} B_{\perp l}^c & \mu_{\text{n}}(B_{\perp l}^a - iB_{\perp l}^b) \\ \mu_{\text{n}}(B_{\perp l}^a + iB_{\perp l}^b) & V_l^{\text{n}} - \mu_{\text{n}} B_{\perp l}^c \end{pmatrix}. \tag{2.36}$$

Here, V_l^{n} is the nuclear potential of Equation (2.19) in the material with index l and $\mathbf{B}_{\perp l}$ is the projection of the magnetic induction in the material with index l on the plane perpendicular to the momentum transfer $\boldsymbol{q}$ (in specular reflectometry the sample plane). The indices a, b and c of $\mathbf{B}_{\perp l}$ indicate the components of the magnetic induction in Cartesian coordinates, where the c-axis is oriented along the given quantisation axis, i. e. the externally applied magnetic field.

The projection of the magnetic induction on the sample plane ($\mathbf{B}_\perp$) is used, because only components of $\mathbf{B}$ perpendicular to the momentum transfer $\boldsymbol{q}$ cause magnetic scattering. This originates from the differential magnetic scattering cross section

$$\left(\frac{d^2\sigma}{d\Omega dE'}\right)_{\sigma\varpi\to\sigma'\varpi'} \propto \frac{k'}{k} |\langle \sigma'\varpi'|\boldsymbol{\sigma}\cdot\boldsymbol{Q}_\perp|\sigma\varpi\rangle|^2 \delta(E_\varpi - E_{\varpi'} + \Delta E), \tag{2.37}$$

where σ and σ' are the initial and the final spin states of the neutron, k and k' the initial and the final wave vectors of the neutron, ϖ and ϖ' the initial and the final states of the scattering system with the energy E_ϖ and $E_{\varpi'}$, respectively and where ΔE is the change of energy which the neutron experiences during the scattering process. $\boldsymbol{\sigma}$ is the spin operator of the neutron and $\boldsymbol{Q}_\perp$ is given by

$$\boldsymbol{Q}_\perp = \hat{\boldsymbol{q}} \times (\mathbf{B}(\boldsymbol{q}) \times \hat{\boldsymbol{q}}), \tag{2.38}$$

where $\mathbf{B}(\boldsymbol{q})$ is the total magnetic induction of the scattering system in reciprocal space and $\hat{\boldsymbol{q}}$ is the unity vector in direction of the momentum transfer $\boldsymbol{q}$ [80]. The cross product $\mathbf{B}(\boldsymbol{q}) \times \hat{\boldsymbol{q}}$ in Equation (2.38) shows, that only components of $\mathbf{B}$ perpendicular to $\boldsymbol{q}$ contribute to the scattering cross section. Hence $\mathbf{B}_\perp$ is used in Equation (2.36).

In neutron reflectometry, the quantisation axis is generally chosen to lie in the sample plane. Its direction is defined by an externally applied magnetic field $\mathbf{H}_{\text{appl}}$, which is not necessarily pointing in the same direction as the magnetic induction $\mathbf{B}$ (or $\mathbf{B}_\perp$) inside the sample. The component of $\mathbf{B}_\perp$ which is parallel to the quantisation axis $\mathbf{H}_{\text{appl}}$ enhances or decreases the potential for the spin up or spin down neutrons, respectively, while the components of $\mathbf{B}_\perp$ perpendicular to the quantisation axis $\mathbf{H}_{\text{appl}}$ give rise to a change

of the neutron spin state (see Equation (2.36)). In analogy to the nuclear scattering length density from Equation (2.20), one can define a vectorial magnetic scattering length density:

$$\bar{\boldsymbol{\rho}}_{\mathrm{m}} = -\frac{\mu_{\mathrm{n}} m_{\mathrm{n}}}{2\pi\hbar^2}\mathbf{B}_{\perp}. \tag{2.39}$$

Assuming that the quantisation axis is pointing along the c-axis of $\mathbf{B}_{\perp}$ and hence also of $\bar{\boldsymbol{\rho}}_{\mathrm{m}}$, in analogy to Equation (2.36) the total scattering length density seen by the neutrons becomes

$$\bar{\rho}_{\mathrm{n}}^{\mathrm{total}} = \begin{pmatrix} \bar{\rho}_{\mathrm{n}} + \bar{\rho}_{\mathrm{m}}^{c} & \bar{\rho}_{\mathrm{m}}^{a} - i\bar{\rho}_{\mathrm{m}}^{b} \\ \bar{\rho}_{\mathrm{m}}^{a} + i\bar{\rho}_{\mathrm{m}}^{b} & \bar{\rho}_{\mathrm{n}} - \bar{\rho}_{\mathrm{m}}^{c} \end{pmatrix}. \tag{2.40}$$

As a consequence of the additional degree of freedom due to the neutron spin, the formalism for specular reflectometry has to be extended. The $Q_{l-1,l}$-matrices that have been introduced as 2×2 matrices in Equation (2.28) become 4×4 matrices. Subsequently, the reflectivities for the two non-spin flip channels and the two spin flip channels can be calculated.

It can be seen in Equation (2.36) and (2.40) that a magnetic induction pointing along the quantisation axis does not lead to spin flip scattering. It merely leads to a difference of the scattering length densities for the two neutron spin states. Subsequently, the magnetic scattering length density can be reduced to the value

$$\bar{\rho}_{\mathrm{m}} = -\frac{\mu_{\mathrm{n}} m_{\mathrm{n}}}{2\pi\hbar^2}B. \tag{2.41}$$

Accordingly, the spin up neutrons experience a total scattering length density which is $\bar{\rho}_{\mathrm{n}}^{\mathrm{total}+} = \bar{\rho}_{\mathrm{n}} + \bar{\rho}_{\mathrm{m}}$, while the spin down neutrons experience a total scattering length density which is $\bar{\rho}_{\mathrm{n}}^{\mathrm{total}-} = \bar{\rho}_{\mathrm{n}} - \bar{\rho}_{\mathrm{m}}$.

Figure 2.11 illustrates this special case for the example of the superlattice consisting of ten $YBa_2Cu_3O_7$ (100 Å) / $La_{2/3}Ca_{1/3}MnO_3$ (100 Å) double layers that has been shown for the non-magnetic case in Figure 2.10 *d*. Here, the $La_{2/3}Ca_{1/3}MnO_3$ is assumed to carry a magnetic scattering length density of $1.0 \cdot 10^{-6}\,\text{Å}^{-2}$ which corresponds to a magnetic induction of $2.15\,\mu_{\mathrm{B}}$ per Mn atom. For the spin up neutrons, the contrast between the scattering length densities of the $YBa_2Cu_3O_7$ and $La_{2/3}Ca_{1/3}MnO_3$ layers almost vanishes, whereas it is enhanced for the spin down neutron. Accordingly, the reflectivity curve calculated for the spin up neutrons shows mainly Kiesig fringes, while the one for the spin down neutrons shows enhanced superlattice Bragg reflexes.

It is important to note here, that a reflectivity curve measured with unpolarised neutrons (the same amount of spin up and spin down neutrons) on a magnetic sample is not necessarily the same as the reflectivity curve measured on a non-magnetic but otherwise identical sample. The fact, that $\bar{\rho}_{\mathrm{n}}^{\mathrm{total}}$ averaged over the same amount of spin up and spin down neutrons reduces to $\bar{\rho}_{\mathrm{n}}$ may be misleading. The point is, that the reflectivity does not depend linearly on $\bar{\rho}_{\mathrm{n}}^{\mathrm{total}}$. To illustrate this, the reflectivity curve calculated for the non-magnetic sample from Figure 2.11 is shown in Figure 2.12 compared to the unpolarised (sum of the spin up and the spin down) reflectivity curve for the magnetic sample. The difference between the two curves reveals, that a magnetic signal can also be observed with unpolarised neutrons.

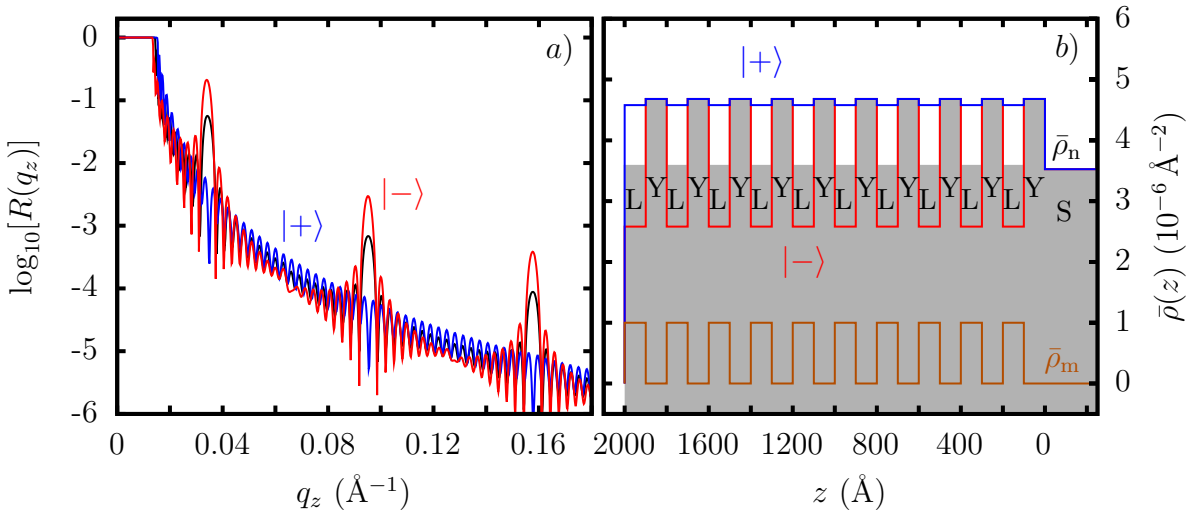

Figure 2.11: *a*) Polarised neutron reflectivity curves calculated for a superlattice consisting of ten $YBa_2Cu_3O_7$ (100 Å) / $La_{2/3}Ca_{1/3}MnO_3$ (100 Å) double layers by assuming the $La_{2/3}Ca_{1/3}MnO_3$ layers to be ferromagnetic. The magnetisation has been assumed to arise from the Mn-ions that carry an average magnetic moment of 2.15 μ_B per Mn atom oriented along the quantisation axis. The blue curve shows the reflectivity calculated for the spin up neutrons ($|+\rangle$) and the red curve shows the reflectivity calculated for the spin down neutrons ($|-\rangle$). The black curve shows the non-magnetic case (same as in Figure 2.10 *d*). *b*) Model of the scattering length density profiles used for the calculated reflectivity curves shown in *a*. The grey shaded area is the nuclear scattering length density profile and the orange line is the magnetic scattering length density profile. The spin up neutrons experience the sum of the two (*blue line*), while the spin down neutrons experience the difference between the two (*red line*). The different layers are marked with "Y" for $YBa_2Cu_3O_7$ and "L" for $La_{2/3}Ca_{1/3}MnO_3$. The $SrTiO_3$ substrate is marked with "S".

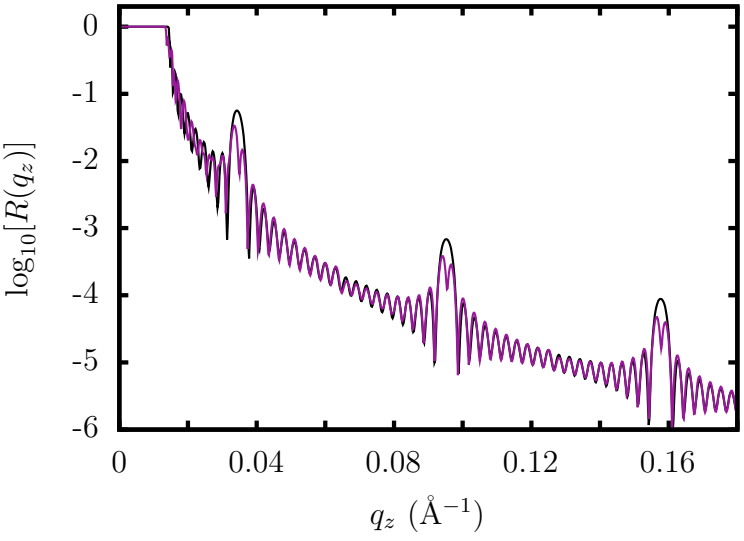

Figure 2.12: Neutron reflectivity curves calculated for a superlattice consisting of ten $YBa_2Cu_3O_7$ (100 Å) / $La_{2/3}Ca_{1/3}MnO_3$ (100 Å) double layers. The black curve shows the reflectivity in the non-magnetic state and the violet curve shows the reflectivity of unpolarised neutrons if the $La_{2/3}Ca_{1/3}MnO_3$ layers contain an average magnetic moment of 2.15 μ_B per Mn atom. This illustrates that magnetism can be observed with unpolarised neutrons.

Treatment of Surface and Interface Roughness

So far, the sample surface and interfaces have been assumed to be perfectly flat and sharp. In reality, this is never the case. All surfaces and interfaces contain a certain roughness that is a lateral variation of the surface or interface position in z. In case of a chemical interdiffusion, interfaces can additionally be blurry and consist of a more or less continuous transition from one layer to the next one. Roughness and interdiffusion can be modelled in the above described formalism by introducing several thin layers at the position of the roughness or interdiffusion zone of the interface which have only small changes in the potential. These layers are introduced to level out the difference between the potentials of the two adjacent layers in small steps over the interdiffusion zone. In order to flatten the nonetheless occurring potential steps in the formalism, a statistical approach is used. Therefore, the position in z of the interface (surface) with index l is assumed to vary depending on the lateral position $\boldsymbol{r}_\parallel$ around z_l:

$$z_l(\boldsymbol{r}_\parallel) = z_l + U_l(\boldsymbol{r}_\parallel). \tag{2.42}$$

The variation $U_l(\boldsymbol{r}_\parallel)$ of the interface position around its mean value can be described by a probability distribution that has the expectation value $\left\langle U_l(\boldsymbol{r}_\parallel)\right\rangle = 0$. In most cases, the best description is obtained with the Gaußian distribution

$$p(U_l) = \frac{1}{\sqrt{2\pi}\sigma_l} \exp\left(-\frac{U_l^2}{2\sigma_l^2}\right), \tag{2.43}$$

where σ_l is the root mean square (rms) roughness of the surface or interface. Based on this distribution, a roughness correction of the Fresnel coefficients can be calculated [81, 82]. Subsequently, the corresponding correction of the $Q_{l-1,l}$-matrices from the above introduced matrix formalism becomes

$$Q'_{l-1,l} = P_{l-1,l} Q_{l-1,l} \tag{2.44}$$

with

$$P_{l-1,l} = \begin{pmatrix} \exp\left(-\frac{1}{2}(k_l - k_{l-1})^2\sigma_l^2\right) & 0 \\ 0 & \exp\left(-\frac{1}{2}k_l k_{l-1}\sigma_l^2\right) \end{pmatrix}. \tag{2.45}$$

Hence Equation (2.30) has to be modified to

$$\begin{pmatrix} t_0 \\ r_0 \end{pmatrix} = \prod_{l=1}^{N} P_{l-1,l} Q_{l-1,l} \begin{pmatrix} t_N \\ 0 \end{pmatrix} = M \begin{pmatrix} t_N \\ 0 \end{pmatrix} = \begin{pmatrix} M_{11} & M_{12} \\ M_{21} & M_{22} \end{pmatrix} \begin{pmatrix} t_N \\ 0 \end{pmatrix}. \tag{2.46}$$

Figure 2.13 shows three calculated reflectivity curves that illustrate the effect of statistical roughness. They have been calculated based on the previously introduced model of the superlattice consisting of ten $YBa_2Cu_3O_7$ (100 Å) / $La_{2/3}Ca_{1/3}MnO_3$ (100 Å) double layers in the non-magnetic state. A reference curve (black line) shows the reflectivity calculated by assuming the surface and the interfaces to be perfectly flat. A second reflectivity curve (blue line) has been calculated by assuming a rms surface roughness

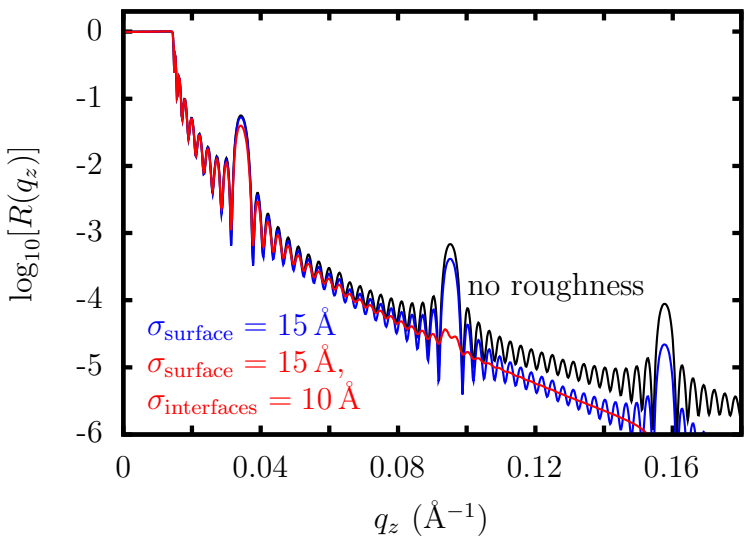

Figure 2.13: Effect of roughness on the neutron reflectivity curve calculated for a superlattice consisting of ten $YBa_2Cu_3O_7$ (100 Å) / $La_{2/3}Ca_{1/3}MnO_3$ (100 Å) double layers in the non-magnetic state. The reflectivity for a perfect flat sample (*black*) is compared with the one for a sample with an rms surface roughness of $\sigma_{\text{surface}} = 15$ Å (*blue*) and the one for a sample with $\sigma_{\text{surface}} = 15$ Å and $\sigma_{\text{interfaces}} = 10$ Å (*red*).

of $\sigma_{\text{surface}} = 15$ Å. Here, the overall value of the reflectivity decreases faster than in the reference curve with $\sigma_{\text{surface}} = 0$ with increasing q_z. The third curve (red line) shows the reflectivity calculated by assuming a rough surface ($\sigma_{\text{surface}} = 15$ Å) combined with rough interfaces ($\sigma_{\text{interfaces}} = 10$ Å). The rough interfaces lead to a strong intensity loss of the higher order superlattice Bragg reflexes and of the Kiesig fringes at large q_z-values.

The above model for statistical roughness describes only a random variation of the interface position around its mean value and blurry interfaces. It does not describe a correlation of the roughness. In case of a lateral correlation of an interface roughness or if the roughness of an interface follows the one of the next interface (vertically correlated roughness), the statistical approach is not valid. In the correlated case, coherent diffuse scattering may occur. Generally, this scattering is several orders of magnitude weaker than the specular reflectivity. It occurs at the position of the specular reflectivity and of the off-specular reflectivity. It can be modelled and calculated by the so-called *distorted wave born approximation* (DWBA) [83, 84, 85] and added to the specular reflectivity which has been calculated with the formalism shown above. The formalism of DWBA is very complicated and has not been used in the present work, because no significant off-specular scattering could be observed or identified.

Instrument Resolution

The instrument resolution of a reflectometry instrument is determined by the uncertainty $\Delta\boldsymbol{q}$ of the measured momentum transfer vector $\boldsymbol{q}$. Under the assumption of a spatially homogeneous but incoherent source it can be estimated by determining the uncertainties of the instrument angles measured and of the wavelength used [82, 86]. In the case of an angular dispersive instrument, the uncertainty of the wavelength used is determined by the mosaicity of the monochromator crystal. In the case of an energy dispersive instrument, it is determined by the energy resolution of the chopper system.

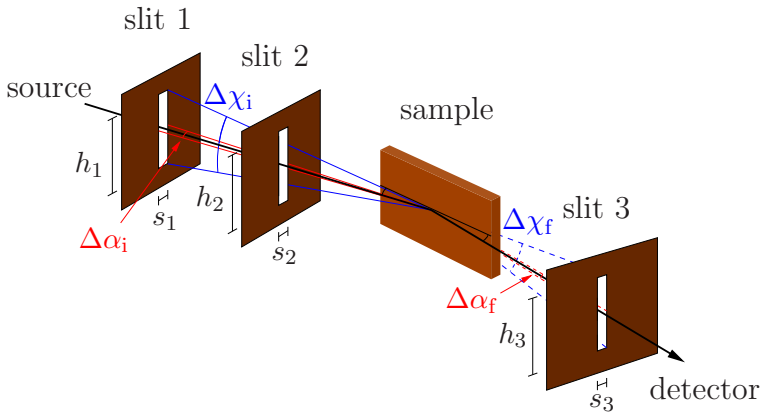

Figure 2.14: Sketch of the geometry of a reflectometer. The first slit defines the divergence of the incoming beam, while the second one defines the illuminated area and reduces the background signal. The third slit defines the divergence of the beam accepted by the detector. Sometimes, there is an additional slit inserted between the third slit and the sample, which reduces the background signal further.

The uncertainties of the measured instrument angles are determined by the slits that are used to define the cross section of the probe beam (see Figure 2.14). If the entire sample is illuminated by the beam, i. e. if the sample is small, the divergence $\Delta\alpha_i$ of the incident beam in the scattering plane depends on the width s_1 of the first slit and on the distance a_1 between this slit and the sample ($\Delta\alpha_i \approx s_1/a_1$). Similarly, the divergence $\Delta\chi_i$ of the incoming beam in the sample plane depends on the height h_1 of the first slit and the on the distance a_1 between the slit and the sample ($\Delta\chi_i \approx h_1/a_1$). In analogy, the divergence of the reflected beam which is still accepted by the detector is determined by the opening of the third slit and its distance to the sample ($\Delta\alpha_f \approx s_3/a_3$ and $\Delta\chi_f \approx h_3/a_3$).

Based on the uncertainties of the angles measured and of the wavelength used, the instrument resolution $\Delta\boldsymbol{q}$ can be estimated with a Gaußian error propagation: In a first step, the derivative of $\boldsymbol{q}$ (Equations (2.8) - (2.10)) is calculated [82, 87]:

$$\delta q_x = \frac{2\pi}{\lambda}\left(-\sin\alpha_f\delta\alpha_f + \sin\alpha_i\delta\alpha_i\right) - \frac{2\pi\delta\lambda}{\lambda^2}\left(\cos\alpha_f - \cos\alpha_i\right) \tag{2.47}$$

$$\delta q_y = \frac{2\pi}{\lambda}\left(\cos\chi_f\delta\chi_f + \cos\chi_i\delta\chi_i\right) - \frac{2\pi\delta\lambda}{\lambda^2}\left(\sin\chi_f + \sin\chi_i\right) \tag{2.48}$$

$$\delta q_z = \frac{2\pi}{\lambda}\left(\cos\alpha_f\delta\alpha_f + \cos\alpha_i\delta\alpha_i\right) - \frac{2\pi\delta\lambda}{\lambda^2}\left(\sin\alpha_f + \sin\alpha_i\right) \tag{2.49}$$

Here, the scattering along q_y has been taken into account for by

$$q_y = \frac{2\pi}{\lambda}(\sin\chi_f + \sin\chi_i), \tag{2.50}$$

even though the angles χ_i and χ_f are put to zero in reflectometry because one integrates over the intensity which is scattered along q_y.

In a second step, the derivatives $\delta\alpha_\mathrm{i}$, $\delta\alpha_\mathrm{f}$, $\delta\chi_\mathrm{i}$, $\delta\chi_\mathrm{f}$ and $\delta\lambda$ are replaced by the uncertainties $\Delta\alpha_\mathrm{i}$, $\Delta\alpha_\mathrm{f}$, $\Delta\chi_\mathrm{i}$, $\Delta\chi_\mathrm{f}$ and $\Delta\lambda$ of the measurement. By assuming these uncertainties to be independent, one can calculate $\Delta\boldsymbol{q}$ in a third step as follows:

$$\Delta q_x = \frac{2\pi}{\lambda}\sqrt{(\sin\alpha_\mathrm{f}\Delta\alpha_\mathrm{f})^2 + (\sin\alpha_\mathrm{i}\Delta\alpha_\mathrm{i})^2 + (\cos\alpha_\mathrm{f} - \cos\alpha_\mathrm{i})^2\left(\frac{\Delta\lambda}{\lambda}\right)^2} \quad (2.51)$$

$$\Delta q_y = \frac{2\pi}{\lambda}\sqrt{(\Delta\chi_\mathrm{f})^2 + (\Delta\chi_\mathrm{i})^2} \quad (2.52)$$

$$\Delta q_z = \frac{2\pi}{\lambda}\sqrt{(\cos\alpha_\mathrm{f}\Delta\alpha_\mathrm{f})^2 + (\cos\alpha_\mathrm{i}\Delta\alpha_\mathrm{i})^2 + (\sin\alpha_\mathrm{f} + \sin\alpha_\mathrm{i})^2\left(\frac{\Delta\lambda}{\lambda}\right)^2} \quad (2.53)$$

In specular reflectometry, the resolution element Δq_z plays the most important role, since the reflectivity R is measured as a function of q_z. According to Equation (2.53), Δq_z depends on the beam divergence, on the angles and the wavelength resolution. Its value depends strongly on the instrument and is not necessarily constant over the measured q_z-range. In the case of a measurement in the angle dispersive mode, the resolution is a non-linear function of the instrument angles. In the case of a measurement in the energy dispersive mode, the resolution is almost linearly proportional to q_z (assuming that $\frac{\Delta\lambda}{\lambda}$ is almost constant over the wavelength range). Figure 2.15 *b* shows the calculated resolution Δq_z for both experimental modes in q_z-dependence. Table 2.1 shows the instrument parameters used for this calculation. These values are characteristic for

Table 2.1: Parameters that have been used to calculate the instrument resolution shown in Figure 2.15 *b*. The beam divergence and $\frac{\Delta\lambda}{\lambda}$ correspond to the ones of the two instruments Morpheus (angular dispersive) and Amor (energy dispersive) at SINQ, Paul Scherrer Institut, Switzerland. On Amor, the accessible range of wavelengths is about 2 - 9 Å. Hence energy dispersive measurements are usually performed at several angles $\alpha_\mathrm{i} = \alpha_\mathrm{f}$ in order to cover the entire q_z-range of interest.

experimental mode:	angular dispersive:	energy dispersive:
$\Delta\alpha_\mathrm{i}$:	0.035°	0.019°
$\Delta\alpha_\mathrm{f}$:	0.147°	0.086°
$\alpha_\mathrm{i} = \alpha_\mathrm{f} = \alpha$:	0 - 3.88°	0.4°, 1.0° and 2.0°
λ :	5 Å	2 - 9 Å
$\frac{\Delta\lambda}{\lambda}$:	1%	7%

the two instruments Morpheus (angle dispersive) and Amor (energy dispersive) at SINQ, Paul Scherrer Institut, Switzerland. Both instruments are located at a quasi-continuous neutron spallation source. On Morpheus, the wavelength is selected with the help of a monochromator. Hence the value $\frac{\Delta\lambda}{\lambda}$ of 1% is relatively small. As a consequence, the

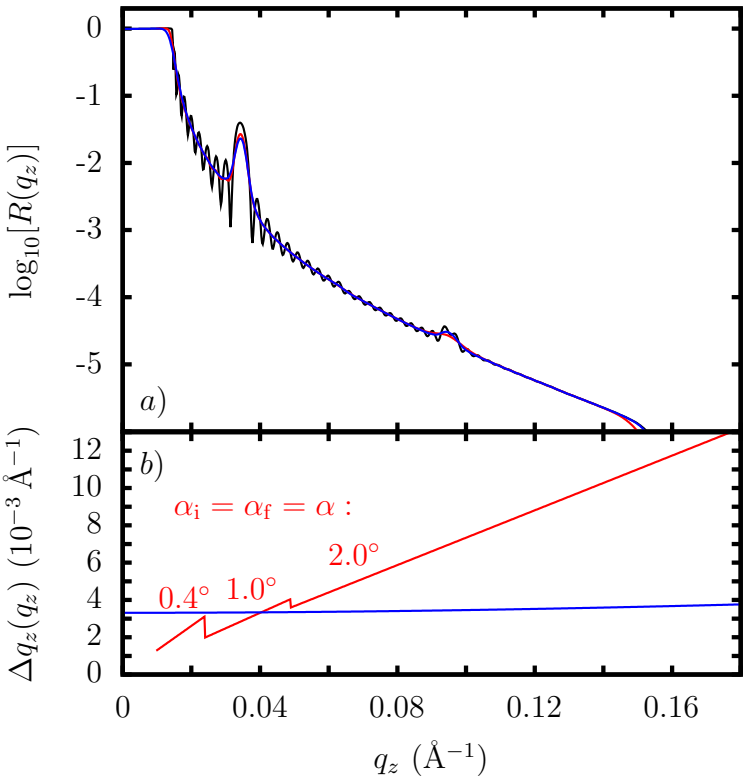

Figure 2.15: Influence of the instrument resolution on reflectivity curves. *a*) The black curve is the reflectivity calculated for a superlattice consisting of ten $YBa_2Cu_3O_7$ (100 Å) / $La_{2/3}Ca_{1/3}MnO_3$ (100 Å) double layers in the non-magnetic state with an rms interface roughness of 10 Å and an rms surface roughness of 15 Å. This curve is convoluted with the resolution function of an energy dispersive instrument (*red*) and with the resolution function of an angle dispersive instrument (*blue*). The parameters of the resolution functions are given in Table 2.1. *b*) The resolution function of an energy dispersive instrument (*red*) and of an angle dispersive instrument (*blue*).

slits before the sample are kept at 0.7 mm in order to obtain a sufficiently high intensity of the beam at the sample position. On Amor, a chopper system cuts bunches out of the continuous neutron beam. For each neutron bunch, the time of flight is measured which the neutrons need to reach the detector. The neutron wavelength is calculated from the time measured. The wavelength resolution $\frac{\Delta\lambda}{\lambda}$ is 7%, which results in a rather large intensity of the neutron beam at the sample position. Accordingly, the opening of the slits in front of the sample can be kept smaller (0.5 mm). As the given range of neutron wavelengths is limited, separate measurements need to be performed at three different angles $\alpha_i = \alpha_f = \alpha$ to cover the q_z-range of interest. Therefore, the resolution Δq_z of the energy dispersive instrument contains two steps. During experiments, these steps are often avoided by keeping the slits opening proportional to the chosen angles $\alpha_i = \alpha_f = \alpha$. This way, the resolution Δq_z becomes a continuous function of q_z. Figure 2.15 *b* shows that the resolution of an energy dependent instrument changes more over the q_z-range of interest and may be better at smaller q_z-values than the one of an angle dispersive instrument.

In the matrix formalism, the instrument resolution can be included as a convolution of the preliminarily calculated reflectivity curve with an instrument resolution function

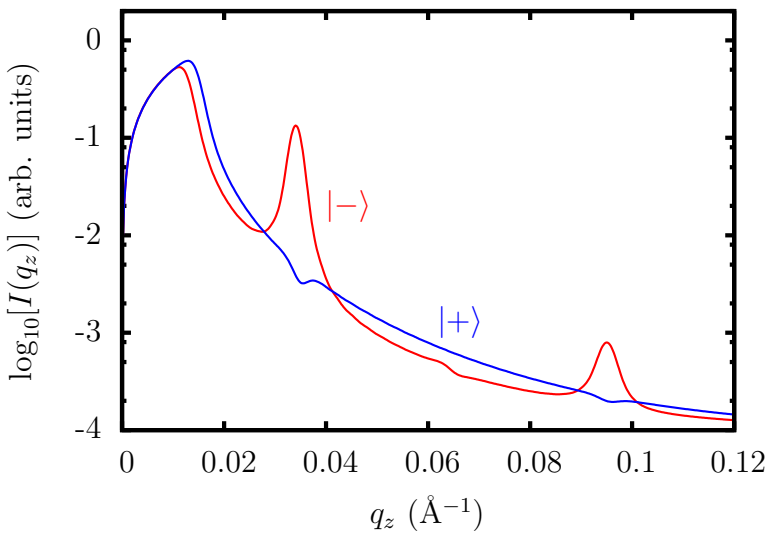

Figure 2.16: Polarised neutron reflectivity curves calculated for the same superlattice as in Figure 2.15 with an additional average magnetic moment of 2.15 μ_B per Mn atom oriented parallel to the quantisation axis. The instrument resolution used is the one of an angle dispersive instrument. The curves have been calculated for spin up neutrons ($|+\rangle$, *blue*) and for spin down neutrons ($|-\rangle$, *red*). The illumination and a constant background have been considered additionally.

that has a Gaußian shape. The full width at half maximum (FWHM) of this Gaußian is Δq_z. Figure 2.15 *a* shows the reflectivity curve calculated for a superlattice consisting of ten $YBa_2Cu_3O_7$ (100 Å) / $La_{2/3}Ca_{1/3}MnO_3$ (100 Å) double layers in the non-magnetic state with an rms interface roughness of 10 Å and an rms surface roughness of 15 Å. It has once been convoluted with the resolution function of an angular dispersive instrument and once with the resolution function of an energy dispersive instrument.

Figure 2.16 shows the final simulation of a polarised neutron reflectometry measurement. The reflectivity curve of the same superlattice as in Figure 2.15 has been simulated by including ferromagnetic $La_{2/3}Ca_{1/3}MnO_3$ layers which contain an average magnetic moment of 2.15 μ_B per Mn atom oriented parallel to the quantisation axis. The same resolution function of an angle dispersive instrument as shown in Figure 2.15 *b* has been used. Since for this type of instrument the intensity of the incident beam is at the sample position proportional to $\sin\alpha_i$, the reflectivity has been multiplied by $\sin\alpha_i$. Finally, a background signal of $1 \cdot 10^{-4}$ has been added to the curves.

Strictly speaking, the curves shown in Figure 2.16 are not reflectivities because they contain the systematic error of the illumination (of the sample). In this work, this correction is applied on the raw data in order to show the reflectivity R instead of the measured intensity I. Accordingly, the reflectivities are compared to simulations, where the illumination has not been included.

Coherence Lengths

Reflectometry is based on the measurement of the probe beam's interference pattern caused by reflections at different interfaces in the sample. The occurrence of the interference pattern requires the coherence of the probe beam, which depends on the beam's source and on the optical elements in the beam path: A source may emit a completely

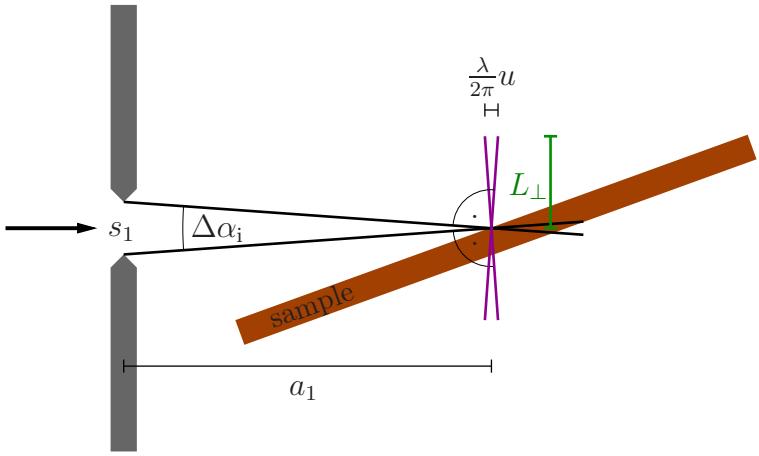

Figure 2.17: Geometrical determination of the beam's coherence length at the sample position perpendicular to the main propagation direction under the assumption of an incoherent but spatially homogeneous source: A slit with opening s_1 is placed between the source and the sample. The coherence length $L_\perp$ (*green*) can be calculated as a function of the divergence of the beam $\Delta\alpha_\mathrm{i} \approx s_1/a_1$ and the beam's wavelength λ (Equation (2.55)). The magenta lines show the fronts of the plane waves that originate from the upper and the lower edges of the slit.

coherent, partially or completely incoherent beam. The optical elements in the beam path subsequently modify this initial coherence of the beam.

Neutron sources for example emit a completely incoherent radiation homogeneously over their volume. A probe beam from such a source is defined by accepting only a certain solid angle of the radiation. From the resulting incoherent beam, a specific neutron wavelength is chosen by the use of a monochromator, a chopper or a velocity selector. Such a wavelength selection makes the beam coherent along its main propagation direction over the length

$$L_\parallel = \frac{\lambda^2}{2\pi\Delta\lambda}u, \tag{2.54}$$

where $\Delta\lambda$ is the uncertainty of the wavelength selection and u is the phase difference (in radian) of two wave fronts which is still accepted as sufficiently coherent. The coherence drops quickly from its maximum value at $u = 0$ due to the accepted phase difference u and reaches zero at $u = 2\pi$. In the literature, commonly a partial coherence of $u = 1$ [86] or $u = \pi$ [82] is accepted.

The coherence of the beam in the scattering plane and perpendicular to its main propagation direction can be achieved by putting a slit with opening s_1 in the beam path. Due to the spatial homogeneity of the source, this perpendicular coherence length of the beam can be estimated by a relatively simple calculation (A sketch of the geometry is shown in Figure 2.17): The waves at the sample position can be assumed to be planar if the sample is placed at a much larger distance a_1 from the slit than the slit opening s_1 ($a_1 \gg s_1$). The resulting divergence of the beam at the sample position is $\Delta\alpha_\mathrm{i} \approx s_1/a_1$.

Subsequently, the wave front originating from one edge of the slit is tilted by the angle $\Delta\alpha_\mathrm{i}$ to the one originating from the second edge of the slit. Assuming that both wave fronts hit the sample at the same position, they split in the scattering plane perpendicular to the wave propagation direction under the angle $\Delta\alpha_\mathrm{i}$. At some distance $L_\perp$ in this perpendicular direction they are separated by $\frac{\lambda}{2\pi}u$ and and are considered to be no longer coherent. Hence the coherence length of the beam in the scattering plane along the direction is $L_\perp$. It can be calculated by the equation

$$L_\perp = \frac{\lambda}{2\pi}\frac{1}{\Delta\alpha_\mathrm{i}}u. \tag{2.55}$$

The coherence $L'_\perp$ of the beam perpendicular to its main propagation direction and perpendicular to the scattering plane can be estimated in analogy to $L_\perp$ from the height h_1 of the slit. For $L'_\perp$, the divergence $\Delta\chi_\mathrm{i} \approx h_1/a_1$ is the important parameter:

$$L'_\perp = \frac{\lambda}{2\pi}\frac{1}{\Delta\chi_\mathrm{i}}u. \tag{2.56}$$

It is evident, that the coherence volume of the incoming beam defined by $L_\parallel$, $L_\perp$ and $L'_\perp$ is very anisotropic. In a similar way, the coherence volume of the scattered beam has an anisotropic coherence volume that is defined by the distance and the opening of the detector. Hence, the coherence volume of the probe beam is a combination of the two volumes. It is usually described in sample coordinates. Nevertheless, it is not trivial to calculate it in real space. It is easier to estimate it in reciprocal space with the help of the instrument resolution (see page 30). In a good approximation, it can be estimated with the equation

$$l_\beta = \frac{2\pi}{\Delta q_\beta}, \tag{2.57}$$

where β runs over the sample coordinates x, y and z [85, 87]. To the best of the author's knowledge, there is no parameter u to be found in the literature for this estimation like it is for the coherence volume of the incident beam (see page 35). As the factor 2π stands for the accepted phase shift, u can even though be assumed to be 2π. Hence, the obtained values for the coherence volume can be considered to be an estimate of the upper limit. Thus, a coherence volume reduced by a factor of 2 is most likely a more appropriate estimate for the coherence volume within which correlation phenomena can be observed.

Any estimate for the coherence volume given in this work is nonetheless obtained from Equation (2.57), which is in its full form:

$$l_x = \frac{\lambda}{\sqrt{\left(\sin\alpha_\mathrm{f}\Delta\alpha_\mathrm{f}\right)^2 + \left(\sin\alpha_\mathrm{i}\Delta\alpha_\mathrm{i}\right)^2 + \left(\cos\alpha_\mathrm{f} - \cos\alpha_\mathrm{i}\right)^2\left(\frac{\Delta\lambda}{\lambda}\right)^2}} \tag{2.58}$$

$$l_y = \frac{\lambda}{\sqrt{\left(\Delta\chi_\mathrm{f}\right)^2 + \left(\Delta\chi_\mathrm{i}\right)^2}} \tag{2.59}$$

$$l_z = \frac{\lambda}{\sqrt{\left(\cos\alpha_\mathrm{f}\Delta\alpha_\mathrm{f}\right)^2 + \left(\cos\alpha_\mathrm{i}\Delta\alpha_\mathrm{i}\right)^2 + \left(\sin\alpha_\mathrm{f} + \sin\alpha_\mathrm{i}\right)^2\left(\frac{\Delta\lambda}{\lambda}\right)^2}}. \tag{2.60}$$

l_x is usually of the order of some 1 - 100 μm, while l_y is only of the order of a few Å and l_z of some 10 μm. The large spread of possible l_x-values has to do with the strong dependence of l_x on α_i and α_f. The comparatively small value of l_y on the other hand has to do with the beam divergence $\Delta\chi_\mathrm{i}$ and $\Delta\chi_\mathrm{f}$ in the sample plane: The slit heights are usually chosen to be larger than the sample width (i. e. in the centimetre range) in order to illuminate the entire sample and subsequently to maximise the measured intensity. This leads to the short coherence length along the y-axis.

The coherence volume in the sample plane has a cigar-like shape. It is usually much smaller than the illuminated sample surface. Subsequently, the measured intensity is the incoherent addition of several coherently scattering volumes on the sample surface. This has a tremendous influence on the observation of correlations within the sample.

Correlation Lengths and the Limitations of the Matrix Formalism

The matrix formalism for the calculation of specular reflectivity curves assumes the coherence lengths of the probe beam to be infinitely long. In the subsection on coherence lengths on page 34 it is shown that this is never the case in a real experiment. The probe beam has always a limited coherence length which leads to limitations of the formalism:

Limitation Due to l_z: Interference phenomena originating from interfaces that are separated by more than l_z do not occur, since the probe beam does not provide the coherence needed. The observed interference pattern is only formed by interferences of structures within the length l_z. Hence the spatial resolution perpendicular to the layers is given by l_z, which is usually 1 - 10 μm. This length scale is considerably longer than the thickness of usually investigated thin film heterostructures and thus rarely causes a limitation.

Limitations Due to l_x and l_y: The coherence lengths l_x and l_y define an area on the sample surface over which the probe beam is coherently scattered. As the illuminated area on the sample surface is much larger than the lateral coherence area of the beam, the measured intensity consists of an incoherent superposition of reflectivities from different areas on the sample surface in which the beam is coherent. Thus, the matrix formalism can only be applied straight forward if the sample is laterally perfectly homogeneous. Accordingly, the following two limitations exist for the application of the formalism:

I) The matrix formalism is applicable, if the sample contains inhomogeneities in the potential that are smaller in size than the laterally coherent area of the probe beam. In this case, the mean value of the potential is taken into account. Additional diffuse coherent scattering may even though occur, if the inhomogeneities are correlated. If the sample contains inhomogeneities that are larger than the laterally coherent area of the beam, the contributions to the reflectivity are added up incoherently. This can be taken into account in the matrix formalism by calculating the reflectivity curves for several potential depth profiles and by adding them up weighted by the surface areas across which the respective profile is valid. Figure 2.18 illustrates that

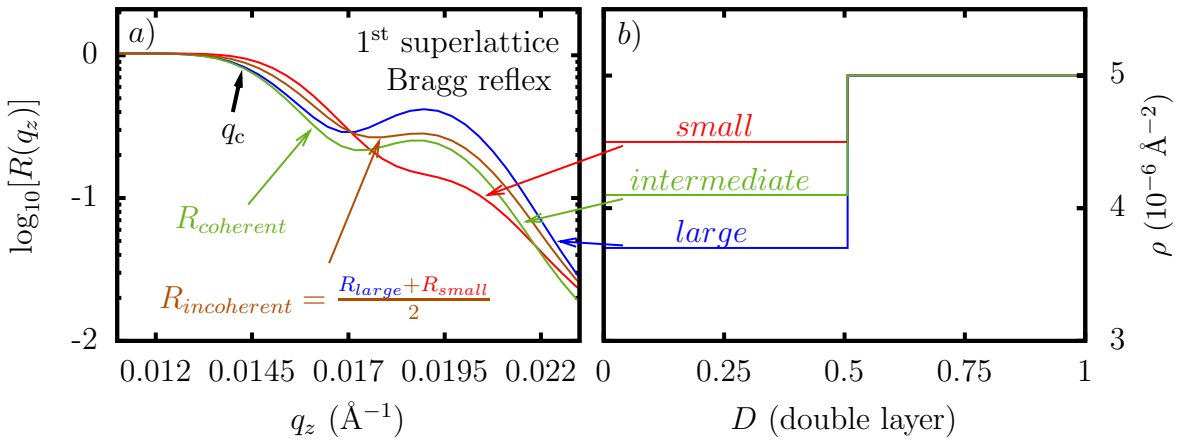

Figure 2.18: Effect of lateral inhomogeneities in the potential and the laterally coherent area of the probe beam on reflectivity curves. *a*) The red, blue and green reflectivity curves are calculated based on the scattering length density profiles shown in *b*. The brown curve is the incoherent addition of the calculated reflectivities of the model with a large and a small contrast between the layers (red and blue curves). The green curve is the reflectivity curve calculated based on the average of the models with the large and the small contrast. The difference between the brown and the green reflectivity curves illustrates, that the incoherent superposition of two reflectivity curves differs from the reflectivity curve based on a coherently averaged profile. *b*) Three models of the scattering length density profile with a small (*red*), an intermediate (*green*) and a large (*blue*) contrast between the layers. The intermediate profile is the average of the red and the blue one. The models contain eight repetitions of the double layer shown here.

the treatment of smaller and larger inhomogeneities described above does not result in the same reflectivity curves.

II) The correlation length of the interface and surface roughness can be smaller or larger than the lateral coherence length of the probing radiation. If it is smaller, it can either be taken into account with a statistical roughness as shown previously on page 29 or it can lead to diffuse coherent scattering, which is not discussed within this work. If however the correlation length of the roughness is larger than the lateral coherence length of the probe beam, one speaks of a *waviness* of the surface or interface. In this case, the measured intensity becomes a superposition of the reflectivities originating from facets that are tilted with respect to each other. In an α_i-α_f-plot, these reflectivities are located at different positions as illustrated in Figure 2.19. It is important to note, that the reflectivity from a wavy surface or interface appears as more than one straight, parallel line on an α_i-α_f-plot. It is thus clearly distinguishable from diffuse, coherent scattering, where the intensity appears mainly on straight lines in q_x-q_z-plots but on bent lines α_i-α_f-plots.

2.2.2 Instrumentation

Neutron reflectometers require a neutron source which provides a sufficiently high neutron flux in order to enable the measurement of reflectivity curves over several orders of

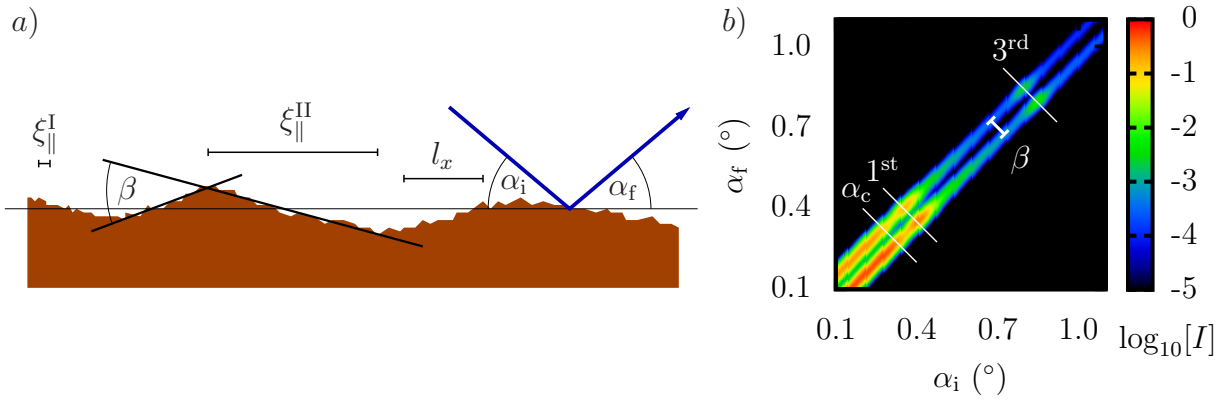

Figure 2.19: *a*) Sketch of a sample with a roughness that is correlated. The two correlation lengths $\xi_\parallel^{\mathrm{I}}$ and $\xi_\parallel^{\mathrm{II}}$ of the sample roughness and the lateral coherence length l_x of the probe beam are indicated. $\xi_\parallel^{\mathrm{I}}$ corresponds to a roughness of the sample surface or the interfaces which is shorter than l_x. The probe beam averages coherently over this roughness. It leads to effects of a statistical rms roughness or to a diffuse coherent scattering. $\xi_\parallel^{\mathrm{II}}$ corresponds to a roughness with a correlation length that is larger than l_x and that is thus called waviness instead of roughness. It is experienced by the beam as separate surfaces that are tilted with respect to each other by the angle β. The angles of the incident beam α_i and of the scattered beam α_f in a measurement are defined with respect to the mean sample plane. *b*) Sketch of an α_i-α_f-plot of a measurement on a superlattice with equally thick layers when assuming the roughness and waviness as indicated in *a*. Due to the waviness, the specular reflectivity appears here on two parallel lines that are separated by the angle β. The position of the edge of total reflection (α_c), the 1st and the 3rd superlattice Bragg reflex are indicated with white lines. If the roughness (correlation length $\xi_\parallel^{\mathrm{I}}$) is correlated from one to the next interface in the superlattice, diffuse coherent scattering occurs. The intensity of this scattering is 2 - 3 orders of magnitude smaller than the one of the specular reflectivity. The diffuse coherent scattering is not shown in this plot.

magnitude in intensity. Such sources are either nuclear reactors or spallation sources. In both cases, the neutrons are moderated in a thermal bath after having been produced. The temperature of this thermal bath determines the energy or wavelength distribution (Boltzmann distribution) of the neutrons, which is usually between 1 and 20 meV (corresponding to neutron wavelengths between about 10 and 2 Å, respectively). After their moderation, the neutrons are extracted from the moderator and guided in so-called *beam guides* to the instruments. The neutron flux in a beam guide at the instrument position depends highly on the neutron source and on the quality of the beam guide. If the source is a nuclear reactor, the neutron flux is high and continuous, while it is either pulsed or quasi continuous at a spallation source. Averaged over time, the neutron flux at a spallation source is about the same as at a nuclear reactor. Accordingly, the pulses at a spallation source carry a very high flux. The pulsed nature of the spallation sources originates from the neutron production by a pulsed, high-energy proton beam that is directed on a target which emits neutrons when being hit by the protons. If the proton pulse frequency is high, the source becomes quasi-continuous, since the time of the neutron moderation becomes larger than the gap between two proton pulses.

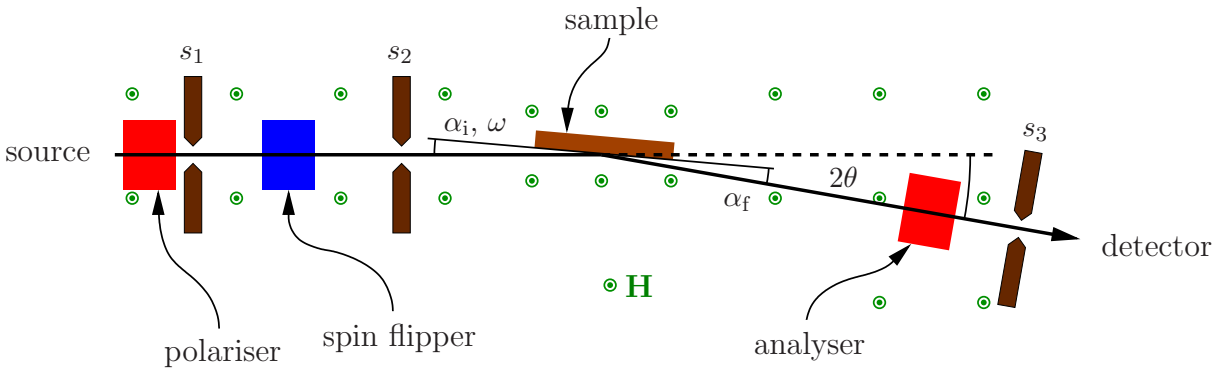

Figure 2.20: Sketch of a polarised neutron reflectometer. Two slits are placed in front of the sample. For a small sample, the first one is used to choose the divergence and hence the resolution of the incident beam, while the second one is used to reduce the background signal. The polariser that is responsible for the neutron polarisation is also placed in front of the sample. If it is only able to polarise the neutrons in one orientation, a spin flipper is used to access the second spin orientation. If the neutron spin polarisation is detected after the sample, an analyser is placed between the sample and the detector. A magnetic guide field is applied in the flight path of the neutrons from the polariser to the sample and, if existing, to the analyser. This guide field defines the quantisation axis of the neutrons and prevents them from depolarising. Normally, the externally applied magnetic field and the guide field are both applied in the sample plane. In this work, they are always applied in the sample plane and perpendicular to the scattering plane.

The neutron reflectometry measurements presented in this work were performed either at a continuous neutron source (FRJ-2 at Forschungszentrum Jülich, Germany, Institut Laue-Langevin in Grenoble, France, and Canadian Institute for Neutron Scattering in Chalk River, Canada) or at a quasi-continuous neutron source (SINQ at Paul Scherrer Institut, Switzerland).

Setup of a Reflectometer

If a neutron reflectometer is working in the angle dispersive mode, a certain neutron wavelength is selected from the beam guide either by a monochromator or by a velocity selector. If a neutron reflectometer is working in the energy dispersive mode, bunches of neutrons of all available wavelengths are used. In the case of a continuous neutron source, these bunches are cut out of the neutron beam by a chopper system. At a pulsed neutron source, this cutting is only needed to shorten the pulse length and to increase the energy resolution of the reflectometer. Knowing the start time of each neutron bunch at the chopper system, the neutron flight time from the chopper to the detector is measured. This allows for the determination of the neutron energy and thus of the neutron wavelengths.

For both experimental modes, a neutron reflectometer is built up as shown in Figure 2.20: Two slits are inserted in the beam between the monochromator, velocity selector or chopper system and the sample. For small samples, the first slit defines the angle resolution of the incident beam, while the second slit is used to reduce the background signal. For large samples, the combination of both slits defines the angle resolution of

the incident beam, while the second slit alone is used to define the illuminated area on the sample surface. A third and sometimes even a fourth slit is inserted between the sample and the detector. If the detector is a point detector, the last slit defines the angle resolution accepted by the detector and reduces the background signal. If the detector is an area detector, it only reduces the background signal. In this case, the angle resolution of the detector is determined by the size of the detector pixels and the distance of the detector from the sample. The intensities measured with the detector pixels on stripes perpendicular to the scattering plane are usually integrated. This leads to a virtual, one dimensional detector which is lying in the scattering plane. The resulting intensity gain is justified by the poor instrument resolution along q_y: For intensity reasons, the slit openings which are oriented parallel to the sample plane are normally as far open as the sample is broad. This way, the entire sample surface is illuminated and the available intensity is maximised.

Apart from some angles and axes to orient and position the sample in the centre of the beam, a reflectometer comprises two relevant physical angles which are movable: The detector can be rotated around the sample by the angle $\alpha_\mathrm{i} + \alpha_\mathrm{f} = 2\theta$, while the sample can be rotated around an axis lying in the centre of its surface by the angle $\omega = \alpha_\mathrm{i}$. Both rotation axes should be identical. The angles ω and 2θ can be driven simultaneously or independently.

Setup for the Neutron Polarisation

If a reflectometer should be capable to perform measurements with polarised neutrons, additional devices are needed. In a first step, the incident neutrons need to be polarised before they reach the sample. This is generally achieved by a polariser consisting of a multilayer system comprising magnetic and non-magnetic layers. The magnetic and the nuclear scattering length densities of the magnetic layers are chosen in a way that their sum matches for one neutron spin state with the nuclear scattering length density of the non-magnetic layers. If the angle of incidence matches the layer thicknesses, the neutrons with this spin state are simply transmitted through the multilayer, while the ones with the other spin state are reflected (see page 24). Hence both the transmitted and the reflected neutrons are polarised. One of the two resulting polarised neutron beams is used for the experiment. The second one is dumped into a neutron absorbing material. In order to switch to the other spin state, one can either reverse the magnetisation of the magnetic layers in the polariser or use a separate spin flipper that is inserted in the neutron beam path after the polariser. There are several types of neutron spin flippers in use. On angle dispersive instruments, most often Mezei-type spin flippers are used. They consist of two solenoids that are oriented perpendicular to each other as well as perpendicular to the neutron flight direction. The outer solenoid compensates the external magnetic field, while the inner one applies a magnetic field H perpendicular to the neutron flight path. Inside of the inner solenoid, the neutrons subsequently perform a Larmor precession with the frequency

$$\omega_\mathrm{L} = \frac{2\mu_\mathrm{n}\mu_0 H}{\hbar} \tag{2.61}$$

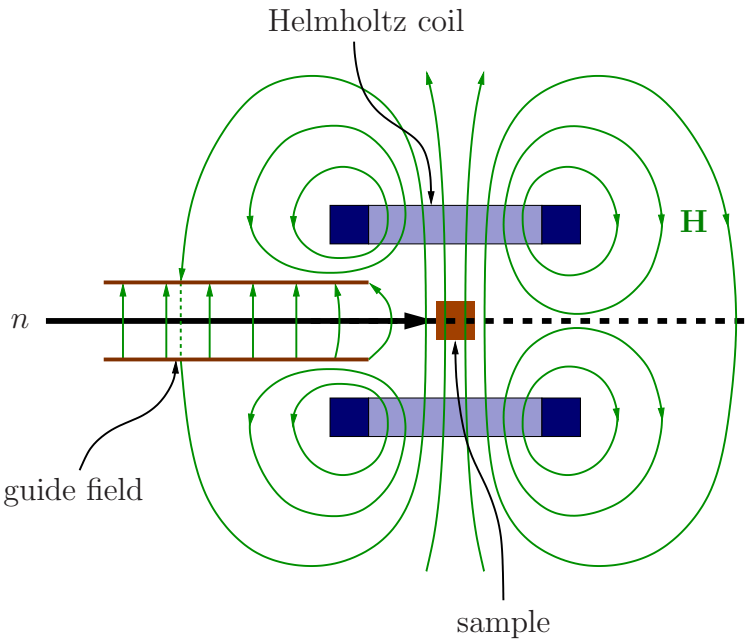

Figure 2.21: An external guide field is used to prevent the neutrons from depolarisation. It overcompensates the stray field of the Helmholtz coils that generate the applied magnetic field at the sample position. The magnetic field in the entire flight path of the neutrons from the polariser to the sample is thus pointing in the same direction. This prevents the neutrons from depolarising before reaching the sample. If the experimental setup also contains a spin analyser, a second guide field is inserted between the sample and the analyser (not shown here).

around H (μ_n is the neutron magnetic moment and μ_0 is the permeability of the free space). If the neutron spin is to be reversed, the current in the inner solenoid is chosen to correspond to a value where the neutron spins perform $n + 1/2$ rotations on the way through the solenoid. No current is applied in the coils if the neutron spin is to be preserved. On energy dispersive instruments, this type of spin flipper does not work because the exposure time to the Larmor field is energy (flight speed) dependent. Hence either an energy independent spin flipper has to be used or the polariser has to be reversed.

After polarising the neutrons, they must be prevented from depolarising. This is achieved by a weak magnetic field which is applied along the neutron's quantisation axis. Generally, such a guide field is generated by a simple setup comprising permanent magnets. It is at least 10 Oe strong. If at the sample position, there is a magnetic field H_{appl} applied, the guide field should be further strong enough to overcompensate the stray field of the magnet (see Figure 2.21). The guide field is usually either applied in the same direction as H_{appl} or it is rotated into this direction shortly before the sample. H_{appl} is mostly oriented in the sample plane, since only magnetic moments perpendicular to the momentum transfer of the neutrons lead to magnetic scattering (see page 24 in subsection 2.2.1). Thus, H_{appl} was always oriented in the sample plane and perpendicular to the scattering plane for the experiments performed in the context of this work.

If, additionally, the neutron spin state is analysed after the sample for spin flip or non-spin flip scattering by the sample, another guide field has to be used from the sample to the analyser. The latter is a system following the same principle as the polariser / spin flipper system. If it is a combination of a polariser and a spin flipper, the flipper is placed

before the polariser. Switching the flipper on and off or reversing the polariser allows for the detector to either measure spin up or spin down neutrons only. This way, the reflectivity can be measured for four neutron spin channels: For the two non-spin flip channels $R_{|+\rangle\to|+\rangle}$ and $R_{|-\rangle\to|-\rangle}$ and for the two spin flip channels $R_{|+\rangle\to|-\rangle}$ and $R_{|-\rangle\to|+\rangle}$.

Neutron Polarisation and Polarisation Correction

The degree of a neutron beam's polarisation is given by the normalised difference between the number of spin up and spin down neutrons in the beam:

$$P = \frac{I^- - I^+}{I^- + I^+}. \tag{2.62}$$

The beam emitted by a neutron source is initially unpolarised ($P = 0$). It becomes polarised by a polariser which removes a certain fraction of neutrons with a particular spin state from the beam. This fraction is never one and hence a beam polarisation of 100% can never be obtained (except for ultra cold neutrons, which are not discussed here). Generally, the polarisation efficiency of a polariser is around 96 - 98%. In order to compare different measurements, it is thus important to know the polarisation efficiency of the components that are responsible for the neutron polarisation. Then, the systematic error of a neutron polarisation of less than 100% can be corrected for.

If the polariser and the analyser side consist of a polariser in combination with a spin flipper, the neutron polarisation at the detector is given by

$$P_{\text{final}} = P_{\text{p}} P_{\text{fp}} P_{\text{fa}} P_{\text{a}}, \tag{2.63}$$

where the indices "p", "a", "fp" and "fa" stand for polariser, analyser, flipper of the polariser and flipper of the analyser, respectively. P_{fp} and P_{fa} are equal to one, if the respective flipper is switched off. If the respective flipper is switched on, the corresponding P-value is slightly smaller than one. In case of Mezei-type spin flippers, it is nonetheless almost one and P_{fp} and P_{fa} can in good approximation be put to one. Subsequently, the final polarisation P_{final} becomes a spin state independent quantity determined by the efficiency of the polariser and the analyser.

If one measures the intensity $I_{\text{non-spin flip}}$ of the direct beam with both polariser and analyser aligned in the same direction and the intensity I_{spinflip} with polariser and analyser aligned antiparallel, one can identify P_{final} by the formula

$$I_{\text{spinflip}} = \frac{1 - P_{\text{final}}}{1 + P_{\text{final}}} I_{\text{non-spin flip}}. \tag{2.64}$$

If the polariser and the analyser are identical devices, the polarisation efficiency of one of them is given by

$$P_d = \sqrt{\frac{I_{\text{non-spin flip}} - I_{\text{spinflip}}}{I_{\text{non-spin flip}} + I_{\text{spinflip}}}}, \tag{2.65}$$

where d stands either for the polariser or for the analyser. The value of P_d is experimentally accessible by measuring the direct beam once of a non-spin flip and once of a spin flip channel [88].

If a measurement has been performed without polarisation analysis but with known polarisation efficiency P_p of the polariser, the measured intensities I_m are known to correspond to the following mixtures of the two spin states:

$$\begin{pmatrix} I_\mathrm{m}^+ \\ I_\mathrm{m}^- \end{pmatrix} = \frac{1}{2} \begin{pmatrix} 1+P_\mathrm{p} & 1-P_\mathrm{p} \\ 1-P_\mathrm{p} & 1+P_\mathrm{p} \end{pmatrix} \begin{pmatrix} I^+ \\ I^- \end{pmatrix} \tag{2.66}$$

Subsequently, the measured intensities can be corrected for the polarisation error and the effective intensities for the spin up and spin down neutrons can be calculated:

$$\begin{pmatrix} I^+ \\ I^- \end{pmatrix} = \frac{P_\mathrm{p}}{2} \begin{pmatrix} 1+P_\mathrm{p} & P_\mathrm{p}-1 \\ P_\mathrm{p}-1 & 1+P_\mathrm{p} \end{pmatrix} \begin{pmatrix} I_\mathrm{m}^+ \\ I_\mathrm{m}^- \end{pmatrix} \tag{2.67}$$

These corrected intensities allow for the comparison of different measurements where the polariser had different efficiencies.

2.3 Magnetometry

The magnetometry measurements presented in this work were performed on a *Physical Property Measurement System* (PPMS) with *Vibrating Sample Magnetometer* (VSM) option from *Quantum Design* [89]. This equipment allows the application of a magnetic field of up to 9 T at the sample position and the probing of the sample's magnetisation with a sensitivity of $(6 \cdot 10^{-7}\,\mathrm{emu} + 3 \cdot 10^{-7}\,\frac{\mathrm{emu}}{\mathrm{T}})/\sqrt{\mathrm{Hz}}$. The setup consists of an outer, superconducting coil to apply a magnetic field at the sample position and an inner, non-superconducting detection coil. Inside the detection coil, the sample is vibrated with a certain frequency and amplitude. The magnetic field originating from the sample is thus vibrating relatively to the detection coil, where it induces an AC-voltage. This voltage is measured and processed with a lock-in technique in order to reduce the noise level of the signal. The amplitude of the processed signal is proportional to the magnetic moment of the sample.

Two different detection coils with an inner diameter of 6.3 mm and 10.16 mm, respectively, were used. Most measurements were performed with the smaller coil with a vibration frequency of 40 Hz and an amplitude of 2 mm. The larger coil was only used for the stress dependent magnetometry measurements presented in Figure 4.27. Due to the rather large weight of the sample holder used for the stress dependent measurements (see Figure 4.25 *e*), the frequency and the amplitude were reduced to 20 Hz and 1 mm, respectively.

3 Sample Preparation and Characterisation

The sample growth technique of pulsed laser deposition is briefly introduced in section 3.1. Subsequently, the relevant growth parameters of the samples are indicated. The sample characterisation is discussed in section 3.2. The characterised quantities are listed in tables at the end of the chapter.

3.1 Sample Growth

All samples investigated in this work were produced by pulsed laser deposition (PLD), which is a technique that is well suited to produce heteroepitaxial thin films with a well defined thickness. It allows the control of the film growth on the level of monolayers and thus the growth of films with very flat surfaces. Changing the deposited material in-situ allows further the growth of different films with atomically flat interfaces on top of each other.

The main parts of a pulsed laser deposition system are an ultra high vacuum sample chamber and an intense, pulsed laser. The sample chamber can be evacuated and back-filled with a specific gas at a certain pressure in order to produce a controlled atmosphere for the sample growth. Inside the chamber, the laser beam is focused onto a target that consists of the same material as the desired film. Its fluence on the target is about $2\,\mathrm{J/cm^2}$ per 25 ns laser pulse. Each pulse creates a plasma at the target surface. This plasma expands rapidly and forms a plume in the space above the target. The plume's shape and size depends on the energy of the laser and on the gas type and pressure in the chamber: Collisions of the plasma ions with the gas modify the energy distributions of the different plasma ions. If the gas is reactive and ionised by the collisions, additional ions may be produced and offered to the plasma. If a certain element in the plasma is not reactive enough, such a reactive atmosphere is required to obtain the correct stochiometry of the growing film.

The substrate for the film growth is typically placed a few centimetres from the target where the plume is as homogeneous as possible. After each laser pulse, ions and neutrals are deposited from the plume on the substrate's surface, where they start to form the film. The crystallographic phase and the orientation of the growing film are determined by the lateral lattice parameters of the substrate and the film material and by the thermal mobility of the atoms deposited on the surface. Both parameters are tuned by the temperature of the substrate, which can be set to any value between room temperature

and 1′000° C. Usually, the temperature is set to obtain a compromise between optimally matching lattice parameters and an optimal atom mobility [90].

A pulsed laser deposition system allows the growth of films with a homogeneous thickness on an area with a diameter of up to 6 - 8 cm, if the substrate is toggled during the growth. This area becomes reduced to 5×5 - $10 \times 10\,\mathrm{mm}^2$, if the substrate is kept fixed. Other limiting factors are the spot size of the laser beam on the target which determines the size of the homogeneous area of the plume and the heating system of the substrate which may limit the area on the substrate where a homogeneous temperature is achieved. As a result of these limitations, the film thickness often decreases from the centre to the border of the substrate. On $10 \times 10\,\mathrm{mm}^2$ substrates, this decrease of thickness is often about 10%.

The samples that were investigated here were superlattices which comprised several repetitions of $YBa_2Cu_3O_7$ / $La_{2/3}Ca_{1/3}MnO_3$ double layers. They had been grown by G. Cristiani in the group of H.-U. Habermeier at the Max Planck Institut für Festkörperforschung in Stuttgart, Germany [72]. The substrates consisted of 0.5 mm thick single crystalline $SrTiO_3$ squares with an area of $10 \times 10\,\mathrm{mm}^2$ that had been polished on one side. This surface was oriented along the crystalline [001] direction with a maximum miscut of 0.3°. The samples had been grown on the polished and cleaned surface at a temperature of 730° C and in an atmosphere of 0.5 mbar oxygen. A laser fluence of $1.8\,\mathrm{J/cm}^2$ enabled a growth rate of 0.059 unit cells $YBa_2Cu_3O_{7-\delta}$ per pulse and 0.026 unit cells $La_{2/3}Ca_{1/3}MnO_3$ per pulse. Both materials had been grown along their *c*-axis. The samples were annealed after growth for one hour at 530° C in 1.0 bar oxygen partial pressure in order to saturate the $YBa_2Cu_3O_{7-\delta}$ CuO-chains with oxygen.

3.2 Sample Characterisation

The structural and electromagnetic properties of the samples were characterised by magnetometry and transport measurements as well as by neutron reflectometry measurements. The transport and reflectometry measurements were performed directly on the samples, while the magnetometry measurements were performed either on small pieces cut off the main samples or on smaller samples that had been grown under the same conditions right before or right after the growth of the main samples. This substitution was necessary because of the limited space in the magnetometer.

The magnetometry measurements were used to determine the saturation moment of the magnetisation, the ferromagnetic phase transition temperature T_{Curie} and the superconducting phase transition temperature T_{sc}. The saturation moment was obtained by measuring the magnetic moment of the sample while driving an M-H-hysteresis loop at 5 K with the external magnetic field applied in the sample plane. Such a measurement is shown in Figure 3.1. It illustrates how the coercive field and the saturation moment are determined and that the saturation field of several Tesla is much larger than the coercive field. On some of the samples, an exchange bias of several ten Oe was observed at low temperatures (see Figure 3.2). The same experimental geometry as for the determination of the saturation moment was used to determine the ferromagnetic phase transition tem-

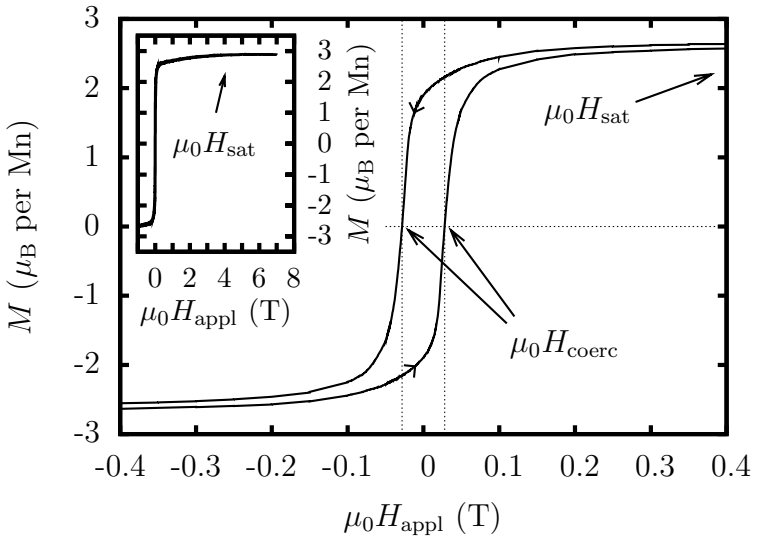

Figure 3.1: M-H-hysteresis loop measured at 5 K on a small piece cut off the sample Y-LCM70. The diamagnetic signal of the $SrTiO_3$ substrate has been subtracted from the data. It is characteristic for all samples that the saturation field H_{sat} of several Tesla (see inset) is much larger than the coercive field H_{coerc}.

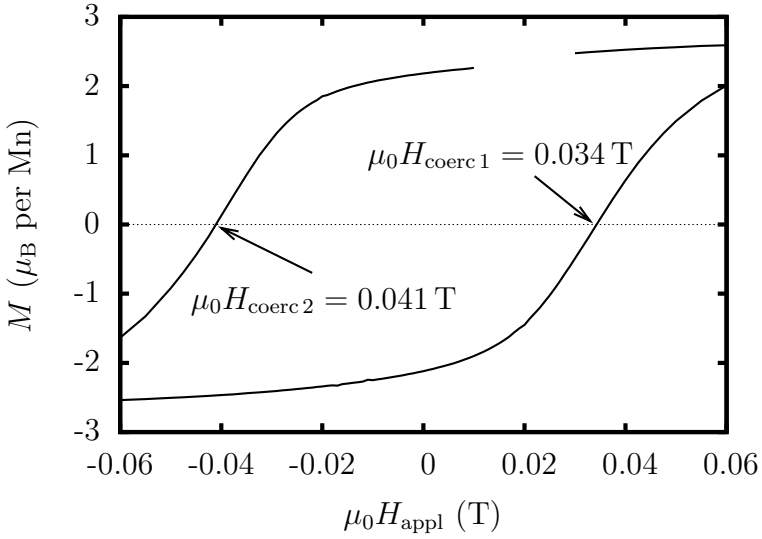

Figure 3.2: M-H-hysteresis loop measured at 5 K on a small piece cut off the sample Y-LCM43. An exchange bias is observed, i. e. the coercive field is for the two magnetisation reversal directions not the same. The curve is shifted by 3.5 mT towards negative values of $\mu_0 H_{\mathrm{appl}}$.

perature T_{Curie}. The only difference was that the magnetic field was kept constant while the temperature was varied during the measurement. Figure 3.3 shows a corresponding measurement on a piece cut off the sample YPr04-LCM1 together with two measurements of the superconducting phase transition temperature T_{sc}. For the latter measurements, a different geometry with the external magnetic field applied perpendicular to the sample plane was used.

The superconducting phase transition temperature T_{sc} was additionally determined by four point transport measurements. It turned out that the T_{sc}-values obtained from magnetometry measurements are some degrees lower than the ones obtained from transport measurements. Most likely, a superconducting percolation path along grain boundaries enables the resistance drop before the entire $YBa_2Cu_3O_7$ layers become superconducting. Thus, the T_{sc}-values given in this work are the ones obtained from magnetometry measurements in order to make sure that the entire $YBa_2Cu_3O_7$ layers are superconducting below this temperature.

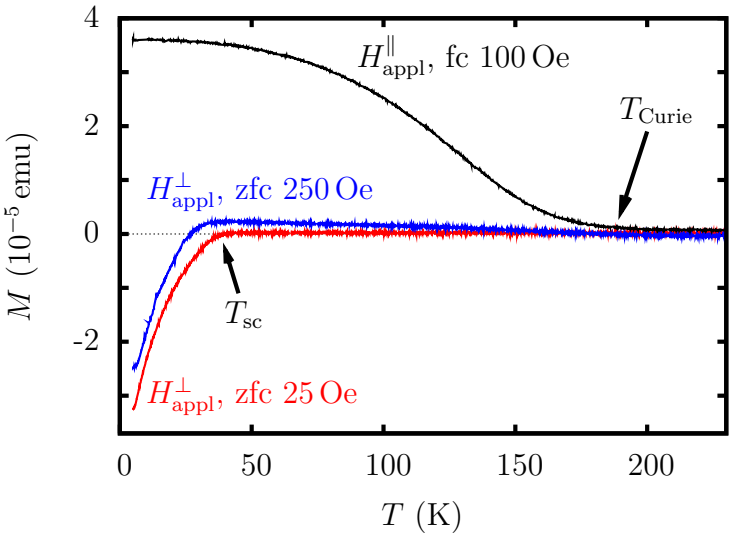

Figure 3.3: The ferromagnetic phase transition temperature $T_{\rm Curie}$ was determined by cooling the sample in an external magnetic field of $H_{\rm appl} = 100\,{\rm Oe}$ applied in the sample plane. The superconducting phase transition temperature $T_{\rm sc}$ was determined by cooling the sample in zero magnetic field and measuring while heating up in a field applied perpendicular to the layers. Sample: YPr04-LCM1

The phase transition temperatures and the saturation moments that were obtained from the magnetometry measurements are shown in Table 3.1 together with the transition temperature T', where the deviation between the nuclear and the magnetic potential depth profile evolves. The values of T' were determined during the main neutron reflectometry experiments presented in section 4.2. Table 3.2 shows the thickness of the individual $YBa_2Cu_3O_7$ and $La_{2/3}Ca_{1/3}MnO_3$ layers which was determined from neutron reflectometry measurements at room temperature and simulation calculations according to the formalism explained in subsection 2.2.1. This table shows additionally a list of the number of $YBa_2Cu_3O_7$ / $La_{2/3}Ca_{1/3}MnO_3$ double layers in the superlattices.

Table 3.1: Phase transition temperatures and magnetic saturation moments of the samples.

sample:	$T_{\rm Curie}$:	T':	$T_{\rm sc}$:	saturation moment at 5 K:
Y-LCM43	165 K	120 - 150 K	75 K	3.2 $\mu_{\rm B}$ per Mn atom
Y-LCM70	240 K	145 K	80 K	2.9 $\mu_{\rm B}$ per Mn atom
Y-LCM75	180 K	140 K	60 K	—
YPr04-LCM1	190 K	—	40 K	2.4 $\mu_{\rm B}$ per Mn atom
YPr04-LCM6a	—	—	40 K	—

Table 3.2: Thickness of the individual layers and the number of YBCO / LCMO double layers.

sample:	thickness YBCO:	thickness LCMO:	N° of double layers:
Y-LCM43	98 Å	98 Å	7
Y-LCM70	256 Å	256 Å	8
Y-LCM75	141 Å	131 Å	16
YPr04-LCM1	100 Å	100 Å	10
YPr04-LCM6a	85 Å	85 Å	13

4 Experiments

The main experimental results of this work are presented in this chapter. In section 4.1, the influence of (001)-oriented $SrTiO_3$ substrates on the structural properties of superlattices grown on top is discussed. For this reason, x-ray diffraction and reflectometry measurements are presented that were performed on a superlattice which comprises ten $Y_{0.6}Pr_{0.4}Ba_2Cu_3O_7$ (10 nm) / $La_{2/3}Ca_{1/3}MnO_3$ (10 nm) double layers. In section 4.2, a deviation of the depth profile of the magnetic induction from the structural depth profile is discussed. Corresponding polarised neutron reflectometry measurements are presented which were performed on different $YBa_2Cu_3O_7$ / $La_{2/3}Ca_{1/3}MnO_3$ superlattices. In section 4.3, a giant, superconductivity-induced modulation of the magnetic induction profile is discussed which was observed in $Y_{0.6}Pr_{0.4}Ba_2Cu_3O_7$ / $La_{2/3}Ca_{1/3}MnO_3$ superlattices, where the $YBa_2Cu_3O_7$ layers were strongly underdoped. Neutron reflectometry and magnetometry measurements are presented. In section 4.4, the magnetisation reversal process in a $YBa_2Cu_3O_7$ (25.6 nm) / $La_{2/3}Ca_{1/3}MnO_3$ (25.6 nm) superlattice comprising eight double layers is discussed. Polarised neutron reflectometry measurements are presented which were performed while the applied magnetic field was cycled on an M-H-hysteresis loop.

4.1 Structural Investigations

The influence of (001)-oriented $SrTiO_3$ (STO) substrates on multilayers grown on top is discussed here. In particular, x-ray diffraction and reflectometry measurements are presented which were performed on a sample comprising ten $Y_{0.6}Pr_{0.4}Ba_2C_3O_7$ (10 nm) / $La_{2/3}Ca_{1/3}MnO_3$ (10 nm) double layers grown on top of an STO substrate. The area of the substrate surface with the superlattice on top was $10 \times 10\,mm^2$ and the substrate thickness was 0.5 mm. In the first part, the instrumentation used for the measurements is introduced. Afterwards, the experimental results are presented. The structural phase transitions of the STO substrate (see subsection 2.1.4) are identified in scans on the STO (002) Bragg reflex. The influence of these transitions on the substrate surface and on the superlattice is determined with scans on the 1st superlattice Bragg reflex. Subsequently, the stress and relaxation behaviour of the superlattice is worked out. In the last part, the results are interpreted and the general implications for multilayers grown on STO (001) substrates are discussed. The main results have been published in Ref. [91].

4.1.1 Instrumentation

The experiments presented here were performed with hard x-rays at the Material Science (MS) beamline of the Swiss Light Source (SLS) at the Paul Scherrer Institut (PSI) in Villigen, Switzerland. The energy of the x-rays was set to 8.5 keV with a beam cross section of $2 \times 2\,\mathrm{mm}^2$. The alignment and rotation of the sample and the detector were achieved with a 2+3-circle surface diffractometer from Micro-Controle Newport that had been equipped with a Physik Instrumente hexapod [92]. The sample was mounted in a closed cycle refrigerator attached to the hexapod. The accessible temperature range at the sample position was 18 - 300 K.

In order to determine the alignment of the STO crystallites that evolve in the low temperature phases, the scans were performed at two sample positions before and after rotating the sample around its surface normal by 90°. In the following, these directions are referred to as the *a*- and *b*-direction. Due to a slight misalignment of the sample rotation axis along the surface normal and the incident x-ray beam, the position of the probed area on the sample surface varied slightly between the measurements for the two orientations. Nonetheless, this cannot be primarily responsible for the results presented, since they were reproducibly obtained in different experiments and for several other samples.

4.1.2 Structural Characterisation of the $SrTiO_3$ Substrate

The STO substrate was characterised on the (002) Bragg reflex. At this point, the x-rays have an effective penetration depth of about $7\,\mu$m, i. e. they probe the surface-near region. Two types of scans were used: In the first type of scans (*rocking scans*), the angles of the incident beam α_i and of the scattered beam α_f were varied in a way that the sum of the two was kept constant ($\alpha_\mathrm{i} + \alpha_\mathrm{f} = 2\theta = constant$). 2θ is then the total scattering angle relative to the incident beam. If 2θ is chosen to correspond to the length of the STO unit cell along the *c*-axis, the alignments of the crystallites' *c*-axes are probed. In the second type of scans ($\theta/2\theta$-*scans*), α_i and α_f were varied by equal amounts ($\alpha_\mathrm{i} = \alpha_\mathrm{f}$) in order to probe the length of the crystallites' unit cells along the *c*-axis.

Figures 4.1 *a* and *b* display rocking curves at different temperatures at the position of the STO (002) Bragg reflex along the *a*- and *b*-directions, respectively. The lineshapes exhibit a distinct broadening below 90 K, which is considerably more pronounced for the *a*- than for the *b*-direction. The curves consist of a superposition of several Bragg reflexes which are shifted in angle with respect to each other. This indicates that the x-ray beam is probing several crystallites with different *c*-axis orientations. The size of these crystallites must exceed the size of the coherence volume of the incident beam ($\approx 1\,\mu\mathrm{m}^3$) but be significantly smaller than the entire probed volume ($\approx 1\,\mathrm{mm}^3$). Notably, the lineshape broadening is entirely absent at 90 K, while it is already clearly visible at 60 K. This suggests, that the formation of the crystallites is related to the structural transition at $T_\mathrm{STO}^\mathrm{II} \approx 65\,\mathrm{K}$ rather than to the antiferrodistortive cubic-to-tetragonal phase transition at $T_\mathrm{STO}^\mathrm{I} = 104\,\mathrm{K}$. It is remarkable that the domain formation observed below $T_\mathrm{STO}^\mathrm{II}$ involves a much larger *c*-axis tilting than the one reported in Ref. [59] at $T_\mathrm{STO}^\mathrm{I} = 104\,\mathrm{K}$. This difference is most likely related to the fact that the experiment in Ref. [59] was

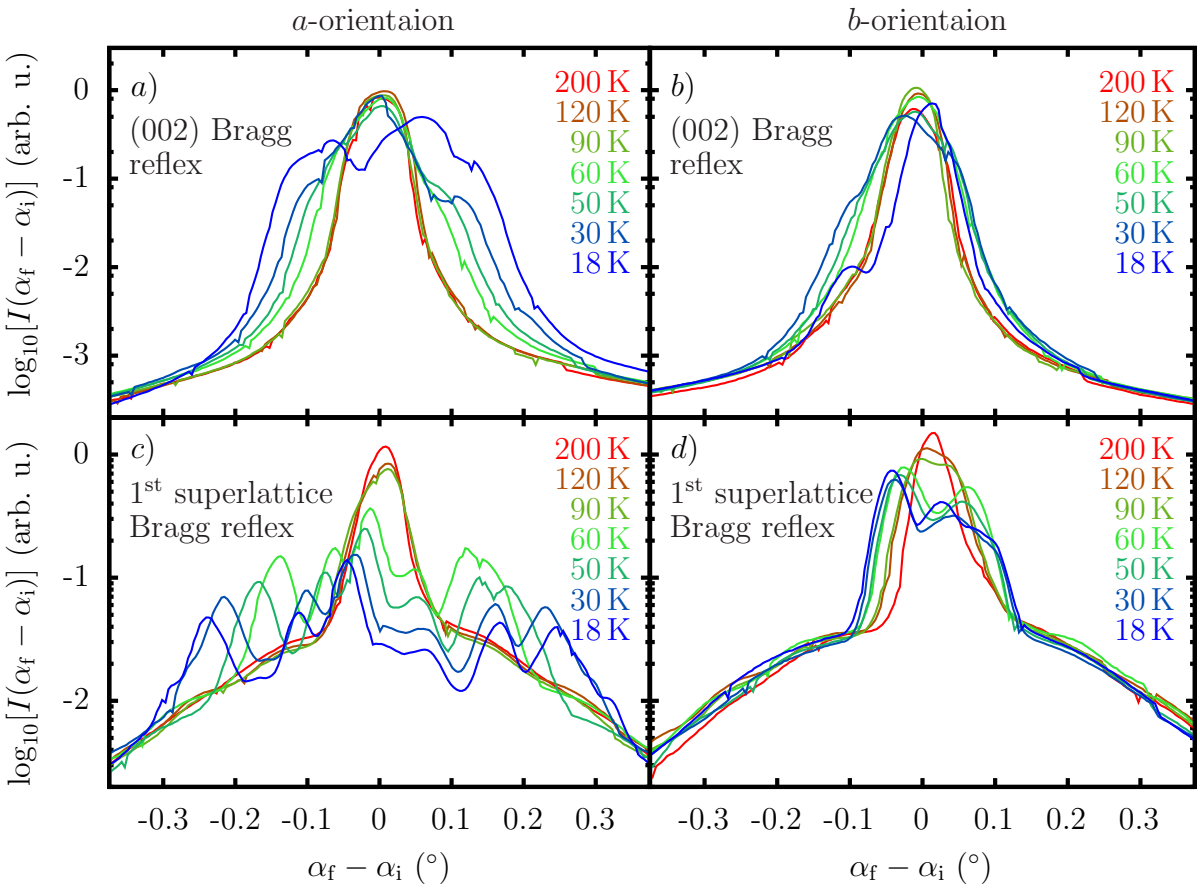

Figure 4.1: *a*) and *b*): Rocking curves (plotted as angle of scattered beam α_f versus angle of incident beam α_i) on the $SrTiO_3$ (002) reflex measured in temperature dependence along the *a*- and *b*-direction, respectively. *c*) and *d*): Rocking curves at the position of the 1st superlattice Bragg reflex measured along the *a*- and *b*-direction as a function of temperature. Sample: YPr04-LCM1

sensitive to much weaker distortions, since the probed volume was about four orders of magnitude smaller than in the experiment presented here. Hence the signal consisted of a superposition of less crystallites with different *c*-axis alignments. Therefore smaller *c*-axis tiltings could be observed.

A second anomaly in the lineshape is observed between 30 K and 18 K: A narrowing occurs along the *b*-direction while an additional broadening occurs along the *a*-direction. This unusual behaviour happens in a temperature range, where in ^{18}O-substituted STO the ordering of the Ti-ions combined with ferroelectricity has been reported [48, 51] and where in ordinary STO uniaxial stress-induced ferroelectricity has been reported [52].

Additionally, $\theta/2\theta$-scans were performed at the position of the STO (002) Bragg reflex for the *a*- and *b*-directions and hence for the corresponding probed volumes (see Figure 4.2). In the cubic state, the *c*-axis lattice parameters were determined as 0.3905, 0.3898 and 0.3896 nm at 300, 120, and 90 K, respectively, which is in good agreement with the tabulated values in Ref. [50]. The 60 K-scans revealed crystallites with different *c*-axis lattice parameters in the range between 0.3887 nm and 0.3899 nm for the volume

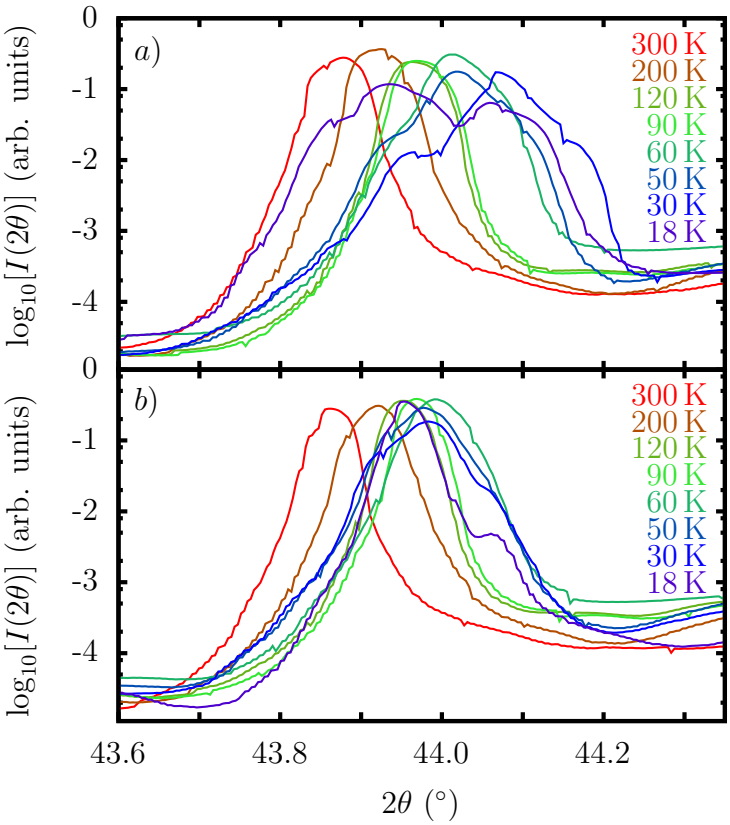

Figure 4.2: Temperature dependent $\theta/2\theta$-scans at the position of the STO (002) Bragg reflex performed along the a- and b-direction, respectively. The probed volumes for the scans along the a- and b-direction are located in the surface-near region and at laterally different positions on the sample surface. Sample: YPr04-LCM1

probed in the scans in the a-direction and a somewhat smaller spread from 0.3893 nm to 0.3899 nm for the volume probed along the b-direction. At 30 K, the lattice parameters got even shorter in the volume probed along the a-direction while they remained almost the same in the one probed along b. Below 30 K, another phase transition takes place as is already shown in the rocking scans in Figure 4.1 a and b. At 18 K, the lattice parameters were between 0.3884 nm and 0.3913 nm in the volume probed along the a-direction, while they only varied between 0.3889 nm and 0.3906 nm for the one probed in b-direction. A similar sudden increase of the lattice parameters along the c-axis at low temperatures has been reported in Ref. [50].

4.1.3 Influence of the $SrTiO_3$-Substrate on the Superlattice

Temperature dependent rocking curves at the position of the 1st superlattice Bragg reflex show a similar broadening as the rocking curves on the (002) STO Bragg reflex in the first place (see Figure 4.1). The largest changes occur below $T_{\mathrm{STO}}^{\mathrm{II}}$, where the lineshapes split up into several reflexes (Figure 4.1 c). This splitting indicates an incoherent superposition of reflections originating from surfaces facets that are tilted relatively to each other. The size of these surface facets must exceed the lateral coherence volume of the x-ray beam which is of the order of micrometers. Corresponding micrometer-sized structural domains had indeed previously been observed by magneto-optical imaging for $La_{2/3}Ca_{1/3}MnO_3$ on STO which yielded a typical domain size of 10-40 μm times several 100 μm [56]. A similar lower limit of the facet size of some 50 μm can be obtained from polarised neutron reflectometry

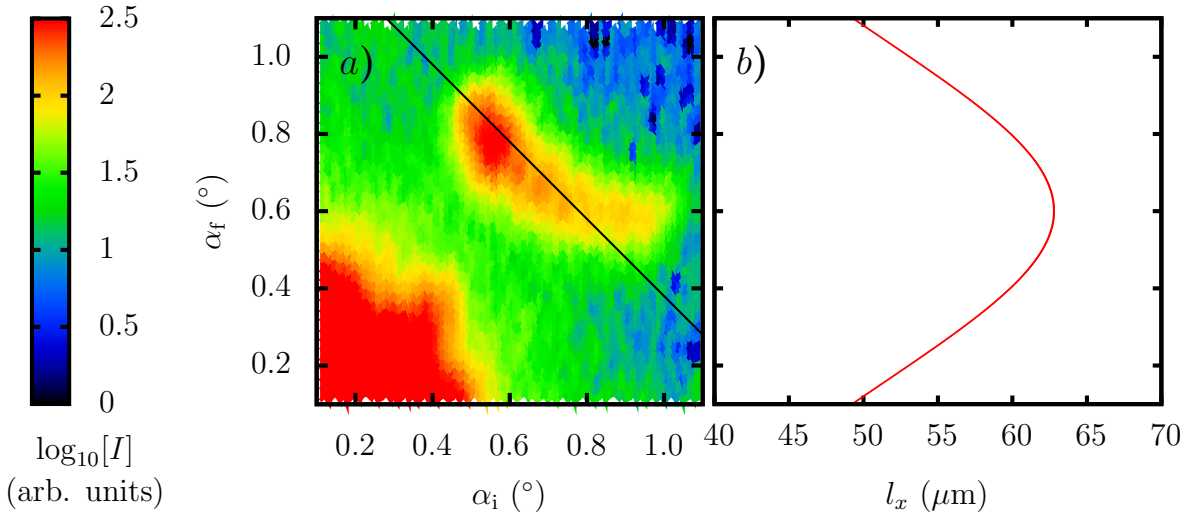

Figure 4.3: *a*) α_i-α_f-plot of an off-specular neutron reflectometry measurement with the sample oriented along the *a*-direction. The measurement was performed at 15 K with a neutron wavelength of 4.41 Å. The black line at $\alpha_i + \alpha_f = 1.38°$ indicates a rocking scan at the position of the 1st superlattice Bragg reflex. The different intensity maxima on the reflex along this rocking scan are caused by the incoherent superposition of several reflecting surface facets (a waviness of the substrate surface). *b*) The lateral coherence length of the neutrons calculated according to the instrument settings (see page 34 in subsection 2.2.1) along the rocking scan at $\alpha_i + \alpha_f = 1.38°$. The surface facets must be larger than this lateral coherence length. Sample: YPr04-LCM1

measurements on the same superlattice by estimating it from the lateral coherence length of the neutrons (see Figure 4.3). The combined x-ray and neutron data thus both provide clear evidence for a waviness of the substrate surface that consists of strongly anisotropic, tilted micrometer-sized facets. The difference in the number of incoherently superposed superlattice Bragg reflexes in Figure 4.1 *c* and *d* suggests, that the extent of the facets is three times longer in the *b*-direction than in the *a*-direction. From the total width of the lineshapes one can derive that these facets are tilted relative to each other by up to 0.5° along the *a*-direction and by up to 0.2° along the *b*-direction. It appears that this facet pattern or waviness involves the entire superlattice including the surface layer of the STO substrate. It is likely to be caused by the structural phase transition of the STO substrate as is suggested by the similarities between the rocking scans on the STO (002) Bragg reflex and the 1st superlattice Bragg reflex. Nevertheless, there are also some noticeable differences: For example, the onset of a broadening of the rocking curves on the 1st superlattice Bragg reflex already occurs at 120 K along the *b*-direction (Figure 4.1 *d*). This suggests that the corresponding surface domains are stabilised by the slight miscut angle of the surface normal with respect to the STO *c*-axis of about 0.26° orientated along the *a*-direction and thus by the strongly anisotropic terraces on the STO surface that have a terrace width of about 86 nm. The second remarkable difference concerns the changes near T_{STO}^{III}. A clear anomaly is observed here for the STO (002) Bragg reflex while no corresponding changes are seen at the multilayer Bragg reflex.

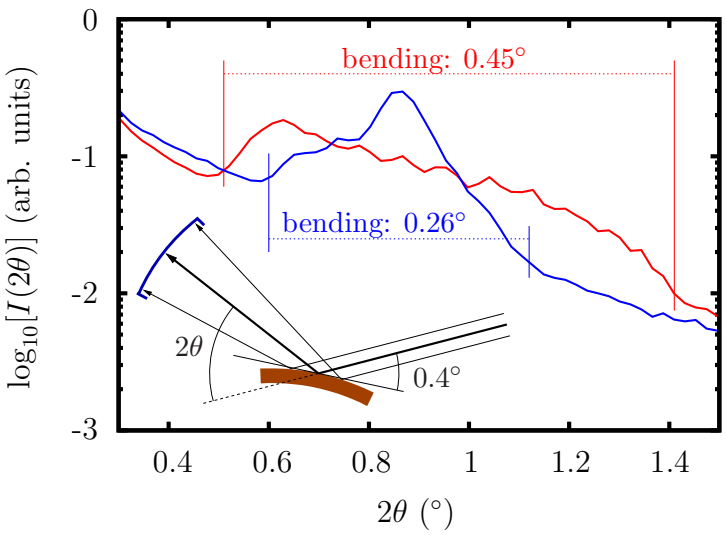

Figure 4.4: Measurement on a time of flight neutron reflectometer at different scattering angles $2\theta = 0.4° + \alpha_f$ (see insert). The intensities are integrated over time (neutron wavelength). The sample was oriented along the a-direction and T was below T_{STO}^{III}. Once the sample had been mounted by preventing its bending (blue) and once by allowing it (red). The precise sample mounting is shown in Figure 4.25 *a* - *d*. Sample: YPr04-LCM6a

The overall behaviour suggests, that as a function of decreasing temperature, structural domains first develop in the immediate vicinity of the STO substrate surface in the form of phase separated tetragonal and cubic crystallites. They propagate from the substrate surface into the superlattice but not deeper into the STO substrate (as predominantly probed at the STO (002) Bragg reflex). Even below the bulk cubic-to-tetragonal transition, the data suggest that these domains are limited to the vicinity of the STO surface region. This situation suddenly changes at T_{STO}^{II}, where a fairly ordered pattern of strongly an- isotropic crystallites (probably due to embedded rhombohedral crystallites [48]) develops even several micrometer down into the STO substrate. This transition gives most likely rise to intrinsic stress in the substrate which is unequal on the upper and lower surface of the substrate since the lower surface is not polished and does not carry a superlattice. This leads most likely to a bending of the entire substrate (see Figure 4.4). Curiously, the observed changes below 30 K seem to be entirely absent in the superlattice and are thus most likely also absent in the topmost surface region of the STO substrate. Since it is known that the temperature T_{STO}^{III} is extremely sensitive to small perturbations like an ^{18}O-substitution in STO, it is conceivable that this transition is suppressed in the STO surface region due to the strain which is imposed by the superlattice.

4.1.4 Stress and Relaxation in the Superlattices

Strain and relaxation in the superlattice and at the interface between the STO substrate and the superlattice were determined by mapping the regions near the (103) and the (013) asymmetric Bragg reflexes of STO. Figure 4.5 shows these mappings at 200 K. They were obtained by performing rocking scans at the respective positions and measuring the diffracted intensities with an area detector. The crystal structure of STO could be

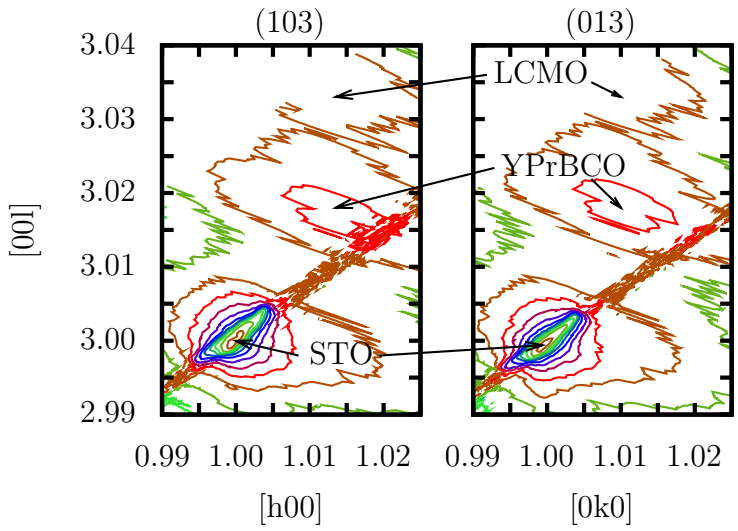

Figure 4.5: Mappings of the asymmetric (103) and (013) STO Bragg reflexes at 200 K. The YPr0.4BCO (109) and (019) Bragg reflexes are visible at (1.014 0 3.18) and (0 1.01 3.18), respectively, while the LCMO (161) Bragg reflex is visible at (1.014 0 3.033) and (0 1.01 3.033). The diagonal lens shape of the STO Bragg reflexes results from the instrument resolution (detector streak), while the diagonal line of noisy signal is due to the filters used to protect the area detector from oversaturation at the position of the main STO peak. The linespacing of the contours corresponds to $0.5 \times \log_{10}[I_{\text{measured}}]$. Sample: YPr04-LCM1

determined from the main peaks as being cubic with a lattice parameter of 0.39005 nm. The lens-like shape of the peaks along the diagonal of the maps is caused by the detector streak and the instrument resolution. The noisy signal on the diagonal line through the main peak is caused by filters inserted in the direct beam to avoid oversaturation in the area detector which reduced the count rate and thus the statistics at the measured point. The shoulders of the main peaks towards larger h and k values but smaller l values indicate that the STO unit cells nearest to the superlattice structure exhibit a lateral shrinking combined with a slightly increased c-axis parameter to fit the $Y_{0.6}Pr_{0.4}Ba_2C_3O_7$ (YPr0.4BCO) ab-plane. The obtained lattice parameters of YPr0.4BCO are $a = 0.385$ nm, $b = 0.386$ nm and $c = 1.163$ nm which is in good agreement with the tabulated values of $a = 0.38334$ nm, $b = 0.39034$ nm and $c = 1.1686$ nm at 300 K [43]. In Figure 4.5 its (109) and (019) Bragg reflexes are located at (1.014 0 3.018) and (0 1.01 3.018), respectively. $La_{2/3}Ca_{1/3}MnO_3$ (LCMO) was found to have the lattice parameters $a = 0.546$ nm, $b = 0.547$ nm and $c = 0.711$ nm, which corresponds to the tabulated values. As given in [56], the larger, orthorhombic LCMO unit cell is rotated by 45° around the c-axis as compared to the one of YPr0.4BCO. Its (161) Bragg reflex is located in the Figure 4.5 at (1.014 0 3.033) and (0 1.01 3.033), respectively.

One can conclude from these mappings that the LCMO layers maintain the same lattice parameters as bulk LCMO. No mismatch between the lateral lattice parameters of the LCMO and the YPr0.4BCO layers was observed. Since the lateral lattice parameters of the latter are slightly increased compared to the tabulated bulk values, the YPr0.4BCO

layers must be tensile stressed. Furthermore, the superlattice induces a compressive stress on the STO substrate: The STO unit cells nearest to the superlattice had reduced lateral lattice parameters and an increased c-axis length.

4.1.5 Results and Interpretation

The hard x-ray and neutron investigations on the structural properties of STO substrates that are presented above lead to the conclusion that the structure of the near-surface region of STO is spatially inhomogeneous. The antiferrodistortive phase transition starts in the near-surface region already at $T_{\mathrm{STO}}^{\mathrm{I'}} \approx 150\,\mathrm{K}$ and yields a mixture of tetragonal and cubic crystallites. Facets develop on the surface that are slightly tilted with respect to each other in the direction perpendicular to the miscut of the surface. The bulk of the substrate remains unaffected by this transition. Around $T_{\mathrm{STO}}^{\mathrm{II}} \approx 65\,\mathrm{K}$, crystallites with a rhombohedral structure form embedded in the otherwise tetragonal crystal matrix. They fill a sizeable fraction of the sample volume. This leads to intrinsic strain and subsequently to a bending of the substrate and a waviness of its surface: Facets are formed in the surface which along the miscut direction of the substrate (bending direction) are tilted relatively to each other by up to 0.5°, while the facets' tilting along the other direction remains considerably smaller. A similar, but slightly weaker tilting behaviour is observed for the orientation of the crystallites' c-axes down to a depth of at least $7\,\mu$m, confirming the bulk properties of the bending. Laterally, the surface facets extend at least 20 - 30 μm along the shorter direction and most likely more than three times this length along the longer direction. The exact shape and tilting angle of the facets depends on the substrate, its miscut, its termination and most likely on the way, the sample is mounted. At $18\,\mathrm{K} < T_{\mathrm{STO}}^{\mathrm{III}} < 30\,\mathrm{K}$, STO undergoes a third phase transition, where the c-axis lattice parameter increases again. This transition was only observed on the STO (002) Bragg reflex but not on the substrate surface. As this transition is extremely sensitive to small perturbations, it is possibly stabilised at the surface by the superlattice grown on top.

In the investigated temperature range from 18 to 300 K thin film single or multilayer systems grown heteroepitaxially on top of STO substrates are exposed to a wealth of different types of stress. In the case of a persistent material like LCMO grown on an STO substrate, this stress can be partially relaxed within the uppermost STO layers without leading to a deformation of the lateral lattice parameters of the material on top. Nonetheless, the transition at $T_{\mathrm{STO}}^{\mathrm{II}}$ and the subsequent bending of the substrate induces a strain in the multilayer system. This strain is most likely large and therefore expected to change the electronic and magnetic properties of the system. Furthermore, the formation of the surface facets that are tilted with respect to each other is expected to imprint a lateral strain pattern into the multilayer and hence break the lateral translation symmetry. This break of symmetry may affect two dimensional electronic systems in superlattices at the interfaces and may modify the magnetic induction in thin layers.

The bending and tilting of the surface facets below $T_{\mathrm{STO}}^{\mathrm{II}}$ influences investigation methods that are performed at gracing incidence. Reflectometry measurements for example are strongly influenced, since the specular reflectivity becomes split into several parallel lines in α_{i}-α_{f}-plots (see Figure 2.19). Unfortunately, the alignment of the instrument on only

one line does not ensure the measurement of a proper specular reflectivity curve, since at lower angles of incidence the substrate bending may shadow parts of the sample surface from the incident beam. This fact has to be taken into account for the interpretation of data obtained at $T < T_{\mathrm{STO}}^{\mathrm{II}}$.

4.2 Depth Profile of the Magnetic Induction

In this section, polarised neutron reflectometry measurements are presented which were performed on $YBa_2Cu_3O_7$ (YBCO) / $La_{2/3}Ca_{1/3}MnO_3$ (LCMO) superlattices grown on $SrTiO_3$ (STO) substrates with (001)-oriententation. In the first part, temperature dependent measurements on three samples with different thickness are discussed and the characteristic transition temperatures are identified. In the second part, the theoretical modelling introduced in subsection 2.2.1 is developed further and applied to the specific features of the data. The results are discussed and interpreted in the last part of this section. Some of the data presented here have been published in Ref. [28].

4.2.1 Temperature Dependence of the Magnetic Depth Profile

Specular neutron reflectometry measurements were performed on three superlattices with nearly equally thick YBCO and LCMO layers which had been grown on (001)-oriented STO substrates. In the first sample (Y-LCM43), all layers had a thickness of 9.8 nm. In the second sample (Y-LCM75), the YBCO layers were 14.1 nm and the LCMO layers were 13.1 nm thick. In the third sample (Y-LCM70), the layers had a thickness of 25.6 nm.

Figure 4.6 displays temperature dependent measurements with unpolarised neutrons on the sample Y-LCM43. The edge of total reflection, the 1$^{\mathrm{st}}$ and 3$^{\mathrm{rd}}$ superlattice Bragg reflexes are visible at all temperatures, even though the latter is almost hidden in the background signal. Below 150 K, the structurally forbidden 2$^{\mathrm{nd}}$ superlattice Bragg reflex appears. The origin of its intensity gain is in the region of the interfaces a deviation of the magnetic induction depth profile from the structural depth profile. This deviation will be discussed in more detail in the following subsection on page 62. In the current subsection, only the temperature of its appearance is of interest.

The shift of the 1$^{\mathrm{st}}$ superlattice Bragg reflex towards smaller q_z-values at $T < 100\,\mathrm{K}$ is a further temperature dependent change in the reflectivity curves. It is caused by the magnetisation dependence of the contrast between the total scattering length densities of the YBCO and the ferromagnetic LCMO layers. As illustrated in Figure 2.11, the magnetisation of the LCMO layers increases the contrast for the spin down neutrons and decreases it for the spin up neutrons. Accordingly, the 1$^{\mathrm{st}}$ superlattice Bragg reflex becomes dominated by the spin down neutrons with decreasing temperature and increasing magnetisation. At the same time, the mean total scattering length density becomes reduced for the spin down neutrons and increases for the spin up neutrons. For the spin down neutrons this leads to a shift of the position of the edge of total reflection towards smaller q_z-values, which pulls the position of the 1$^{\mathrm{st}}$ superlattice Bragg reflex along. For the spin up neutrons, the position of the edge of total reflection is shifted towards larger q_z-values.

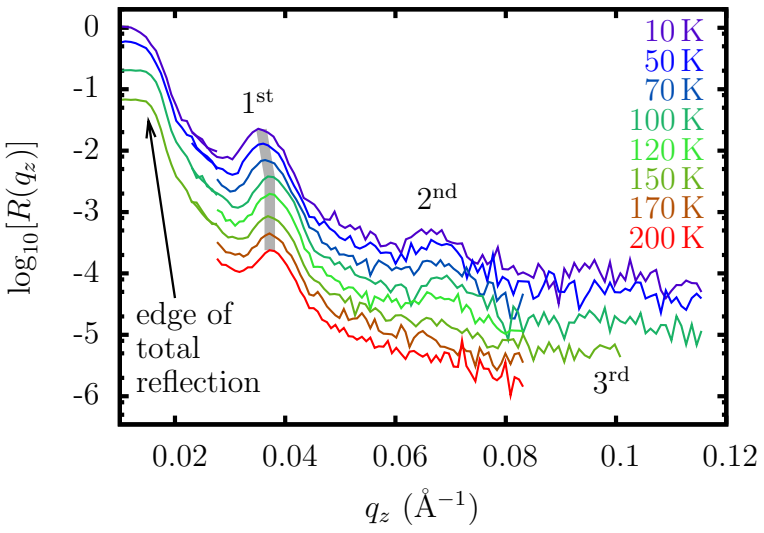

Figure 4.6: Reflectivity curves measured with unpolarised neutrons in an applied magnetic field of about 300 Oe. The maximum position of the 1st superlattice Bragg reflex shifts below 100 K towards smaller q_z-values. The structurally forbidden 2nd superlattice Bragg reflex appears below 150 K. For comprehensibility reasons, the curves are shifted upwards. Sample: Y-LCM43.

Consequently, since the data were obtained with unpolarised neutrons, i. e. comprise the superposed reflectivities of the spin up and spin down neutrons, the edge of total reflection changes its shape at 50 K and 10 K. An additional reason for the pronounced change of the edge of total reflection's shape is the surface facets formation at $T_{\mathrm{STO}}^{\mathrm{II}} \approx 65\,\mathrm{K}$ and the subsequent change of the surface area which is specularly reflecting at gracing angles of incidence (see section 4.1).

In order to get a more detailed picture of the changes described above, temperature scans were performed at the positions of the 1st and the 2nd superlattice Bragg reflex (Figure 4.7). At each point, a rocking scan was performed and the measured intensity was integrated. This way, the reflected intensities of all surface facets that evolve below $T_{\mathrm{STO}}^{\mathrm{II}} \approx 65\,\mathrm{K}$ (see section 4.1) were added up and the total reflecting surface remained constant for all temperatures. Accordingly, it was possible to determine the temperature dependent changes of the reflectivity at the respective positions in q_z. The position of the 1st superlattice Bragg reflex was chosen because it is sensitive to changes in the potential depth profile that have a double layer periodicity. The position of the 2nd superlattice Bragg reflex was chosen because it is most sensitive to changes of the potential depth profile that modify the thickness ratio of the individual layers, i. e. to changes at the interfaces. Below $T_{\mathrm{Curie}} = 165\,\mathrm{K}$, the intensity of the 1st superlattice Bragg reflex increases continuously. The slope of the increase remains constant until $T_{\mathrm{sc}} = 75\,\mathrm{K}$. The reason for this increase is a magnetisation induced change of the contrast between the YBCO and LCMO layers: As the reflectivity depends on the potential consisting of a nuclear and a magnetic part, a change of the magnetic induction results in a change of the measured intensities for the spin up and spin down neutrons. This change of intensities is not levelled out in the unpolarised neutron beam with equal amount of spin up and spin down neutrons, since the reflectivity depends quadratically on the potential (see page 24 and Figure 2.12). Below the superconducting phase transition temperature T_{sc}, the slope of the increasing intensity is reduced. One would expect a gradually reduced slope that is following the temperature dependence of the magnetisation of the LCMO

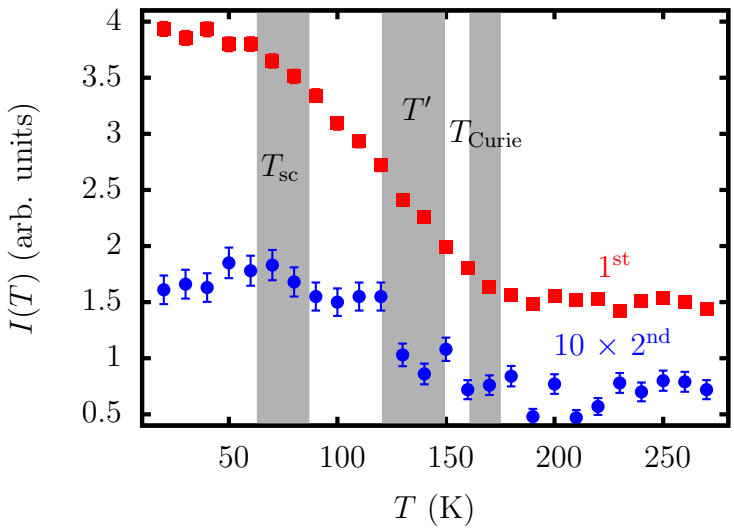

Figure 4.7: Temperature dependence of the integrated intensities measured with rocking scans at the positions of the 1st and the 2nd superlattice Bragg reflex. The 1st superlattice Bragg reflex increases below T_{Curie} = 165 K due to the magnetisation onset of the LCMO layers. Below T_{sc} = 75 K, its slope becomes changed. The 2nd superlattice reflex appears below T' ≈ 120 - 150 K. Its intensity has been scaled by a factor of 10. Sample: Y-LCM43.

layers here. Therefore, the observed kink in the slope at T_{sc} indicates an influence of the superconductivity on the magnetisation. This influence will be discussed in more detail in sections 4.3 and 4.4.

The intensity measured at the position of the 2nd superlattice Bragg reflex shows a different temperature dependent behaviour than the one at the position of the 1st superlattice Bragg reflex. It is not clear, whether it starts to increase right below T_{Curie} or at a little lower temperature. Below 120 K, it does not increase significantly anymore and remains about constant at T_{sc}. Combined with the measurements on the other two samples (Figure 4.8 and 4.9), one can nonetheless state that it most likely increases at $T' \approx 120$ - 150 K.

From these observations one can conclude that there is I) a transition at T_{Curie} where the LCMO layers become ferromagnetic, II) a transition to an unknown state at the interfaces occurring at $T' \approx 120$ - 150 K and III) a second transition of the entire LCMO layer magnetisation occurring at T_{sc}. The latter is most likely influenced by superconductivity. An influence by the structural phase transition of the substrate at $T^{II}_{STO} \approx 65$ K is rather unlikely, since the specular reflectivity of all surface facets was taken into account.

Figure 4.8 shows a temperature scan at the positions of the 1st and the 2nd superlattice Bragg reflex measured on sample Y-LCM75 which has a YBCO layer thickness of 14.1 nm and an LCMO layer thickness of 13.1 nm. The scan is similar to the one discussed above (shown in Figure 4.7). One difference between the two scans is that the present one was measured with polarised neutrons. A second difference is that the points in the present scan are the intensities measured at the centre position of the respective superlattice Bragg reflex and not the integrated intensities of rocking scans. Thus, the measured intensity is not the one reflected from the entire sample surface area. This makes the interpretation of

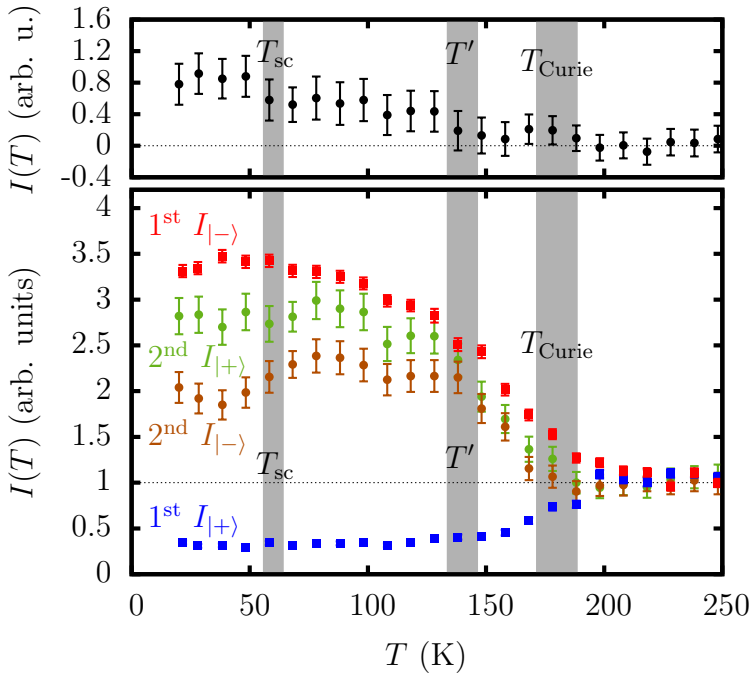

Figure 4.8: *Upper panel*: Temperature dependence of the splitting between the intensities measured for the spin up and spin down neutrons at the position of the 2nd superlattice Bragg reflex. *Lower panel*: Temperature dependent measurements of the intensities at the positions of the 1st and the 2nd superlattice Bragg reflex. The intensities of the 1st superlattice Bragg reflex split for the two neutron spin states below $T_{\mathrm{Curie}} = 180\,\mathrm{K}$. At the position of the 2nd superlattice Bragg reflex, the intensities of the two neutron spin states start to split at $T' \approx 140\,\mathrm{K}$. Sample: Y-LCM75.

the data around $T_{\mathrm{sc}} = 60\,\mathrm{K}$ difficult, since it is close to the structural phase transition of the substrate at $T_{\mathrm{STO}}^{\mathrm{II}} \approx 65\,\mathrm{K}$. Nonetheless, by comparing the evolution of the intensities at the positions of the two superlattice Bragg reflexes one can still extract trends from the data at $T < T_{\mathrm{STO}}^{\mathrm{II}}$.

Below $T_{\mathrm{Curie}} = 180\,\mathrm{K}$, the intensities of the spin up and spin down neutrons split up at the position of the 1st superlattice Bragg reflex. The temperature dependence of the splitting follows the shape of the magnetisation curve of the LCMO layers. Below T_{sc}, neither a kink in the slope of the splitting nor a kink in the slope of the intensities is observed as was the case in the previously discussed scan. The reason for this may be the missing integration of the intensities of rocking scans. Even without integration, the absence of a kink in the curve measured at the position of the 1st superlattice Bragg reflex can be compared to the behaviour of the intensities measured at the position of the 2nd superlattice Bragg reflex: There, the intensities of both neutron spin states increase below T_{Curie} the by same amount and thus follow the increasing splitting of the intensities of the two neutron spin states measured at the 1st superlattice Bragg reflex. Below $T' \approx 140\,\mathrm{K}$, their intensities start to split. The splitting increases with decreasing temperature. Below T_{sc}, the splitting seems to increase in a small step and to remain constant at lower temperatures. The sum of the intensities of both neutron spin states starts to decrease below T_{sc}. When comparing this behaviour with the smooth temperature dependence of the intensities measured at 1st superlattice Bragg reflex, one can state that the magnetic

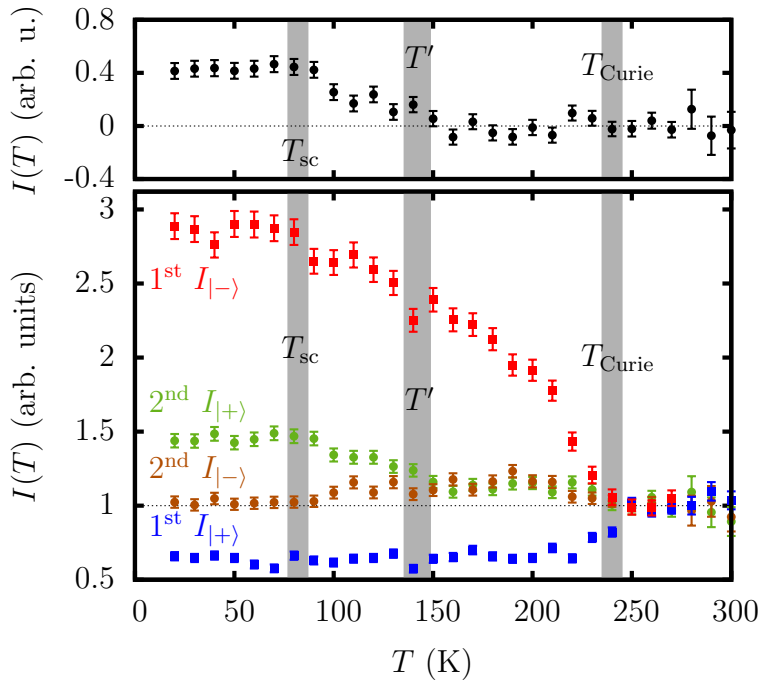

Figure 4.9: *Upper panel*: Temperature dependence of the splitting between the intensities measured for the spin up and spin down neutrons at the position of the 2nd superlattice Bragg reflex. *Lower panel*: Temperature dependence of the intensities measured at the positions of the 1st and the 2nd superlattice Bragg reflex. At the 1st superlattice Bragg reflex, the intensities of the two neutron spin states split below $T_{\mathrm{Curie}} = 240\,\mathrm{K}$. At the 2nd superlattice Bragg reflex, the intensities split at $T' \approx 145\,\mathrm{K}$. This splitting increases until $T_{\mathrm{sc}} = 80\,\mathrm{K}$. Sample: Y-LCM70.

induction depth profile changes at T_{sc}. In contrast to the scan presented in Figure 4.7, it is not possible to attribute the change in the magnetic depth profile to the interface regions or to entire layers here.

The scan on sample Y-LCM75 reveals almost the same information as the one on sample Y-LCM43. In particular, the same characteristic temperatures were identified. Nonetheless, the two scans differ in the following two points: I) In sample Y-LCM75, the change in the magnetic induction profile which occurs at T_{sc} cannot be attributed to the entire layers or to the interface regions. In sample Y-LCM43, it can be attributed to the entire layers. II) In the scan on sample Y-LCM75, the intensities measured at the position of the 2nd superlattice Bragg reflex clearly start to increase right below T_{Curie}. This is not the case in the scan on sample Y-LCM43. There, it is not clear, whether the intensity starts to increase right below T_{Curie} or at a somewhat reduced temperature.

Figure 4.9 shows a temperature scan at the positions of the 1st and the 2nd superlattice Bragg reflexes measured on sample Y-LCM70 which has 25.6 nm thick layers. It is the same type of scan as the one performed on sample Y-LCM75 (displayed in Figure 4.8). The intensities of the two neutron spin states measured at the position of the 1st superlattice Bragg reflex split up at $T_{\mathrm{Curie}} = 240\,\mathrm{K}$. The splitting increases with decreasing temperature and follows the magnetisation curve of the LCMO layers. At $T_{\mathrm{sc}} = 80\,\mathrm{K}$, there is no clear kink in the splitting observed. The intensities of the spin up and spin down neutrons measured at the 2nd superlattice Bragg reflex slightly increase below T_{Curie} over a temperature range of about 20 - 30 K. Below that, they remain constant until they

split up at $T' \approx 145\,\mathrm{K}$. The splitting increases at $T_{sc} < T < T'$ and remains constant below T_{sc}.

At T_{sc}, this scan reveals a change in the magnetic depth profile which is similar to the one observed on the other two samples. As in the scan on the sample Y-LCM75, it is not possible to conclude, whether this change is confined to the interfaces or whether it involves the magnetisation of the entire LCMO layers.

Compared to the two scans presented previously, the increase of the intensities which was measured at the position of the 2nd superlattice Bragg reflex below T_{Curie} is only small. This has most likely a geometrical reason: Since the temperature is close to T_{Curie}, there are likely areas in the LCMO layers in interface vicinity which do not carry the full magnetic moment or which are even non-magnetic. The interface regions with these areas cause a deviation of the magnetic induction depth profile from the structural one. Most likely, this deviation reaches by the same amount into the LCMO layers in all three samples. Since the ratio of this length scale to the layer thickness is the smallest for the sample with the thickest layers and since this ratio is inverse proportional to the intensity at the position of the 2nd superlattice Bragg reflex, the intensity increase is the smallest for the sample with the thickest layers.

From the temperature scans presented here one can conclude that the magnetic induction profile changes not only at the ferromagnetic transition temperature T_{Curie} but also at an intermediate temperature $T' \approx 120$ - $150\,\mathrm{K}$ and at the superconducting phase transition temperature T_{sc}. The change at T' must occur at the interfaces, since it was observed at the position of the 2nd superlattice Bragg reflex for all three samples. It is of magnetic origin and is discussed in more detail in the following subsection. The change in the profile of the magnetic induction at T_{sc} seems to be a change in the magnetisation of the entire LCMO layers. Nevertheless, this attribution to the entire layers (and not to the interfaces) is not unambiguous, since there are difficulties with the intensity changes caused by a structural phase transition of the substrate at $T_{STO}^{II} \approx 65\,\mathrm{K}$. In sections 4.3 and 4.4, these changes at T_{sc} are investigated in more detail.

4.2.2 Theoretical Modelling

In the previous subsection, neutron reflectometry measurements on superlattices with almost equally thick YBCO and LCMO layers have been discussed. It has been shown, that the 2nd superlattice Bragg reflex changes its shape below T'. Its intensity increase suggests that the potential depth profile deviates from a profile governed by the equal thickness of the YBCO and LCMO layers. In general, such a deviation observed in neutron reflectometry experiments can have a structural or a magnetic origin. However, a structural change can be excluded here, since the YBCO and LCMO layer thickness ratio would have to change from 1:1 at higher temperatures to at least 10:11 at lower temperatures in order to produce the measured intensity increase at the position of the 2nd superlattice Bragg reflex. Since the YBCO / LCMO double layer periodicity remains the same (the position of the 1st superlattice Bragg reflex does not change), such a large structural change could only be explained by a thermal expansion of 5% with opposite signs for the two materials. A thermal expansion of this magnitude is extremely unlikely

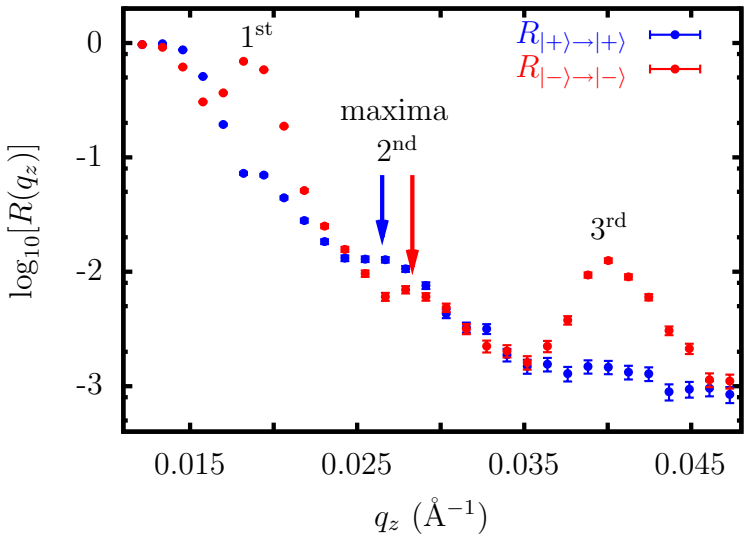

Figure 4.10: Polarised neutron reflectometry measurement performed at 5 K after cooling the sample in $H_{\mathrm{appl}} = 100$ Oe. The 2nd superlattice Bragg reflex is structurally suppressed because the sample has equally thick YBCO and LCMO layers. The reflex' position in q_z is different for the two neutron spin states. This allows for two possible scenarios of the magnetic induction profile. Sample: Y-LCM70.

and has not been observed in temperature dependent x-ray reflectometry measurements. The observed deviation from the 1:1 ratio must therefore have been induced by the magnetic induction. This is further supported by polarised neutron reflectometry measurements, where the maximum position in q_z of the 2nd superlattice Bragg reflex is different for the two neutron spin states (see Figure 4.10).

Theoretical model calculations are needed for a quantitative understanding and further reaching qualitative evaluation of reflectivity data obtained from thin film heterostructures. The formalism used for such calculations is based on the assumption that the layers are homogenous, that the interfaces are mainly flat and that the lateral correlation length of the interface roughness is smaller than the lateral coherence volume of the probe beam. Under the additional assumption of an elastic scattering at the sample and of a momentum that is conserved in the sample plane, the formalism reduces to the reflectivity calculated from a one dimensional potential depth profile of the heterostructure. The mathematical background of this formalism is explained in detail in subsection 2.2.1.

In the case of neutron reflectometry, the potential profile used in the formalism is the sum of the nuclear scattering length density profile and the magnetic induction profile. For the modelling of reflectivity curves measured on the same sample at different temperatures, the structural properties can be kept fixed, while the magnetic induction profile is varied. Figure 4.11 shows the calculated reflectivity curves of four different magnetic profiles, where the structural profile of the sample Y-LCM70 was used. In the first model, the magnetisation was constant throughout the LCMO layers and exhibited a step like decrease right at the interfaces to the YBCO layers. In the second model, the magnetisation penetrated some 1.5 nm into the YBCO layers. In both cases, the positions in q_z of the 2nd superlattice Bragg reflexes are the same. Note, that in the first model, the reflex for the spin up neutrons is hardly visible. Its tiny intensity results from the minimal contrast between the total scattering length densities of the layers for the spin up neutrons.

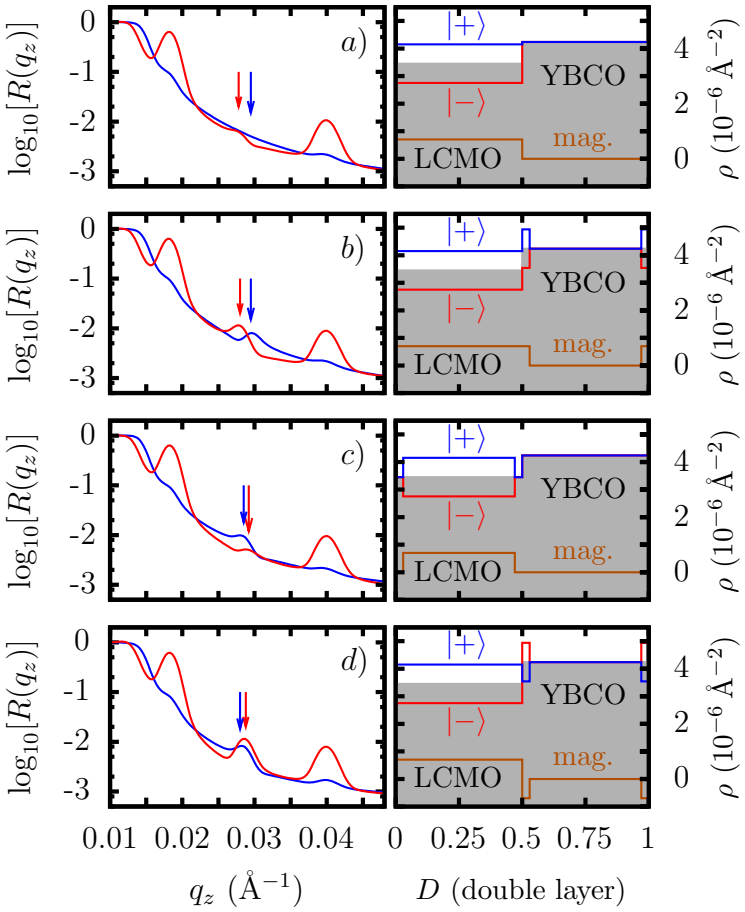

Figure 4.11: *Right*: The nuclear scattering length density profile (*grey*) with the magnetic profile (*orange*) and their superposition seen by the spin up neutrons ($|+\rangle$, *blue*) and the spin down neutrons ($|-\rangle$, *red*) are indicated for one double layer. *Left*: Calculated reflectivity curves for the spin up neutrons ($|+\rangle$, *blue*) and the spin down neutrons ($|-\rangle$, *red*). *a*) The magnetic induction is homogeneous in the entire LCMO layers. *b*) The magnetic induction penetrates the YBCO layers. *c*) A non-magnetic layer in interface vicinity in the LCMO layers. *d*) A layer in interface vicinity in the YBCO layers with a magnetic moment aligned antiparallel to the one in LCMO.

In both models the relative positions of the 2nd superlattice Bragg reflex for the spin up and spin down neutrons are reversed compared to the measured reflectivity curves (Figure 4.10). The correct relative positions can be achieved by either assuming a non-magnetic layer within the LCMO layers at the interfaces (third model in Figure 4.11) or by assuming a layer in interface vicinity in YBCO with a magnetic moment that is aligned antiparallel to the LCMO moments (fourth model in Figure 4.11). Both models yield the same positions of the 2nd superlattice Bragg reflex. Changes in the thickness of the non-magnetic layer or of the layer with the antiparallel oriented magnetic moment only change the relative intensities of the reflexes for the two neutron spin states. Further elaboration of the models in the sense of a smoothening of the magnetisation profile (dividing the profile in many more potential steps with less changes from one step to the other) do also change the relative intensities of the reflexes only.

From these models one can conclude that there are two possible kinds of deviations of the magnetic induction profile from the structural one. Either, there is a non-magnetic layer or a layer with a reduced magnetic induction on the LCMO side of the interfaces, or there is a layer on the YBCO side of the interfaces which carries a magnetic moment that is antiparallel aligned to the one in LCMO. A comparison of the reflectivity curves which have been calculated based on these two models reveals that the deviation of the magnetic induction profile from the interface has about the same length scale and about

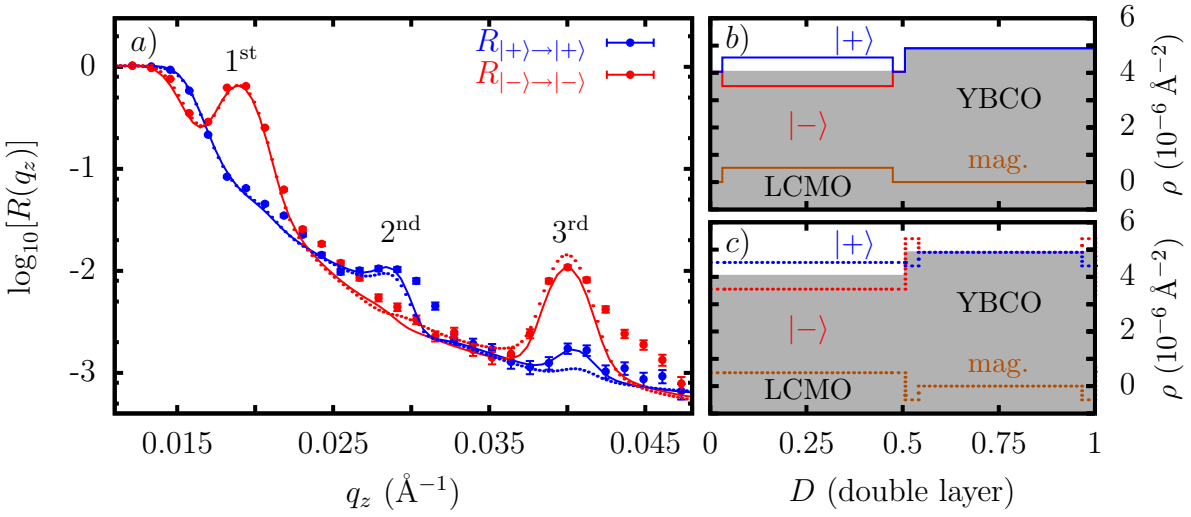

Figure 4.12: *a*) Polarised neutron reflectometry measurement at 130 K in $H_{\mathrm{appl}} = 100$ Oe compared with reflectivity curves that have been calculated based on two different models (*solid lines*: Model shown in *b*, *dotted lines*: Model shown in *c*). Both models reproduce reasonably well the data at $q_z < 0.04$ Å^{-1}. The differences between the models and the misfit to the data at $q_z > 0.04$ Å^{-1} is discussed in the text. *b*) Model of a scattering length density depth profile with a 1.6 nm thick non-magnetic layer in interface vicinity in LCMO. The magnetisation is 1.4 μ_{B} per Mn atom and the LCMO top layer has a magnetic moment which is reduced by 30%. *c*) Model of a scattering length density depth profile with a 1.7 nm thick layer in interface vicinity in YBCO that has a magnetic moment which is oriented antiparallel to the one in LCMO. The magnetisation is 1.3 μ_{B} per Mn atom in the LCMO layers, while the antiparallel moment is 1.1 μ_{B} per Cu atom. The LCMO top layer has a magnetic moment which is reduced by 30%. Sample: Y-LCM70.

the same strength in both cases. For a quantitative analysis, reflectivity curves were calculated for both models and compared with a measurement performed at 130 K (see Figure 4.12). This particular temperature was chosen because it is below T' and above the structural phase transitions of the STO substrate. It allows the extraction of the most reliable numbers, since it is a sufficiently low temperature where the constraints of the theoretical modelling are still valid (any surface waviness would decrease the reliability of the numbers). The first model (Figure 4.12 *b*) contains a non-magnetic layer in interface vicinity in LCMO with a thickness of 1.6 nm. In the centre of the LCMO layers the magnetic moment is 1.4 μ_{B} per Mn atom. Additionally, the top most LCMO layer has a magnetisation which is reduced by 30% compared to the rest of the LCMO layers. In interface vicinity in YBCO the second model (Figure 4.12 *c*) contains a layer with a thickness of 1.7 nm and a magnetic moment of 1.1 μ_{B} per Cu atom which is oriented antiparallel to the one in LMCO (1.3 μ_{B} per Mn atom). The magnetic moment of the top most LCMO layer is reduced by 30%. Both models give very similar reflectivity curves at q_z-values smaller than 0.04 Å^{-1}. At the position of the 3$^{\mathrm{rd}}$ superlattice Bragg reflex, the model with the antiparallel aligned magnetic YBCO layer shows a larger splitting of the intensities for the two neutron spin channels, which indicates more pronounced

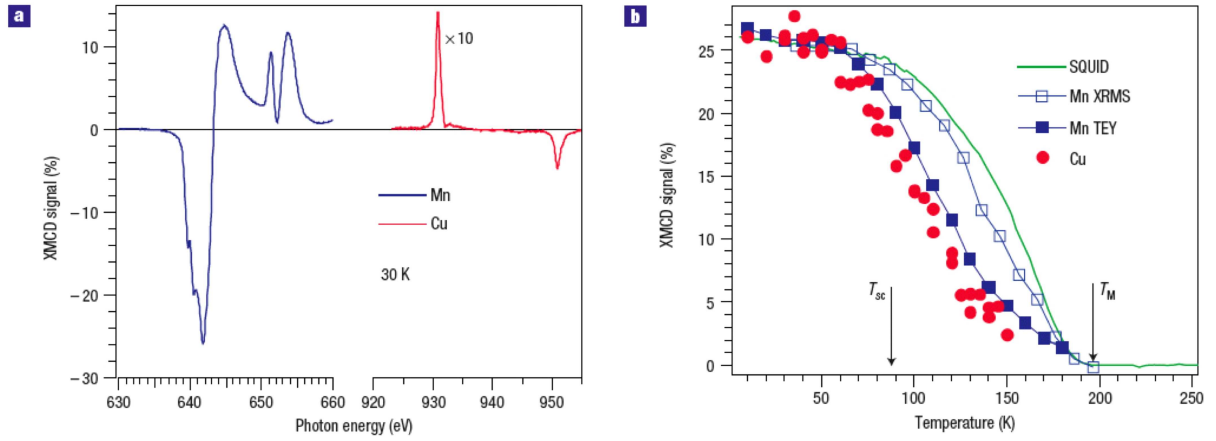

Figure 4.13: X-ray magnetic circular dichroism (XMCD) spectra and their evolution with temperature. *a*) XMCD signals obtained from the core-level absorption spectra for Cu and Mn. The Mn XMCD signal (*blue curve*) is large and reaches 23% at the L_3 edge. For comparison, the magnitude of the XMCD signal for Cu (*red curve*) is multiplied by a factor of 10. The XMCD signal for Cu has the opposite sign of the one for Mn *b*) Temperature dependence of the XMCD signals of Cu and Mn compared with the bulk magnetisation (*green line*). All curves are normalised to the value of dichroism on Mn. The interfacial magnetism of Mn decreases faster than the bulk magnetisation. The estimated errors are of the order of 20% at low temperatures and become larger as the temperature approaches T_M (in the present work called T_{Curie}). This figure has been taken from Ref. [93]

depth dependent changes in the magnetisation profile. At the position of the 2nd and 3rd superlattice Bragg reflex, the intensities of the simulated curves are too low towards larger q_z-values. This is partially caused by the resolution used in the experiment and partially by a thickness variation of the layers in the sample, which can occur due to imperfect sample growth conditions (see section 3.1). It can be taken into account in the theoretical modelling: One has to calculate several reflectivity curves based on the same magnetic model where the structural layer thickness is different each time. The obtained curves are then incoherently added up. This has not been done here because it does not lead to substantial changes of the numbers obtained.

Both models have their merits and their shortcomings. The first model with the non-magnetic or antiferromagnetic layer in interface vicinity is plausible in the sense that it can be explained by I) a changed oxygen stochiometry in the LCMO layers close to the interfaces compared to the layer centres, II) a charge transfer through the interfaces which is reducing the fraction of Mn^{3+}-ions in interface vicinity [94], or III) an extrinsic strain at the interfaces which is distorting the oxygen octahedrons in LCMO in interface vicinity. All three options could lead to a non-magnetic or antiferromagnetic phase as the ground state in interface vicinity. The shortcoming of this model is the possible disagreement with the experimentally observed weak antiparallel magnetic moment located on the Cu atoms which speaks for the second model: J. Chakhalian and co-workers have performed x-ray magnetic circular dichroism (XMCD) measurements on YBCO / LCMO superlat-

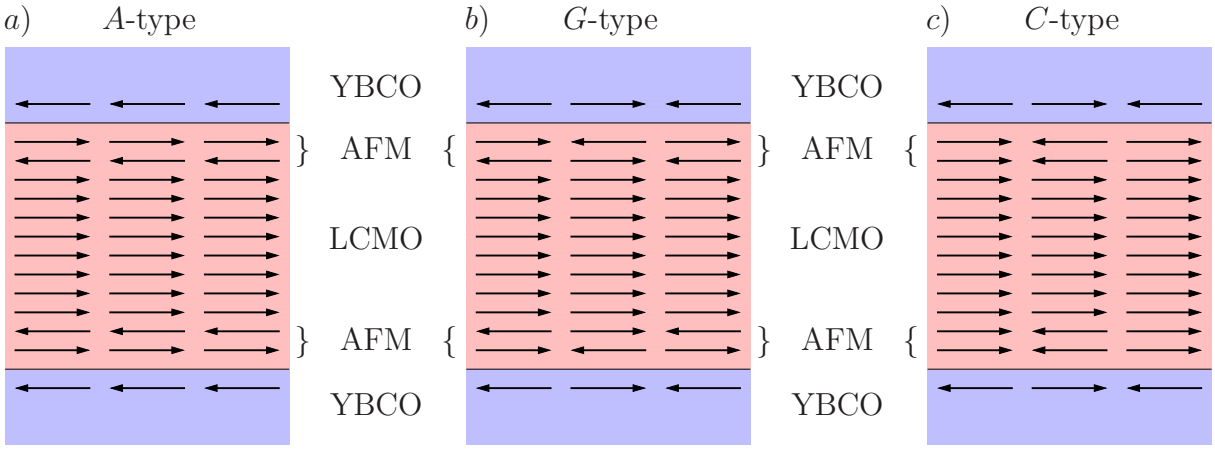

Figure 4.14: There are three possible types of antiferromagnetic (AFM) order on the LCMO side of the interfaces: *a*) *A*-type antiferromagnetic, *b*) *G*-type antiferromagnetic and *c*) *C*-type antiferromagnetic. The Cu-spins on the YBCO side of the interfaces couple antiparallel to the Mn-spins. Only an *A*-type antiferromagnetic order on the LCMO side of the interfaces would give rise to a ferromagnetic alignment of the Cu-spins.

tices [93]. They used samples with 10 nm thick layers which had been grown by the same person on the same pulsed laser deposition equipment as the samples used for the neutron experiments presented here. By probing the magnetism on the Mn L_3 and the Cu L_3 edge, they revealed a magnetic moment located on Cu which is oriented antiparallel to the moment located on Mn (Figure 4.13). They estimated this moment at 10 K to be maximally $0.2\,\mu_B$ per Cu atom at the interfaces when assuming an exponential decay into the YBCO layers. Above 150 K, the size of this moment decreased below the detection limit. This temperature is reasonably close to T', where the deviation of the magnetic depth profile evolves from the structural interfaces. On the first glimpse, the second model with the antiparallel magnetic moment on the YBCO side of the interfaces thus seems to be the correct one. Specially, since it can be explained either by a Cu-O-Mn super exchange through the interfaces which couples the Cu-spins and the Mn-spins antiparallel or by an inverse proximity effect [69] combined with a precursor superconducting state [16]. The only shortcoming of this model is the magnitude of the antiparallel moment which, according to the simulations, is $1.1\,\mu_B$ per Cu atom. This is much larger than the $0.2\,\mu_B$ per Cu atom observed in the XMCD experiments and also much larger than the $0.5\,\mu_B$ per Cu atom observed in antiferromagnetically ordered bulk $YBa_2Cu_3O_6$. Since the XMCD measurements did only show a spin component of the Cu moment, one can exclude an orbital contribution to the moment of the Cu atoms which might increase the moment to the $1.1\,\mu_B$ per Cu atom needed for the neutron reflectivity simulations.

Due to the shortcomings of both models, the most likely depth profile of the magnetic induction is a combination: A weak magnetic moment induced in interface vicinity in the YBCO layers is oriented antiparallel to the one in the LCMO layers, while the magnetic moment in the LCMO layers is reduced in interface vicinity. If the net magnetisation on the LCMO side of the interfaces is reduced to zero, the Mn-spins must be *A*-type

antiferromagnetically ordered, i. e. ferromagnetically along the interfaces and antiferromagnetically perpendicular to the interfaces (see Figure 4.14). Only then, the Cu moments have a Mn moment across the interface to which they can couple antiparallel to and which allows them at the same time to align ferromagnetically along the interfaces.

This combined model accounts for the reportedly small value of the antiparallel moment in the YBCO layers. Unfortunately, the precise shape of the profile is unknown and cannot be satisfactory determined by simulations of polarised neutron reflectometry measure- ments, since there would be too many free parameters. Nonetheless, it is still accessible that the deviation of the magnetic induction profile from the structural depth profile must be confined to a length scale of about 1 - 2 nm on both sides of the interfaces. The magnetisation on the LCMO side will be considerably reduced and the magnetic moment aligned antiparallel induced in YBCO will be less than $0.2\,\mu_B$ per Cu atom. The reduced moment on the LCMO side will not be zero unless the Mn spins order in interface vicinity *A*-type antiferromagnetically, since there is a weak moment at the interfaces required for the Cu moments to couple antiparallel to.

4.2.3 Results and Interpretation

It has been shown subsections 4.2.1 and 4.2.2 that there is a change in the magnetic induction depth profile occurring at the interfaces at $T' \approx 120$ - 150 K and that there is most likely a change occurring in the entire ferromagnetic layers at T_{sc}. The possible physical origins of the change at T' are discussed here, while the origins of the change at T_{sc} are discussed in the following two sections based on different experiments.

The comparison of theoretical calculations with polarised neutron reflectometry data obtained at 130 K revealed two possible profiles of the magnetic induction evolving below T'. The first one contains a 1 - 2 nm thick layer on the LCMO side of the interfaces which is seen by the neutrons as non-magnetic. This layer may have a strongly reduced net magnetic moment, may be effectively non-magnetic or may be antiferromagnetic. In the following, this model will be called the *magnetic dead layer model*. The second possible profile contains a 1 - 2 nm thick layer on the YBCO side of the interfaces which carries a net magnetic moment that is oriented antiparallel to the moment of the LCMO layers and the externally applied magnetic field. In the following this model will be denoted as the *antiphase proximity effect model*. In agreement with the latter model, a magnetic moment on the Cu atoms that is aligned antiparallel to the one of the Mn atoms has been observed by J. Chakhalian and co-workers in x-ray magnetic circular dichroism (XMCD) measurements on YBCO / LCMO superlattices [93]. At 10 K they estimated the amplitude of the Cu spin moments at the interfaces to be less than $0.2\,\mu_B$ per Cu atom, which is considerably smaller than the $1.1\,\mu_B$ per Cu atom extracted from neutron reflectivity simulations for the antiphase proximity effect model. This suggests that the most likely depth profile of the magnetic induction is a combination of the antiphase proximity effect model and the magnetic dead layer model. This way, the reportedly small value of the Cu moments can be accounted for. As a consequence, a completely non-magnetic layer on the LCMO side of the interfaces is very unlikely because there is a Mn moment required at the interfaces for the Cu moments to couple antiparallel to. Therefore, the magnetic

dead layer is most likely not fully non-magnetic, C-type or G-type antiferromagnetic but contains a strongly reduced ferromagnetic moment or is A-type antiferromagnetic.

In the following, the physical origins of the depth profiles of the magnetic induction corresponding to the antiphase proximity effect model and the magnetic dead layer model are discussed. The first two points describe possible scenarios for the occurrence of the antiphase proximity effect, while the other four points describe possible reasons for the occurrence of a layer with a strongly reduced magnetic moment on the LCMO side of the interfaces:

a) In Mn^{4+}, both e_g-orbitals are expected to be empty, while in Mn^{3+} at least one e_g-orbital is occupied (preferentially the $d_{x^2-y^2}$-orbital) [93]. Subsequently, d_{z^2}-electrons hopping virtually from Cu^{2+} to the mainly empty Mn d_{z^2}-orbitals dominate the Cu-O-Mn super exchange through the interface. This would correspond to an antiferromagnetic coupling of the magnetic moments of the Mn and Cu atoms [93, 95]. The strength of this coupling could explain the onset temperature T'.

b) F.S. Bergeret, A.F. Volkov and K.B. Efetov showed in theoretical calculations that a triplet component can be induced in the superconducting order parameter if the superconductor is in adjacency to a ferromagnet [69, 70]. They calculated the influence of the conduction electrons on the magnetisation of the ferromagnet and on the magnetisation induced in the superconductor. They found that the magnetisation inside the ferromagnet is reduced towards the interface and that a magnetic moment is induced in the superconductor that is aligned antiparallel to the moment of the ferromagnet. This antiparallel moment decays into the superconductor on a length scale of ξ_{sc} (see Figure 2.7).

While this model may well account for the experimental data below the superconducting phase transition temperature T_{sc}, it remains to be explained why the antiparallel moment localised on Cu has been observed below 150 K already [93]. One possible explanation for such a high onset temperature might be a precursor superconducting state with a missing long range coherence which may occur in bulk YBCO at $T^* \approx 120$ - 150 K [16].

c) This point is closely related with the explanation *b* for the antiphase proximity effect: F.S. Bergeret, A.F. Volkov and K.B. Efetov have calculated that besides the antiparallel aligned moment in YBCO the magnetic moment in the ferromagnet would be reduced towards the interface [69, 70].

d) An extrinsic strain at the interfaces may distort the oxygen octahedrons in a way in LCMO in interface vicinity that a non-magnetic or antiferromagnetic phase becomes the electronic ground state of the system. Such a strain induced order could set in at T'.

e) The strain conditions caused by the lattice mismatch of YBCO and LCMO at the interfaces may also give rise to a change in the oxygen stochiometry of LCMO near the interfaces. This may lead to a non-magnetic or antiferromagnetic ordering close

to the interfaces in the LCMO layers. The onset temperature of this ordering could be T'.

f) W. Luo *et al.* have shown with density-functional theory (DFT) calculations for YBCO / LCMO superlattices that at the interfaces the occupancy of the Mn e_g-levels is reduced [94]. A charge transfer through the interfaces could be the reason for a reduced fraction of Mn^{3+}-ions in interface vicinity. Subsequently, a super exchange stabilised antiferromagnetic order would be favoured in the two Mn layers lying closest to the interfaces. The onset temperature for this ordering could be T'.

Since an antiparallel magnetic moment on the Cu atoms was observed experimentally in XMCD measurements, at least one of the two scenarios *a* and *b* is realised. Scenario *b* is more likely in the sense that the length scale of the induced moment is with the observed 1 - 2 nm in the range of $\xi_{sc} \approx 1$ nm, while the length scale in scenario *a* would be in the range of one reduced unit cell, i. e. of 0.4 nm. On the other hand, the observation of the moment well above the macroscopic T_{sc} is rather puzzling. A precursor superconducting state which forms below T' is a possible explanation, but its existence remains to be established exprimentally. A proper distinction between the two scenarios may be achieved by investigating corresponding superlattices, where the YBCO layers are either underdoped or overdoped. In the case of scenario *b*, a characteristic varition of T' should be observed. In the overdoped samples, T' should essentially coincide with the macroscopic T_{sc}.

Out of the four scenarios for the magnetic dead layer model, scenarios *e* and *f* are the most likely ones. A modified oxygen stochiometry at the interfaces of the LCMO layers could compared to the centre of the LCMO layers change the transition temperature and change the magnetic ground state. Likewise, a charge transfer could induce a change of the magnetic ground state at the interfaces. Scenario *d* is very unlikely: The observed effect is confined to the interfaces. Accordingly, the stress would have to be induced by the adjacency to the YBCO layers, since a stress induced by the substrate would lead to a relaxation that extends over several layers and thus involves not only the interface regions but the bulk of the individual layers. Scenario *c* would be the most exciting one, since it explains at the same time the antiphase proximity effect model. But it is questionable whether it can explain the amount of reduction of the magnetic moment inside the ferromagnet (see Figure 2.7). Therefore, most likely one of the scenarios *d*, *e* and *f* will be additionally true if scenario *b*/*c* is true.

Since there is very likely an additional reduction of the magnetic moment on the LCMO side of the interfaces, one can further speculate about its nature. One possibility is that the interface regions are laterally inhomogeneous and exhibit areas with a ferromagnetic ground state and areas with a non-magnetic or antiferromagnetic ground state. Another possibility is that the interface regions exhibit a laterally homogeneous *A*-type antiferromagnetic ground state, i. e. that the Mn-spins couple ferromagnetically in the sample plane and antiferromagnetically from one Mn layer to the next one (see Figure 4.14 *a*). This order would have no net magnetic moment and a ferromagnetic layer right at the interfaces to which the Cu-spins could couple to. Subsequently, this order would most likely give rise to an exchange bias. This stands even though in contrast to the observations made on the

samples used here: Only few samples showed an exchange bias at very low temperatures (see Figure 3.2), while all of them showed the deviation of the magnetic induction depth profile from the structural depth profile discussed here.

The question remains, why the observed effect occurs at a temperature T' which is well separated from T_{Curie} and T_{sc}. The answer could be a magnetic state at the interfaces in the LCMO layers which has an ordering temperature T' that is lower than T_{Curie} of the LCMO layer centre. On the other hand, it could also be a structural deviation of the interface region in LCMO. If this deviation is highly stress sensitive, the structural phase transition of the substrate surface at $T^{\mathrm{I}'}_{\mathrm{STO}} \approx 150\,\mathrm{K}$ could in this regions trigger a transition of the magnetic order. In order to distinguish between these two effects, one should perform the same experiments as presented here on superlattices grown on different substrates like for example $NdGaO_3$ with (110)-orientation or $LaAlO_3$ with (001)-orientation.

4.3 Modulation in the Magnetic Induction Profile in Underdoped Samples

A modulation in the magnetic induction depth profile observed in superlattices with underdoped $Y_{0.6}Pr_{0.4}Ba_2Cu_3O_7$ (YPr0.4BCO) is discussed here. In the first part, the modulation's basic features and its temperature dependence are presented. In the second part, the theoretical modelling of the modulation is introduced. The dependence of the modulation on the sample orientation and on a uniaxial stress applied laterally on the substrate are discussed in the third and fourth part, respectively. The modulation's dependence on the strength of the externally applied magnetic field is presented the fifth part. The results are summarised and interpreted in the last part. Some of these data have been published in Ref. [96].

4.3.1 General Features and Temperature Dependence

Neutron reflectometry measurements at low temperatures on superlattices comprising $Y_{0.6}Pr_{0.4}Ba_2Cu_3O_7$ (YPr0.4BCO) and $La_{2/3}Ca_{1/3}MnO_3$ (LCMO) layers showed a fractional order superlattice Bragg reflex. Additional temperature dependent measurements revealed that this reflex develops right below $T_{\mathrm{sc}} = 40\,\mathrm{K}$ (Figure 4.15 and 4.16), which points to a superconductivity-induced origin. As the reflex' position is at a smaller q_z-value than the position of the 1st superlattice Bragg reflex, it must be caused by a modulation in the potential depth profile. This modulation must be perpendicular to the layers and have a periodicity that exceeds the thickness of one YPr0.4BCO / LCMO double layer. Figure 4.16 shows detailed neutron reflectometry temperature scans that were performed with polarised neutrons at the positions of the fractional and of the 1st superlattice Bragg reflex. The intensities have been normalised to the ones measured at the edge of total reflection. This way, the intensity variations originating from the changing tilting angle of the substrate surface facets (see section 4.1) are eliminated. It can be seen that the intensities measured at the position of the 1st superlattice Bragg reflex remain for both

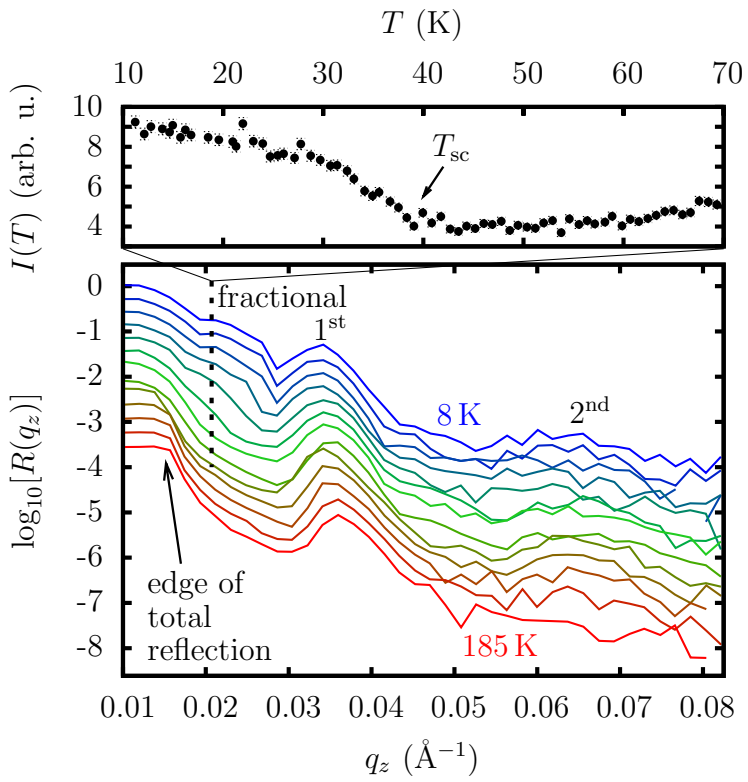

Figure 4.15: *Upper panel*: Temperature dependence of the intensity of the fractional superlattice Bragg reflex measured with unpolarised neutrons at the position $q_z = 0.0207\,\text{Å}^{-1}$ on a superlattice with underdoped YPr0.4BCO. The applied magnetic field was $H_{\text{appl}} = 100\,\text{Oe}$. *Lower panel*: Reflectivity curves measured with unpolarised neutrons at various temperatures from 8 K to 185 K. Below 185 K, the 2nd superlattice Bragg reflex appears. The fractional superlattice Bragg reflex appears below $T_{\text{sc}} = 40\,\text{K}$. The curves are shifted in height for comprehensibility reasons. Sample: YPr04-LCM1

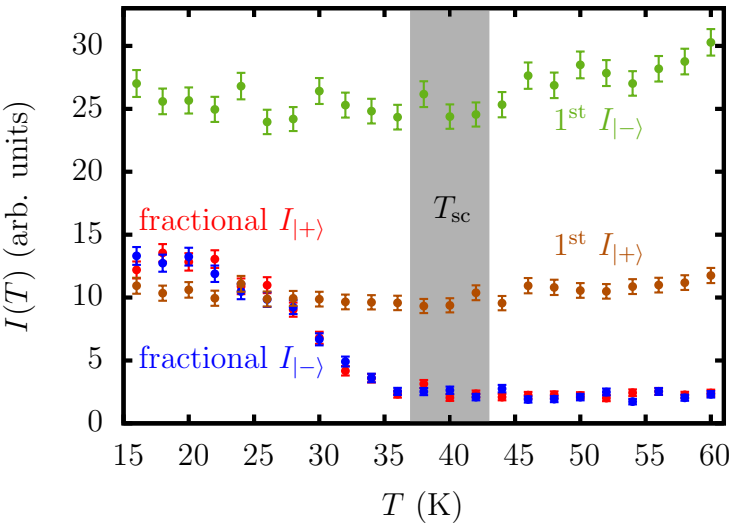

Figure 4.16: Temperature dependent neutron reflectometry measurements of the intensities at the positions of the fractional and the 1st superlattice Bragg reflex in $H_{\text{appl}} = 100\,\text{Oe}$. The intensities of the 1st superlattice Bragg reflex remain constant at $T_{\text{sc}} = 40\,\text{K}$ while the ones at the position of the fractional superlattice Bragg reflex increase. Sample: YPr04-LCM1

neutron spin states almost constant in the investigated temperature range. Due to geometrical reasons, they contain information about the changes in the depth profile that have a double layer periodicity. Their constancy can therefore be interpreted as a conservation of the double layer periodicity from above T_{sc}. The intensities measured at the position of the fractional superlattice Bragg reflex increase below T_{sc} for both neutron

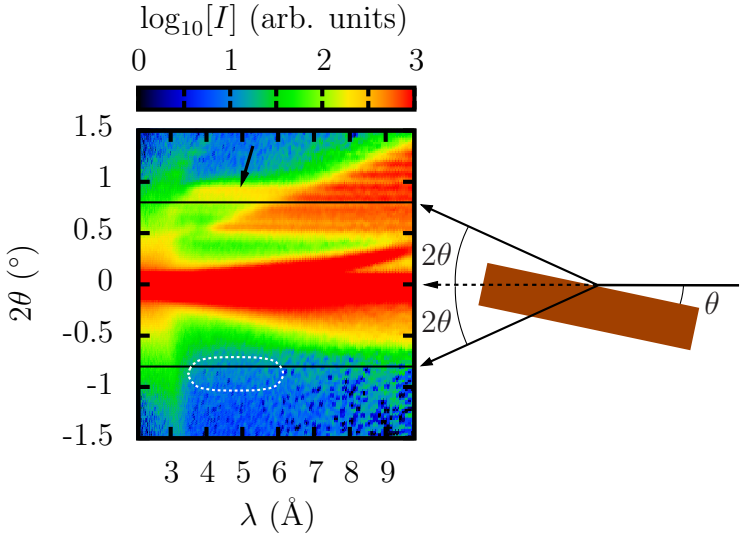

Figure 4.17: Neutron reflectometry measurement in time of flight mode at an incident angle of $\theta = 0.4°$. The fractional superlattice Bragg reflex is visible in reflection at the scattering angle of $2\theta = 0.8°$ (*black arrow*) but not in transmission at $2\theta = -0.8°$ (*white dashed area*). Small angle scattering can thus be excluded as the origin of the fractional superlattice Bragg reflex. Further explanations for the measured intensity at $2\theta > 0.4°$ are given in Figure 4.28. Sample: YPr04-LCM6a

spin states simultaneously. This implies that there is a change in the depth profile which has a periodicity of more than one double layer. Thus, a modulation evolves superposed to the potential profile existing above T_{sc}.

The origin of this modulation must be magnetic, since any modulation of the nuclear scattering length density profile and any other signal can be excluded: A material transport from one layer to the second next one would have to be in the order of about 10% of the layer's density to result in a corresponding modulation of the nuclear scattering length density profile. This is very unrealistic. Small angle scattering that gives rise to an additional intensity at the respective position in q_z can be excluded firstly by the absence of any structural transition at T_{sc} (see section 4.1) and secondly by experiments with an area detector on a time of flight neutron reflectometer. In the latter experiments, small angle scattering would be seen as a signal in reflection of the sample surface and in transmission through the substrate. These signals would be located at the scattering angle 2θ and have about the same intensity. Figure 4.17 illustrates, that there is only a signal observed in reflection but not in transmission.

The observation that the intensities of the two neutron spin states are the same at the position of the fractional superlattice Bragg reflex seems to contradict the magnetic origin of the modulation. This apparent contradiction can be answered with the following picture: There are different areas in the sample plane which are larger than the lateral coherence length of the neutrons. The modulation has in each such area a different, random phase. The incoherent superposition of the signals from the neutrons being reflected from all over the sample surface contains therefore contributions of the modulation with all possible phases. Thus, the intensities of both neutron spin states contain the same information.

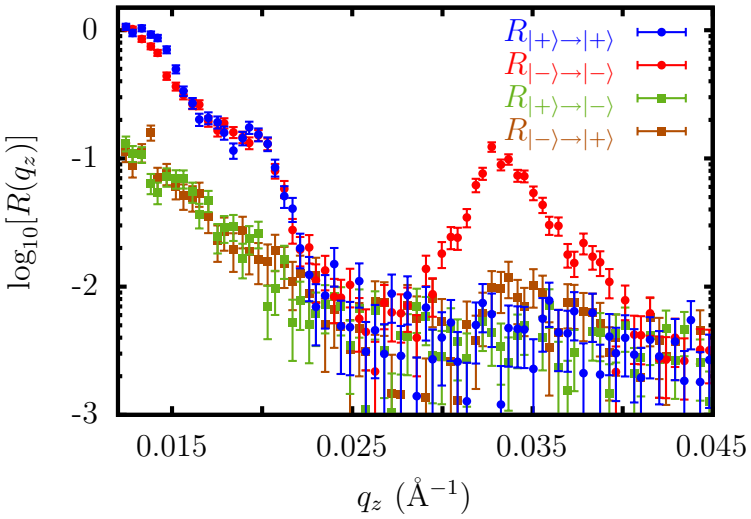

Figure 4.18: Polarised neutron reflectometry measurements with spin analysis performed at 15 K and $H_{\mathrm{appl}} = 100$ Oe. The fractional superlattice Bragg reflex is visible in the non-spin flip channels but not in the spin flip channels. Therefore, the magnetic moments must be either aligned parallel or antiparallel to the applied magnetic field. The modulation cannot be caused by canted or from layer to layer rotating moments. Sample: YPr04-LCM1

So far, the nature of the observed modulation has not been discussed in detail. According to the measurements presented above, there are three different origins of the modulation possible. I) It may be a rotation of the magnetic moments from one LCMO layer to the next one. This rotation may be either in the sample plane or out of the sample plane. II) It may be a modulation of the magnitude of the magnetic moment from on LCMO layer to the next one. III) It may be a more complicated state where ferromagnetic and non-magnetic or antiferromagnetic domains in the LCMO layers change at T_{sc} from one magnetic state to the other. In order to distinguish between these options, polarised neutron reflectometry measurements were performed with spin analysis. With this technique, components of the magnetic induction which point in the sample plane perpendicular to the applied magnetic field can be observed. These moments lead to a flipping of the neutron spins. Hence a spin flip signal is observed if I) the modulation consists of magnetic moments that are canted in the sample plane in opposite direction from one LCMO layer to the next one or if II) the modulation consists of moments rotating in the sample plane by a certain amount from one LCMO layer to the next one (spiral magnetisation). Since the canting or rotation would have to have the same periodicity as the modulation, the signal would have to be at the same q_z-value as the fractional superlattice Bragg reflex. Figure 4.18 shows these measurements and illustrates, that no spin flip signal was observed at this position. Therefore, a canting or rotation of the magnetic moments in the sample plane can be excluded as the origin of the modulation. A canting out of the sample plane is also very unlikely as the origin. Even though magnetic moments pointing out of the sample plane are not observable in neutron reflectometry, this possibility is very unlikely, since magnetometry measurements revealed a saturation moment of 2.4 μ_{B} per Mn atom which is very close to the 2.1 μ_{B} per Mn atom obtained from neutron reflectometry measurements at $H_{\mathrm{appl}} = 100$ Oe (see subsection 4.3.2).

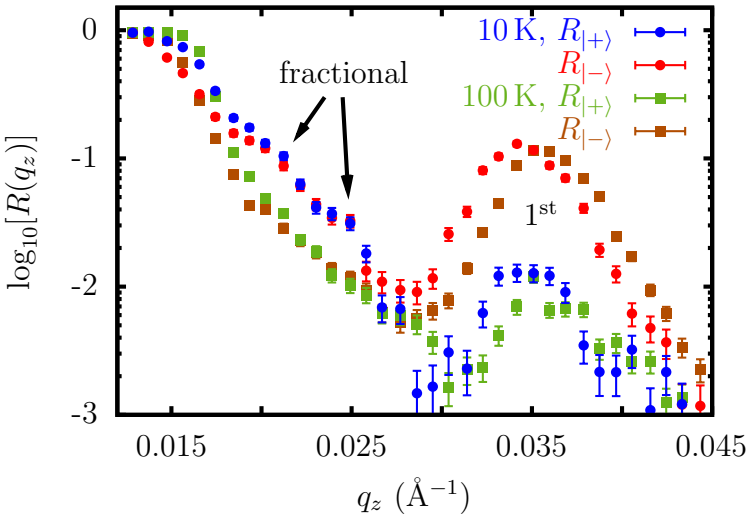

Figure 4.19: Polarised neutron reflectometry measurements at 10 K and 100 K in $H_{\text{appl}} = 100$ Oe. The fractional superlattice Bragg reflex observed at 10 K is not at the position of the 0.5$^{\text{th}}$ reflex but at the positions of the 1/3$^{\text{rd}}$ and 2/3$^{\text{rd}}$ superlattice Bragg reflex. Therefore, the periodicity of the modulation must be three double layers. At 100 K, the modulation is absent. Sample: YPr04-LCM1

During this work, the modulation was investigated in experiments on different instruments. Depending on the instrument and on the mounting of the sample, the shape and the position in q_z of the fractional superlattice Bragg reflex varied (see Figure 4.15, 4.19, 4.23 *a* and 4.26). This is the reason, why the reflex is referred to as *fractional superlattice Bragg reflex*, even though it's periodicity turned out to be most often about two double layers, leading to a 0.5$^{\text{th}}$ superlattice Bragg reflex. The mounting dependence mentioned here was investigated separately and is discussed in more detail in the subsections 4.3.3 and 4.3.4.

4.3.2 Theoretical Modelling

The starting point for the theoretical modelling of the modulation was the determination of the sample's structural parameters like the layer thickness, the scattering length densities and the interface and surface roughnesses. In a second step, the magnetic induction profile at $T > T_{\text{sc}}$ has been appended to the structural parameters in the model. In a third step, the modulation evolving below T_{sc} has been added. The entire model has been kept as simple as possible in order to understand the basic aspects of the modulation. It consisted of only one slice per physical layer which has a constant scattering length density and a constant magnetic moment. The deviation of the magnetic induction profile from the structural interfaces which is discussed in subsection 4.2.2 has been neglected, even though the 2$^{\text{nd}}$ superlattice Bragg reflex appears also in the samples with underdoped YPr0.4BCO (see Figure 4.15).

Determination of the Structural Parameters at $T > T_{\text{Curie}}$: The structural parameters of the model have been determined by the comparison of a calculated neutron reflectivity curve with a measurement on the sample in the non-magnetic state at 185 K $> T_{\text{Curie}}$. The curve has been matched with the data by varying the parameters (grey line and grey data points in Figure 4.20). The layer thickness

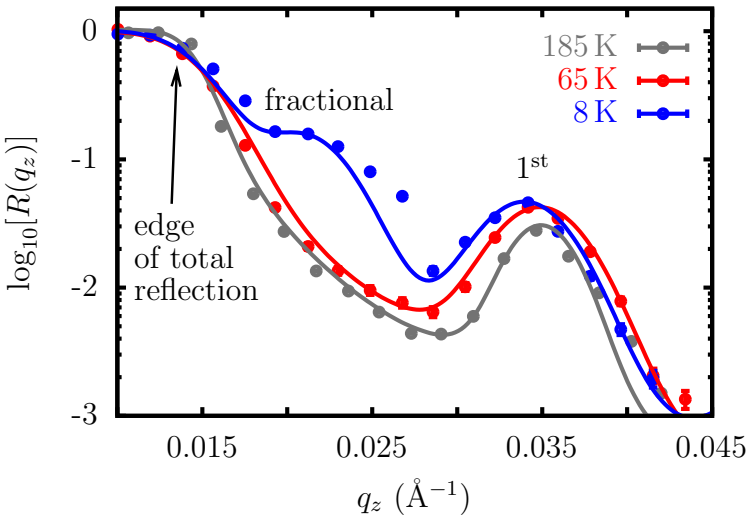

Figure 4.20: Calculated reflectivity curves (*lines*) from the models of the non-magnetic (185 K) and the magnetic state with and without modulation (8 K and 65 K, respectively). The lower intensity in the calculated curve at the tail towards higher q_z-values of the fractional superlattice Bragg reflex is caused by the resolution used for the simulations and by the strongly simplified model. The measured data (*points*) are identical to the ones presented in Figure 4.15. Sample: YPr04-LCM1

is for both LCMO and YPr0.4BCO layers 98 Å and the scattering length densities are $3.578 \cdot 10^{-6}$Å^{-2} and $4.598 \cdot 10^{-6}$Å^{-2}, respectively. The values of both scattering length densities correspond to the theoretical values. Therefore, the densities of the layers are the same as the ones of the bulk materials. Only the top LCMO layer has a scattering length density which is reduced by 15%. This reduction can be caused by a relaxation at the surface, a reduced oxygen content or a hydrogen accumulation in the top layer. The former would induce a reduction of the material density, while the latter two would reduce mainly the scattering length density and keep the material density about the same. The statistical roughness of the interfaces and the surface have been determined as 10 Å and 20 Å, respectively.

Magnetic Induction Depth Profile at $T_{\mathrm{Curie}} > T > T_{\mathrm{sc}}$: In a second step, the magnetic induction depth profile occurring at $T_{\mathrm{Curie}} > T > T_{\mathrm{sc}}$ has been appended to the model. Every LCMO layer has been assumed to be ferromagnetic and to have the same magnetic moment. Only the moment of the top layer has been reduced by 15% as a consequence of its likewise reduced nuclear scattering length density. A schematic sketch of the profile is shown in Figure 4.21 *a*. The comparison of the calculated reflectivity curve with the measured one (red line and data points in Figure 4.20) reveals that the magnetic moment in the LCMO layers is 2.1 μ_{B} per Mn atom. This value is considerably reduced with respect to the one of bulk LCMO (3.7 μ_{B} per Mn atom), but agrees rather well with the value of 2.4 μ_{B} per Mn atom obtained from dc magnetometry measurements. This reduced magnetic moment may be caused by an in-plane stress induced by the lattice misfit between the YPr0.4BCO and LCMO layers or between the substrate and the superlattice. Such a stress could be acting on the highly versatile magnetic properties of LCMO [31].

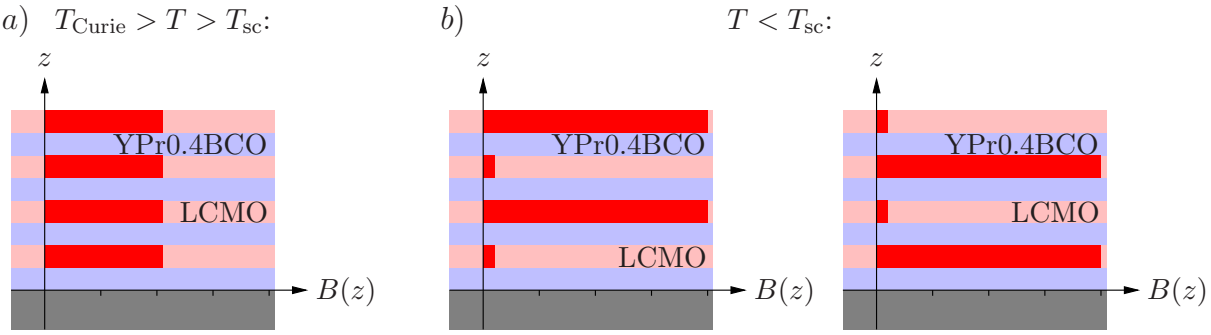

Figure 4.21: Sketches of the magnetic induction depth profile. The real sample discussed in the text contains 10 double layers, while the sketches contain for simplicity reasons only 4 double layers. *a*) Profile of the magnetic induction at $T_{\mathrm{Curie}} > T > T_{\mathrm{sc}}$. The magnetic moment in the LCMO layers is about $2.1\,\mu_{\mathrm{B}}$ per Mn atom. *b*) Profile of the magnetic induction at $T < T_{\mathrm{sc}}$. Every second LCMO layer has an enhanced magnetisation while the layers in between have a reduced magnetisation. There are laterally separated areas in the sample, where the phase of the modulation is different, i. e. areas, where the top layer has an increased magnetisation (*left*) and areas, where the top layer has a reduced magnetisation (*right*). The incoherent superposition of the signals from the different areas with different phases leads at the position of the fractional superlattice Bragg reflex to the same signal for the spin up and spin down neutrons. The maximum magnetic moment caused by the modulation is about $4.0\,\mu_{\mathrm{B}}$ per Mn atom, which is close to the LCMO bulk value of $3.7\,\mu_{\mathrm{B}}$ per Mn atom.

The reduced magnetic moment may also be caused by a small oxygen deficiency or a changed or inhomogeneous La and Ca distribution in the LCMO layers. Excluded as a possible origin is nonetheless a canting of the magnetic moments with respect to the applied magnetic field, since the values obtained from the simulation and the magnetisation measurements are about the same and since no sizeable spin flip signal has been observed at the position of the 1$^{\mathrm{st}}$ superlattice Bragg reflex (see Figure 4.18).

Modulation of the Magnetic Induction Profile at $T < T_{\mathrm{sc}}$: In a third step, a modulation with a periodicity of two double layers has been superposed to the magnetic induction profile obtained for $T_{\mathrm{Curie}} > T > T_{\mathrm{sc}}$ (see sketch in Figure 4.21 *b*). Two reflectivity curves have been calculated based on two profiles with different phases of the modulation. The first profile consisted of a modulation with an enhanced magnetic moment in the top layer (shown in Figure 4.21 *b* on the left hand side), while the second one comprised a reduced magnetic moment in the top layer (π-phase shift, shown in Figure 4.21 *b* on the right hand side). The two calculated reflectivity curves have been added incoherently. This step is justified by the assumption that the lateral area over which the modulation's phase is constant is larger than the lateral coherence length of the probing neutrons, i. e. several $10\,\mu$m. If the lateral areas of constant phase would be smaller, the neutrons would average over several such areas and see the same depth profile as above T_{sc}. This incoherent addition of two reflectivity curves from two profiles with different phase takes the fact into

account that the intensity measured at the position of the fractional superlattice Bragg reflex is for both neutron spin states the same (see Figure 4.16, 4.18 and 4.19). The reflectivity curve calculated by the use of this model has been compared to a reflectivity curve measured at 8 K (blue curve in Figure 4.20). The amplitude of the modulation of the magnetic moment has been determined to be about $1.9\,\mu_B$ per Mn atom. The maximum and minimum magnetic moments in the LCMO layers are therefore about $4.0\,\mu_B$ per Mn atom and $0.2\,\mu_B$ per Mn atom, respectively. It is remarkable that the maximum value is reasonably close to the LCMO bulk magnetic moment of $3.7\,\mu_B$ per Mn atom.

Judging from these numbers, the magnetic moments of the modulation must be located in the LCMO layers and not in the YPr0.4BCO layers. If the modulation would be located in the YPr0.4BCO layers, about $1.9\,\mu_B$ per Cu atom would be required to obtain the corresponding reflectivity curve. This value is way too large, since even in bulk $YBa_2Cu_3O_6$ the magnetic moment is only $0.5\,\mu_B$ per Cu. In hole doped YBCO films, it must be even smaller [93]. Besides, such a large magnetic moment cannot be explained in terms of magnetic vortices or other orbital currents that may arise from unconventional kinds of superconducting states.

The numbers obtained from this model give a good, qualitative idea of the observed phenomena. It is nonetheless evident that the model is not perfect: Figure 4.20 shows at the tail of the fractional superlattice Bragg reflex towards higher q_z-values a clear difference between the model and the experimental data. This can be explained by the fact that in reality the magnetic induction profile will not have a block-like shape as assumed in the simplified model and by the fact that the resolution of the instrument is difficult to simulate at $T < T_{STO}^{II} \approx 65\,K$. (The tilting of the surface facets at $T < T_{STO}^{II}$ changes the resolution of the measurement dramatically, as one can see from the shape of the edge of total reflection at 185 K, 65 K and 8 K.)

The large amplitude of the observed modulation is remarkable. It is most likely enabled by the highly versatile magnetic properties of LCMO, since in a conventional ferromagnet it would cost an amount of energy which could not be gained from the superconducting condensation in the neighbouring layers. The driving mechanism is even though not yet fully understood. It may be a real modulation in the magnetisation density, or it might have to do with the intrinsic phase segregation of LCMO into 100 - 200 nm large nanodomains that are in different magnetic states [31, 32, 33]. The latter mechanism could be explained in the following way: Above T_{sc}, about 53% of the nanodomains are in the ferromagnetic state with the full magnetic moment of $4.0\,\mu_B$ per Mn atom and the rest of the domains are either in a non-magnetic or antiferromagnetic state. When the modulation evolves below T_{sc}, the previously non-magnetic or antiferromagnetic domains could become ferromagnetic and align antiparallel from one LCMO layer to the next one (see sketch in Figure 4.22). Since the lateral extent of the nanodomains is smaller than the lateral coherence volume of the probing neutrons, such a scenario would be observed as an enhancement and a reduction of the mean magnetisation of the LCMO layers. The weak point of this explanation is, that the superconductivity would have to drive the state

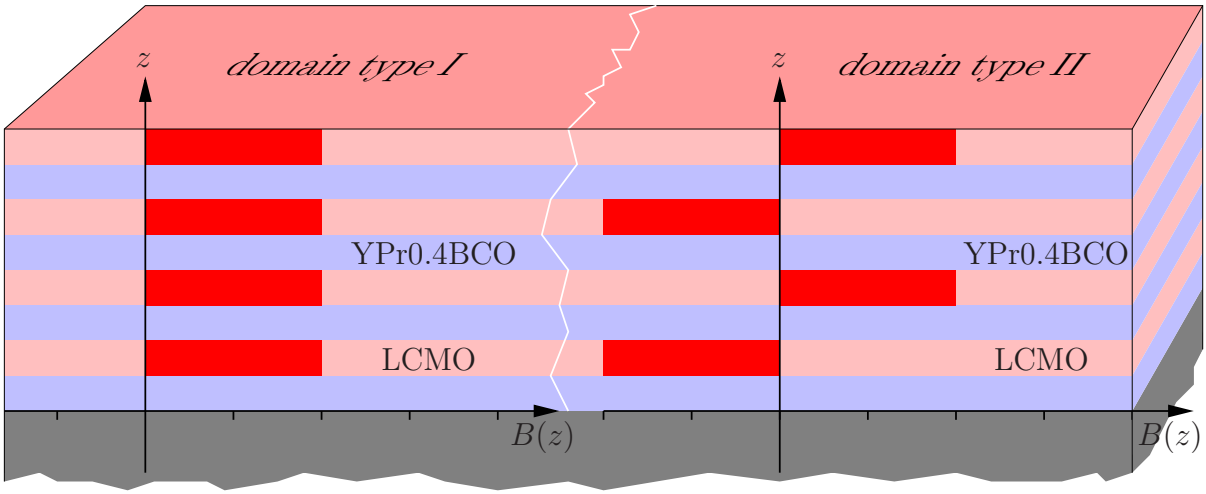

Figure 4.22: Sketch of a model of the magnetic induction depth profile that is different from the one shown in Figure 4.21: Above T_{sc}, some 53% of the magnetic domains carry the full magnetic moment of about $4.0\,\mu_B$ per Mn atom while the rest of the domains is in a non-magnetic or antiferromagnetic state. Below T_{sc}, the first type of domains remains unaffected, while the second type of domains becomes ferromagnetic and orders antiparallel from one LCMO layer to the next one. This scenario is even though less likely than the one presented in Figure 4.21, since the superconductivity would have to switch the magnetic state of the second type of domains.

of the domains from non-magnetic or antiferromagnetic to ferromagnetic. This is rather unlikely. A real modulation of the magnetisation density is thus much more conceivable.

Independently of the mechanism, one can conclude from the presented modelling that the sample is divided laterally into areas, where the phase of the modulation is different. These areas must be larger than the lateral coherence volume of the neutrons, i. e. larger than some $10\,\mu$m. Therefore, there is a significant lateral length scale of at least several $10\,\mu$m participating in the physics of the magnetic induction in these samples.

4.3.3 Orientation Dependence

Experiments on the fractional superlattice Bragg reflex were performed in two different sample orientations. From the first orientation to the second one, the sample was rotated by 90° around its surface normal. For these experiments, the sample was cooled in both orientations in $H_{appl} = 100\,$Oe from room temperature to $T < T_{sc}$. Only in one orientation, the fractional superlattice Bragg reflex was observed. If the sample was mounted in the other orientation, the fractional superlattice Bragg reflex did not appear (Figure 4.23 and 4.24). In the following, the orientation where fractional superlattice Bragg reflex was observed is referred to as *a-direction*, while the other orientation is referred to as *b-direction*. It is the same nomenclature for the orientation as the one used in section 4.1. There, it was shown that the substrate surface splits at $T_{STO}^{II} \approx 65\,$K into several surface facets that are tilted by up to 0.5° with respect to each other. The main tilting occurs in the same orientation as the fractional superlattice Bragg reflex. The external magnetic

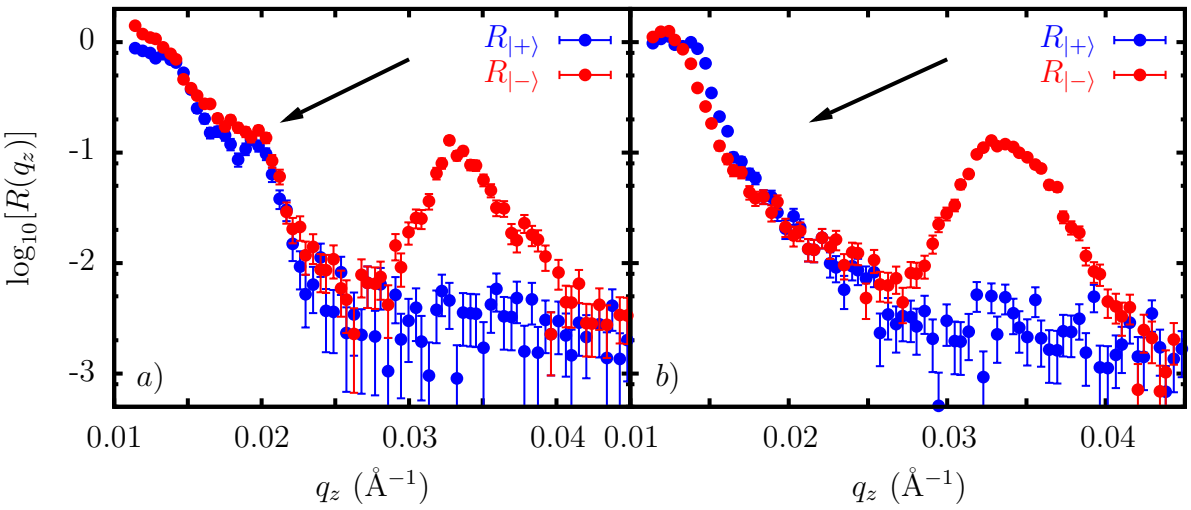

Figure 4.23: Orientation dependence of the fractional superlattice Bragg reflex measured at 15 K in $H_{\mathrm{appl}} = 100$ Oe. In orientation a, the fractional superlattice Bragg reflex appears below T_{sc}, while it does not appear, if the sample is rotated by 90° around its surface normal (orientation b). Sample: YPr04-LCM1

field used in the neutron experiments is in this case pointing along the longer extent of the surface facets (see sketch in Figure 4.25 a).

The uniaxial orientation of the structural surface facets in combination with the dependence of the fractional superlattice Bragg reflex on the direction of the applied magnetic field point towards some kind of strain effect that is required to enable the modulation of the magnetic induction profile. Since the modulation evolves only below T_{sc}, were no structural transition has been observed, the modulation seems to be finally triggered by superconductivity. However, the strain condition appears to be a prerequisite for this to happen.

4.3.4 Stress Dependence

The strain and stress dependence of the fractional superlattice Bragg reflex was investigated with polarised neutron reflectometry and macroscopic magnetometry measurements. A special sample holder was constructed to apply a uniaxial stress laterally on the substrate while cooling and measuring on a neutron reflectometer (Amor at SINQ, Paul Scherrer Institut, Switzerland). A second sample holder was constructed to perform corresponding stress dependent measurements on a Quantum Design Physical Properties Measurement System (PPMS with VSM option). For the neutron measurements, the sample holder was made of titanium. This material has a negative scattering length and therefore a refraction index which is for neutrons larger than one. Hence less of the neutrons that hit the sample holder are reflected into the detector and contribute to the background signal. This sample holder allows for a controlled application of the uniaxial pressure on the substrate by using four different spacers that clamp a spring with different strengths to a force of 0.5 N, 1.0 N, 1.5 N and 2.0 N (corresponding to 100, 200,

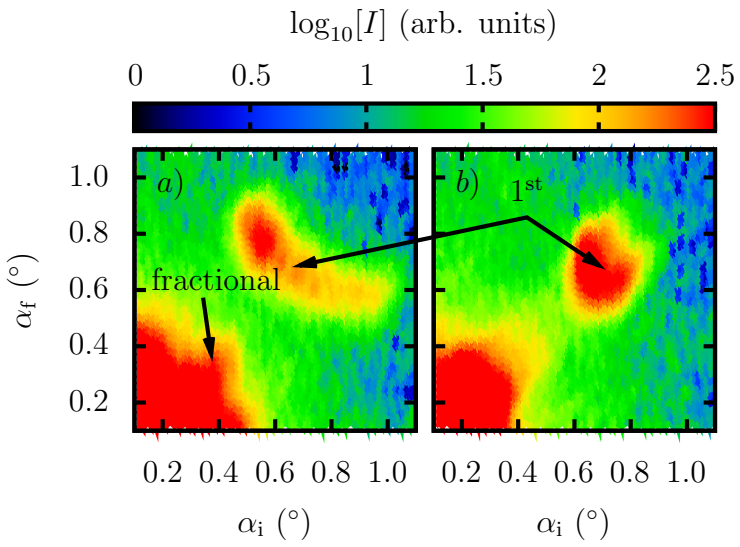

Figure 4.24: Orientation dependence of the fractional superlattice Bragg reflex measured at 15 K in $H_{\mathrm{appl}} = 100$ Oe. The angle of the incident beam α_{i} is plotted versus the angle of the scattered beam α_{f}. The colour scale is given by the logarithm of the measured intensity. The rocking scans ($\alpha_{\mathrm{i}} + \alpha_{\mathrm{f}} = \mathrm{const}$) are broad along the a-direction (a) and narrow along the b-direction (b). The fractional superlattice Bragg reflex is only visible along the a-direction. Sample: YPr04-LCM1

300 and 400 kPa, see Figure 4.25 b). Because the components of the sample holder have different thermal expansion coefficients the exact force applied on the substrate may have slightly deviated with temperature from the above given values. For the magnetometry measurements, the applied force was as well tuned by using different spacers clamping a spring with different strengths. This sample holder was made of Teflon (see Figure 4.25 e), because it can easily be processed and because it gives a minimal magnetic background signal in magnetometry measurements. The relaxation of the rather soft Teflon made the precise determination of the applied force even though impossible. Hence the amount of stress applied in the magnetometry measurements was less well defined than in the case of the neutron reflectometry measurements.

The neutron reflectometry measurements showed a lower threshold of the applied force above which the modulation in the magnetic induction profile evolves: In the measurement with an applied force of 1.5 N, the fractional superlattice Bragg reflex was visible, but had a rather small intensity. If the applied force was enhanced to 2.0 N, the modulation evolved fully (see Figure 4.26). In the magnetometry measurements, the magnetisation above $T_{\mathrm{STO}}^{\mathrm{II}}$ was independent of the applied stress. If the minimal possible force was applied, the magnetisation increased below $T_{\mathrm{STO}}^{\mathrm{II}}$ with decreasing temperature continuously and without any kinks. If the maximal possible force was applied, the behaviour of the magnetisation was depending strongly on the cooling speed. If the sample was cooled slowly (0.5 K/min), the slope of the magnetisation decreased below $T_{\mathrm{STO}}^{\mathrm{II}}$. If the sample was cooled fast (20 K/min), the slope of the magnetisation started to increase at $T_{\mathrm{STO}}^{\mathrm{II}}$ and decreased below T_{sc} again (see Figure 4.27). In the neutron measurements, the cooling speed could not be actively controlled. The closed cycle refrigerator used had a cooling speed above 100 K of about 3 K/min and below 100 K of about 4 - 5 K/min. The variation

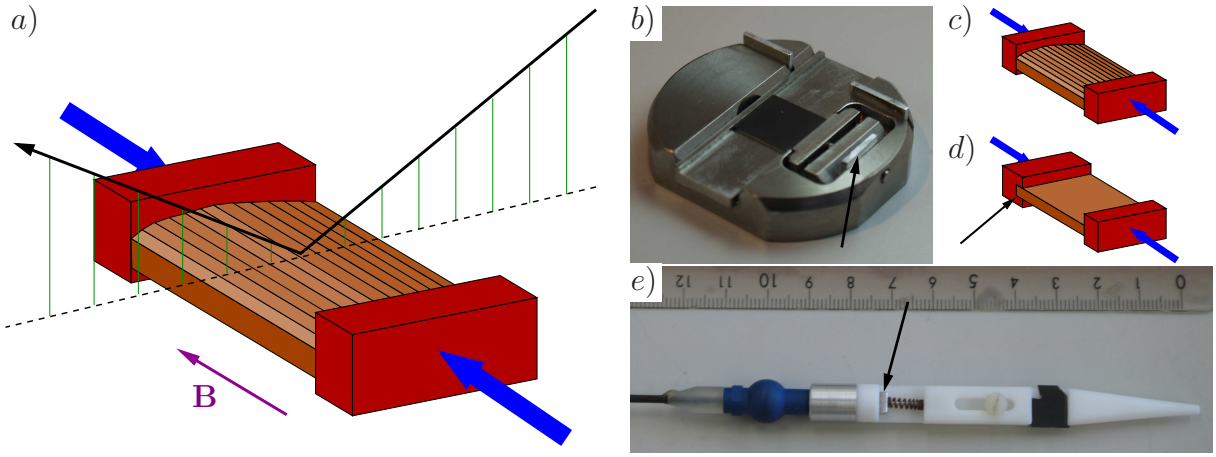

Figure 4.25: *a*) Sketch of the geometry used for the stress dependent measurements. The blue arrows indicate the direction of the applied stress. The direction of the applied magnetic field is indicated by the magenta arrow. The black arrow with the green lines indicates the scattering plane of the neutrons in the PNR measurements. The bent substrate with the surface facets is schematically shown (brown). *b*) Photograph of the sample holder used for the measurements performed on the Amor reflectometer at SINQ, Paul Scherrer Institut, Switzerland. The applied force can be tuned at room temperature within the range of 0.5 - 2.0 N with the help of different spacers that modify the clamping conditions of a spring (*black arrow*). The precise amount of stress may vary with temperature due to different thermal expansion coefficients. *c*) Sketch of the setup that allows the bending of the substrate. *d*) Sketch of the setup that hinders the bending of the substrate by placing the substrate on one side in a slot (*black arrow*). *e*) Photograph of the sample holder used for the measurements performed with a Quantum Design Physical Properties Measurement System (PPMS with VSM option). The applied force could be tuned with the help of different spacers hat modify the clamping conditions of a spring (*black arrow*). The exact applied force could not be determined due to the softness of the Teflon of which the sample holder is made of.

in temperature of the cooling speed was caused by the copper coolfinger and its specific heat capacity. Therefore, the dependence of the modulation on the cooling speed could not be investigated in further detail with neutrons. Nonetheless, this would be a very interesting aspect for further studies.

One can conclude from these measurements that the structural phase transition of the substrate at $T_{\mathrm{STO}}^{\mathrm{II}}$ has a sizeable impact on the magnetisation of the LCMO layers and on the magnetic induction depth profile in the investigated superlattices. At $T_{\mathrm{STO}}^{\mathrm{II}}$, crystallites with a rhombohedral structure evolve embedded in the otherwise tetragonal matrix [48]. It seems that this transition is itself very stress sensitive. Most likely, the force of 2.0 N (which is equivalent to a pressure of 400 kPa) applied uniaxially laterally on the substrate is either enough to force the rhombohedral crystallites to order in a preferential orientation or enough to enhance the volume fraction of the rhombohedral crystallites in the otherwise tetragonal matrix. Subsequently, this gives rise to a structurally ordered pattern throughout the substrate, which induces a stress in the superlattice. This does not occur, if the rhombohedral crystallites are less or randomly oriented. The stress

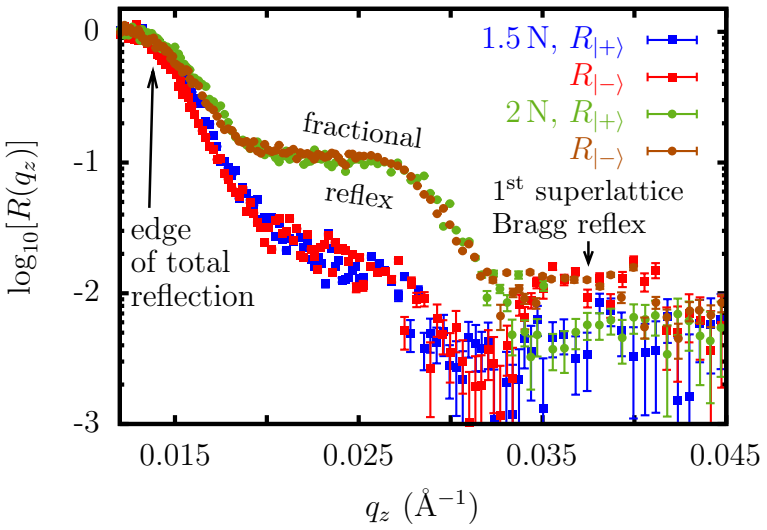

Figure 4.26: Stress dependent measurements with polarised neutrons at 15 K and $H_{\mathrm{appl}} = 100$ Oe along the a-direction. A force of 1.5 N applied on the substrate enables the fractional superlattice Bragg reflex with only a small intensity, while a force of 2.0 N enables it completely. Sample: YPr04-LCM6a

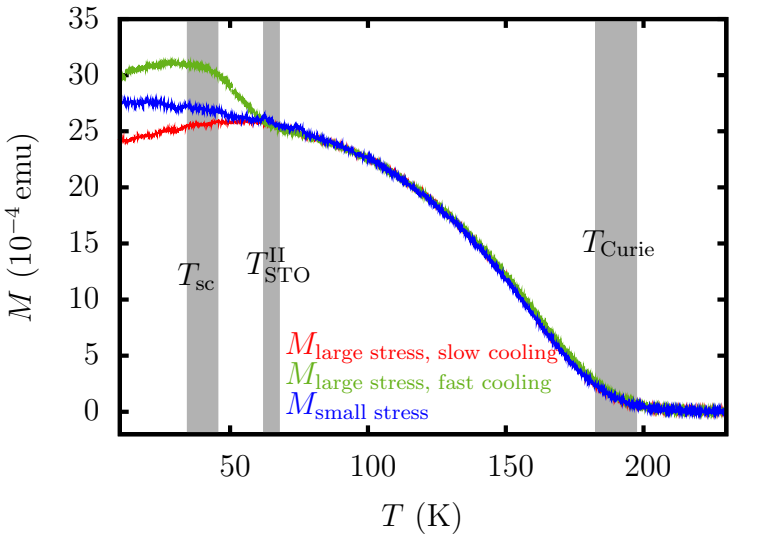

Figure 4.27: Stress dependent magnetometry measurements in $H_{\mathrm{appl}} = 100$ Oe along the a-direction. If the sample was cooled slowly (0.5K/min) with a large applied stress, the slope of the magnetisation turned down at $T^{\mathrm{II}}_{\mathrm{STO}}$. If the sample was cooled fast (20 K/min) with a large applied stress, the slope turned up at $T^{\mathrm{II}}_{\mathrm{STO}}$ and again down at T_{sc}. If the sample was cooled with a small applied stress, no kink was observed. Sample: YPr04-LCM1

induced on the superlattice modifies the magnetic properties of the LCMO. It changes the slope of the magnetisation curve at $T^{\mathrm{II}}_{\mathrm{STO}}$. The type of change in the slope depends even though on the speed of the sample cooling. If it is cooled fast enough, the slope increases at $T^{\mathrm{II}}_{\mathrm{STO}}$ and decreases again at $T_{\mathrm{sc}} = 40$ K. Otherwise, the slope decreases below $T^{\mathrm{II}}_{\mathrm{STO}}$. This cooling speed dependence is so far not understood, but indicates how versatile the electronic states of the LCMO behave under extrinsic stress. Already in bulk LCMO, several different magnetic states are energetically very close to the ground state [31]. A small external stress can therefore modify the balance between these states. Since the magnetisation depended in the experiments strongly on the cooling speed, it is likely that the system never reaches the ground states but changes between states very close to the ground state.

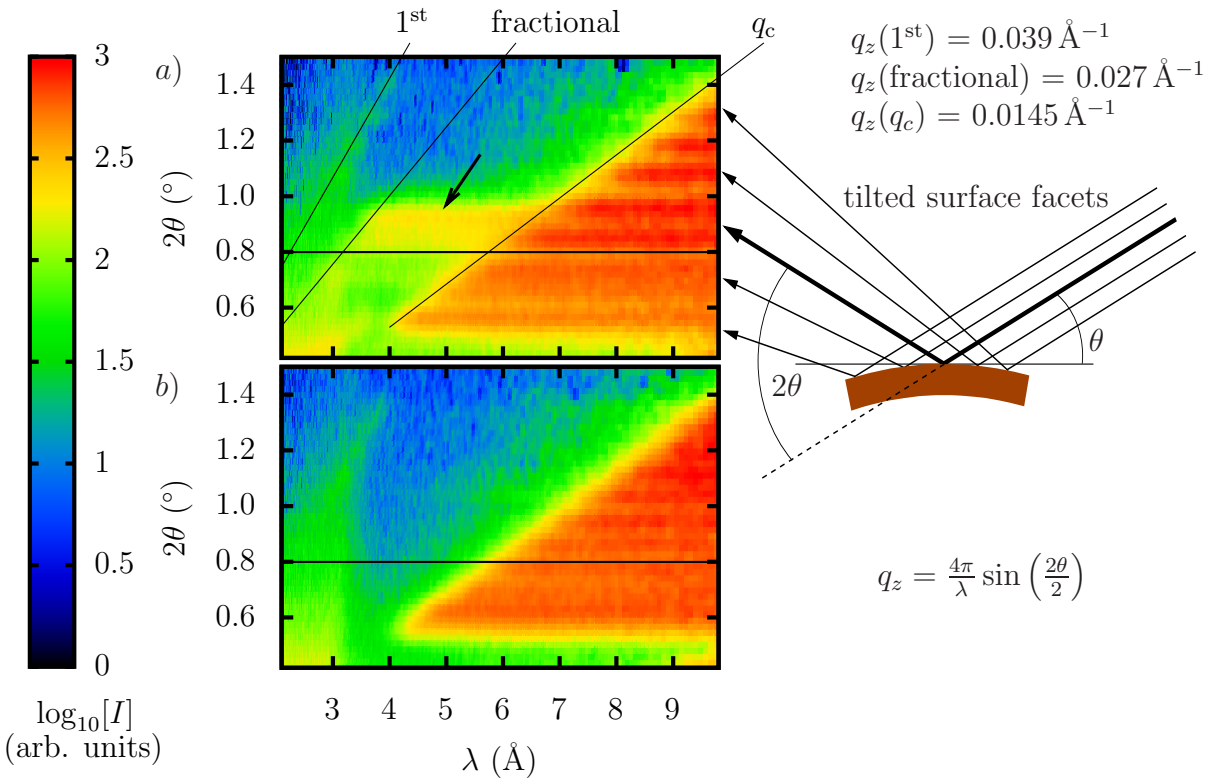

Figure 4.28: λ versus 2θ maps measured on a time of flight neutron reflectometer (Amor at SINQ, Paul Scherrer Institut, Switzerland) in the a-orientation at 8 K in $H_{\mathrm{appl}} = 100$ Oe: A range of wavelengths has been measured for each 2θ-angle. Due to the equation $q_z = \frac{4\pi}{\lambda}\sin\left(\frac{2\theta}{2}\right)$, horizontal cuts through the maps are equivalent to reflectivity curves. The substrate surface facets are tilted by 0.425°, leading at different 2θ-values ranging from 0.55° to 1.4° to specular reflectivity curves. *a)* A map measured with a uniaxial pressure of 400 kPa applied laterally on the substrate. The fractional superlattice Bragg reflex appears only on some of the substrate facets (*black arrow*). Lines with constant q_z-value are marked for the position of the edge of total reflection q_{c}, the fractional and the 1st superlattice Bragg reflex. *b)* A map measured with a uniaxial pressure of 200 kPa applied on the substrate. The fractional superlattice Bragg reflex does not appear. Sample: YPr04-LCM6a

This interplay of highly stress susceptible states is further confirmed by stress dependent reflectometry measurements on a time of flight neutron reflectometer with an area detector. Figure 4.28 displays a measurement at 8 K with an applied force of 2.0 N and a measurement with an applied force of 1.0 N. The sample was mounted for both measurements at an angle of $\theta = 0.4°$ between the mean surface and the incident beam. The intensity reflected from the sample has been measured time resolved at different scattering angles 2θ with respect to the incident beam. Therefore, the measurements are plotted as mappings with the neutron wavelength λ versus the scattering angle 2θ. In these plots, the horizontal lines at different, but constant 2θ-values are equivalent to specular reflectivity curves from surface facets that are tilted with respect to each other. The momentum transfer q_z can be calculated at each point with $q_z = \frac{4\pi}{\lambda}\sin\left(\frac{2\theta}{2}\right)$. The

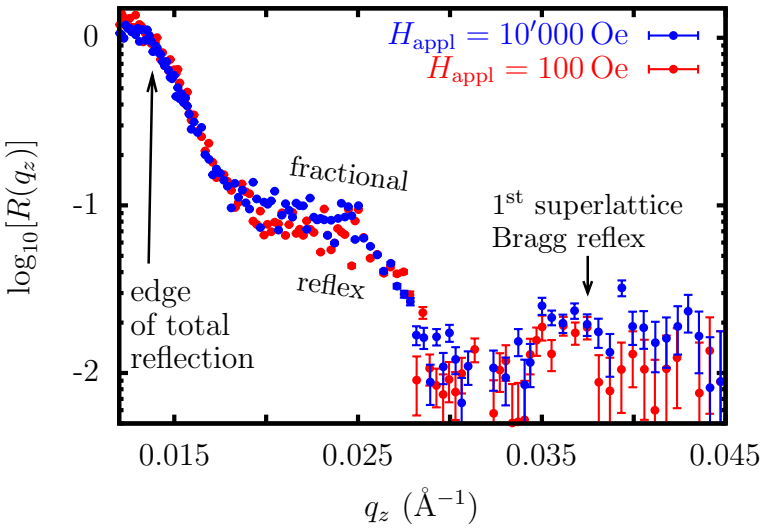

Figure 4.29: Neutron reflectometry measurements with spin down neutrons after cooling the sample from room temperature to 15 K in $H_{\mathrm{appl}} = 100$ Oe and $H_{\mathrm{appl}} = 10'000$ Oe, respectively. The sample has not been remounted for the two measurements. The only difference between the curves is a slightly smaller intensity at $q_z \approx 0.021$ Å^{-1} in the measurement at $H_{\mathrm{appl}} = 100$ Oe. Sample: YPr04-LCM6a

tilting of the surface facets is very well visible in these plots. Their angular spread in 2θ goes from 0.55° to 1.4°, which indicates a maximum tilting of the surface facets of 0.425°.

In order to make the images more readable, lines with constant momentum transfer q_z are indicated for the edge of total reflection (q_c), the fractional and the 1st superlattice Bragg reflex. It becomes clear from these lines, that the fractional superlattice Bragg reflex occurs only on some of the surface facets. This indicates that very specific stress conditions are required for the magnetic modulation to evolve.

4.3.5 Magnetic Field Dependence

Most aspects of the modulation of the magnetic induction depth profile have been discussed in the investigations presented above. Only the question of the modulation's persistence in an applied magnetic field has not been addressed so far. Since the modulation does not only enhance the mean magnetic moment in some LCMO layers but also reduces it in others, a strong applied magnetic field might suppress the modulation. To test this, reflectivity curves were measured after cooling the sample in different applied magnetic fields in the range of 100 Oe to 10′000 Oe from room temperature to 15 K. No significant difference between the curves was observed. For illustration, Figure 4.29 shows a reflectivity curve measured with spin down neutrons after cooling the sample in $H_{\mathrm{appl}} = 100$ Oe and a corresponding curve measured after cooling the sample in $H_{\mathrm{appl}} = 10'000$ Oe. Between these two measurements the sample was not remounted.

If one assumes the inhomogeneous model with the domains in the LCMO layers changing their electronic state at T_{sc}, one can accordingly estimate the minimum energy gained by the system when it forms the magnetic modulation: If a domain's full saturation moment of $4.0\,\mu_{\mathrm{B}}$ per Mn atom is oriented antiparallel to the applied magnetic field of $H_{\mathrm{appl}} = 10'000$ Oe, the energy penalty in this domain is about 0.45 meV per Mn atom. Subsequently, one can calculate the macroscopically averaged energy gain by using the

numbers obtained from the theoretical modelling in subsection 4.3.2 as 0.1 meV per Mn atom. This interpretation does not apply, if one assumes the model with the homogeneous magnetisation, where the magnitude of the magnetic moment changes from one LCMO layer to the next one. There, the macroscopic energy balance remains unchanged by the modulation.

4.3.6 Results and Interpretation

Neutron reflectometry measurements on samples with underdoped YBCO layers revealed the occurrence of a fractional superlattice Bragg reflex below $T_{sc} = 40\,K$. The position of this reflex in q_z depends on the way, the sample is mounted. Most often, it is located at the position of the 0.5^{th} superlattice Bragg reflex, which indicates a modulation of the magnetic induction depth profile with a periodicity of two double layers. This modulation must be superposed to the magnetic induction depth profile above T_{sc} and conserve on average the double layer periodicity of the latter one, since the intensity measured at the position of the 1^{st} superlattice Bragg reflex did not change at T_{sc}.

The average magnetic moment of the LCMO layers above T_{sc} and of the modulation below T_{sc} were determined by theoretical calculations to be about $2.1\,\mu_B$ per Mn atom and $1.9\,\mu_B$ per Mn atom, respectively. Below T_{sc}, the maximum and minimum magnetic moments of the LCMO layers were about 4.0 and $0.2\,\mu_B$ per Mn atom, respectively. Thus, the maximum value is reasonably close to the LCMO bulk moment of $3.7\,\mu_B$ per Mn atom.

Polarised neutron reflectometry measurements with spin analysis in combination with dc magnetometry measurements revealed that the magnetic moments of the modulation must be either aligned parallel or antiparallel to the externally applied magnetic field. Thus, there are two possible models for the modulation. In the first one, the magnitude of the magnetic moment is about constant within one LCMO layer and changes from one LCMO layer to the next one. In the second model, there are small domains in the LCMO layers which are non-magnetic or antiferromagnetic at $T > T_{sc}$. Below T_{sc}, they become ferromagnetic and couple antiparallel from one LCMO layer to the next one. This model is less likely because the superconductivity would have to switch the magnetic state of some domains in the LCMO layers. Supplementary neutron reflectometry measurements in an applied magnetic field of 1 T showed that in the second model the energy which is gained by the system for the formation of the modulation must be at least 0.1 meV per Mn atom in order to overcompensate this antiparallel alignment of the switched, ferromagnetic domains.

The formation of the magnetic modulation is very sensitive to stress that is induced extrinsically on the superlattice: Below $T_{STO}^{II} = 65\,K$, crystallites with a rhombohedral structure form in the otherwise tetragonal crystal matrix in the substrate. As shown by hard x-ray scattering experiments, the substrate surface bends below T_{STO}^{II} and splits into several anisotropic surface facets that are tilted along their shorter extent by up to 0.5° with respect to each other. Neutron reflectometry measurements showed further that the modulation occurs only, if the external magnetic field and a uniaxial pressure on the substrate of more than 300 kPa are applied along the direction of the longer extent of these facets. Even under these special conditions, the modulation occurs only on some of the

surface facets. This leads to the conclusion that the uniaxial pressure applied laterally on the substrate either favours an orientation of the rhombohedral crystallites or enhances their volume fraction in the tetragonal matrix. In both cases, additional strain is induced in the superlattice which is grown heteroepitaxially on top of the substrate. This extrinsic strain changes the magnetic properties of the LCMO layers as was confirmed by macroscopic magnetometry measurements, where the same pressure applied on the substrate forced a kink in the magnetisation curve at $T_{\mathrm{STO}}^{\mathrm{II}}$. The most conceivable explanation for this effect is that the extrinsic strain deforms the oxygen octahedrons in LCMO. Accordingly, the Mn-O-Mn bonds become more bent and the e_g-electron hopping rate and the e_g-band width become reduced. This increases the energy level of the double exchange ground state and increases the volubility of the electronic properties of the LCMO layers. With these prerequisites, the magnetic modulation finally occurs at T_{sc} triggered by a proximity effect between the superconducting and the ferromagnetic order parameter.

So far, only the source of the average magnetic moments in the LCMO layers and the magnitude of the moments have been discussed. It has been worked out that most likely the highly versatile magnetic properties of LCMO enable the modulation. But it has not been discussed, why the modulation may be energetically favourable for the system.

One option is an energy gain from a proximity effect between the ferromagnetic and the superconducting order parameters. Accordingly, one can develop a simple picture by the use of the concepts of the proximity effects introduced in subsection 2.1.6: There, the condensation energy in a superconductor has been calculated by assuming that the superconducting layer thickness is much smaller than the length scale over which the superconducting order parameter changes ($d_{\mathrm{sc}} \ll \xi_{\mathrm{sc}}$). Since the ratio between these lengths is opposite here, d_{sc} has to be replaced by ξ_{sc} for the calculations. Subsequently, one obtains a strongly simplified model, where the pair breaking takes only place in a region in interface vicinity and not in the entire superconducting layer. In this model one can introduce an exchange energy ΔE_{ex} for the two interfaces between the superconducting and the neighbouring ferromagnetic layers. This exchange energy is active in interface vicinity on a length scale of ξ_{sc} into the superconductor and of ξ_{FM} into the ferromagnet. The assumption that the ferromagnetic moments in the two ferromagnetic layers are different implies different exchange energies at the two interfaces. Assuming that they differ by 2ϵ, the exchange energies are given by $\Delta E_{\mathrm{ex}}^{\mathrm{I}} = \Delta E_{\mathrm{ex}} + \epsilon$ and $\Delta E_{\mathrm{ex}}^{\mathrm{II}} = \Delta E_{\mathrm{ex}} - \epsilon$, respectively. Accordingly, one obtains different superconducting zones for the two interfaces. If the ferromagnets are weak, i. e. if $1/\tau T_{\mathrm{sc0}} \ll 1$, these zones have different critical temperatures which are given by $T_{\mathrm{sc}}^{\mathrm{red\,I}} \approx T_{\mathrm{sc}}^{\mathrm{red}} - \frac{\pi\epsilon}{4\tau}$ and $T_{\mathrm{sc}}^{\mathrm{red\,II}} \approx T_{\mathrm{sc}}^{\mathrm{red}} + \frac{\pi\epsilon}{4\tau}$, respectively, where $T_{\mathrm{sc}}^{\mathrm{red}}$ has been calculated in Equation (2.5). Based on $T_{\mathrm{sc}}^{\mathrm{red\,I}}$ and $T_{\mathrm{sc}}^{\mathrm{red\,II}}$, one can calculate the total condensation energy of the two regions together:

$$E_{\mathrm{cond}}^{\mathrm{tot}} = -\gamma_0 \left(\frac{T_{\mathrm{sc}}^{\mathrm{red\,I}} - T}{T_{\mathrm{sc0}}} \right)^2 - \gamma_0 \left(\frac{T_{\mathrm{sc}}^{\mathrm{red\,II}} - T}{T_{\mathrm{sc0}}} \right)^2 \tag{4.1}$$

$$= -2\gamma_0 \frac{(T_{\mathrm{sc}}^{\mathrm{red}} - T)^2 + \left(\frac{\pi\epsilon}{4\tau}\right)^2}{T_{\mathrm{sc0}}^2}. \tag{4.2}$$

Therefore, the energy gain of a system with unequal exchange energies at the interfaces is enhanced by

$$\delta E_{\mathrm{cond}}^{\mathrm{tot}} = \frac{2\gamma_0}{T_{\mathrm{sc0}}^2} \left(\frac{\pi\epsilon}{4\tau}\right)^2 . \tag{4.3}$$

This strongly simplified calculation illustrates that there is indeed a gain in the superconducting condensation energy possible, if the exchange field at the interface varies through the superconducting layers from one to the next interface. If this gain is larger than the energy penalty which is required to rearrange the moments of the ferromagnet, it is possible to change the magnetic domains in the ferromagnet. Since the ferromagnetic layers are relatively thin (8.5 to 10 nm), it is conceivable that the magnetic moments will be modified throughout the entire LCMO layers. Hence, the energetically favoured different exchange fields at the two interfaces of the superconducting layers lead to the two double layer periodicity of the modulation which has been observed.

In the future, three aspects of the modulation in the magnetic induction depth profile should be investigated in more detail. The first two aspects aim for a more profound understanding of the mechanism which causes the modulation, while the third one is more about possible applications of the modulation in electromagnetic devices which can be used to switch the magnetic properties of the device by the application of an electric fields:

I) The dependence of the magnetic modulation on the doping level of the YBCO layers should be investigated further. This would allow for a better understanding of the coupling mechanism between the superconducting and the ferromagnetic order parameter which induces the modulation.

II) The magnetic field dependent measurements should be performed up to much higher applied magnetic fields than the 1 T which was applied in the context of this work. If a sufficiently strong field is applied, the modulation of the magnetic induction profile should become suppressed. If the inhomogeneous model with the non-magnetic or antiferromagnetic domains becoming ferromagnetic at T_{sc} is true, the energy gain of the system achieved by the modulation could be estimated.

III) The stress dependence of the modulation in the magnetic induction depth profile could be used to switch the modulation in a device. For example, it might be possible to orient the rhombohedral crystallites in the STO by applying a strong electric field on the substrate. This would be a path away from the application of a mechanical force, but would not allow a real switching of the device, since STO has to be cooled each time in the electric field or without electric field through $T_{\mathrm{STO}}^{\mathrm{II}} \approx 65\,\mathrm{K}$. A better option might be the use of a substrate showing a piezo-electric effect. This way, an applied electric field could directly and reversibly change the stress applied on the superlattice without heating up in between. Whether this change of applied stress would switch the device also at low temperature or whether the sample would still have to be heated up above T_{sc} is unknown. If yes, it would be possible to build an easy switchable device, where the magnetic properties can be strongly affected by the application of an electrical field.

4.4 Magnetisation Reversal Process

In this section, the magnetisation reversal process in a superlattice comprising eight $YBa_2Cu_3O_7$ (YBCO) / $La_{2/3}Ca_{1/3}MnO_3$ (LCMO) double layers is discussed. The superlattice was grown on a (001)-oriented $SrTiO_3$ (STO) substrate and the individual layers had a thickness of 25.6 nm each. The data presented here have been obtained from polarised neutron reflectometry measurements at different positions of an M-H-hysteresis loop that reached from $\mu_0 H_{\mathrm{appl}} = -7$ to $+7$ T. Initially, the sample was cooled in zero magnetic field to 5 K. Before performing the measurements at a particular field, the sample was saturated at $+7$ or -7 T, depending on the field configuration required. Since the measurements were performed at various fields ranging from from very small fields around the coercive field ($\mu_0 H_{\mathrm{coerc}} = 0.0282$ T) to very large fields of up to $\mu_0 H_{\mathrm{appl}} = 6$ T, a special experimental setup was used. This setup is introduced in the first part of this section. In the second part, the data are shown and discussed. The interpretation of the data is given in the last part.

4.4.1 Experimental Setup

The polarised neutron reflectometry measurements were performed at several positions of the M-H-hysteresis loop around the coercive field ($\mu_0 H_{\mathrm{coerc}} = 0.0282$ T) and at higher fields of up to 6 T. In order to access such a broad field range with polarised neutrons, two different configurations of the reflectometer were required. This was the only way to avoid zero field points in the neutron flight path which would lead to a depolarisation of the neutrons. The smaller applied fields of $\mu_0 H_{\mathrm{appl}} < 0.1$ T at the sample position were accessed by introducing an additional guide field between the polariser and the magnet coils. This guide field and the field applied at the sample position were pointing in the same direction which was assigned by the fixed polariser. The two neutron spin orientations were accessed by a Mezei-type spin flipper located in the neutron beam path after the polariser. In order to keep the neutrons polarised, the strength of the guide field has to exceed the strength of the stray field of the magnet coils (see Figure 4.30 *a*). For fields at the sample position that are larger than 0.1 T, the guide field was not sufficiently strong to compensate the stray field of the magnet coils. In that case, a different configuration of the reflectometer was used: The guide field was still pointing in the same direction, but instead of a separate guide field it was produced by the stray field of the magnet coils. This required that the field at the sample position was pointing in the opposite direction than in the low-field configuration. Since the neutrons had to pass from the field direction in the guide field to the opposite field direction at the sample position, a special field arrangement was required to keep them polarised. This was achieved by driving the two Helmholtz coils in an asymmetric mode (different currents in the two coils, see Figure 4.30 *b*). This way, the zero field point was shifted out of the neutron flight path. Due to this field arrangement, the neutrons performed a 180°-spin rotation on their way to the sample position [97].

The constraints of the fixed polariser and of not having any zero field point in the neutron flight path limited the accessible field range: Polarised neutron reflectometry mea-

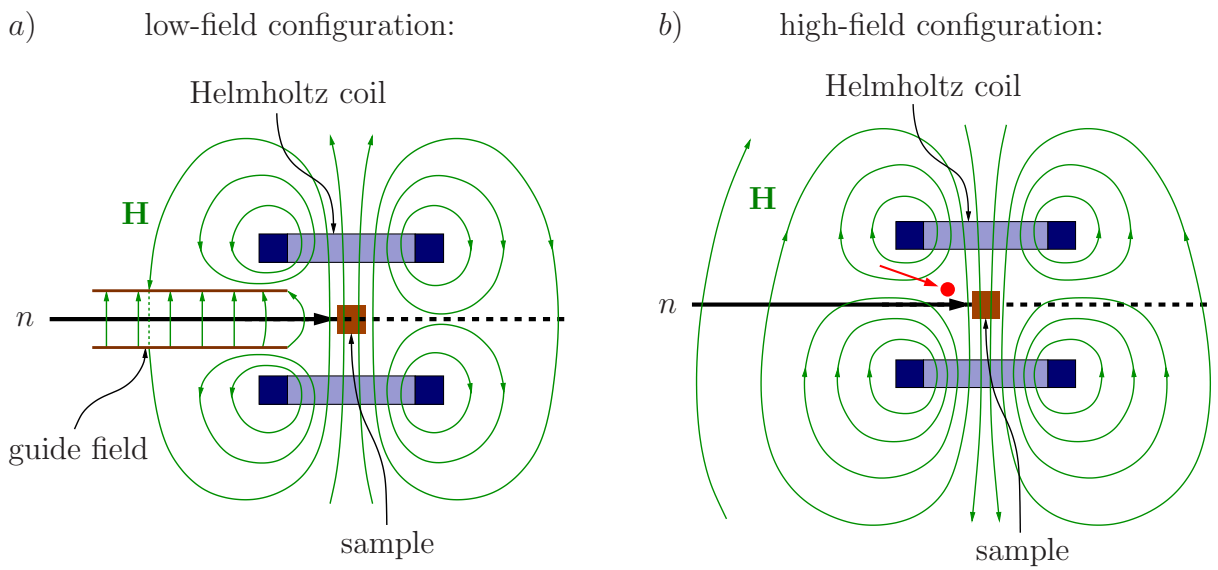

Figure 4.30: Sketch of the two configurations of the neutron reflectometer that were required to reach applied magnetic fields at the sample position in the range of 0 to 6 T with polarised neutrons: *a*) At applied magnetic fields of less than 0.1 T, an external guide field was used to compensate the stray field of the Helmholtz coils. The magnetic field in the entire flight path of the neutrons from the polariser to the sample was thus pointing in the same direction. This prevented the neutrons from depolarising before they reach the sample. *b*) If the applied magnetic field at the sample position was larger than 0.1 T, an external guide field would be too weak to compensate the stray field of the Helmholtz coils. Thus, the two Helmholtz coils were driven without external guide field in an asymmetric mode. Subsequently, the zero-field point was shifted away from the neutron flight path towards the coil with less current (*red point*). In this configuration, the stray field of the Helmholtz coils was used as a guide field: The neutrons performed a 180°-spin rotation on their path from the polariser to the sample and remained polarised. As a consequence, the magnetic field at the sample position was pointing in the opposite direction than in the low-field configuration.

surements in the high-field configuration could only be performed on the positive branch of the M-H-hysteresis loop, while measurements in the low-field configuration could only be performed on the negative branch. For the measurements presented here, this did not pose any problem, since the M-H-hysteresis loop measured by dc-magnetometry had the expected point symmetry, i. e. did not show an exchange bias (see Figure 3.1). Accordingly, the data obtained at the two sides of the M-H-hysteresis loop can be mirrored and directly compared with each other after correcting for the neutron polarisation efficiencies at the different applied fields. In the following, the data obtained in the high-field configuration ($\mu_0 H_{\mathrm{appl}} \geq 0.1\,\mathrm{T}$) are mirrored and given with a changed sign of the field strength in order to compare them with the data obtained in the low-field configuration.

In order to achieve applied magnetic fields of up to $\pm 7\,\mathrm{T}$ at the sample position, the sample was inserted in an Oxford cryomagnet. The accurate values of the applied magnetic fields were estimated after the experiment by measuring the magnetic fields at the sample position with a Hall probe which was inserted in the cryomagnet. This way, the error of the applied magnetic field has been estimated to be smaller than 4%, while

a remanence-induced offset of 0.0021 T has been found when changing the field direction after saturation in ±7 T. Due to this small errors, in the following the nominal field values are used.

4.4.2 Polarised Neutron Reflectometry Measurements on an *M*-*H*-Hysteresis Loop

The magnetisation reversal mechanism in a YBCO (25.6 nm) / LCMO (25.6 nm) superlattice was investigated by polarised neutron reflectometry measurements. The experiments were performed at 5 K, which is well below the ferromagnetic and the superconducting phase transition temperature $T_{\mathrm{Curie}} = 240\,\mathrm{K}$ and $T_{\mathrm{sc}} = 80\,\mathrm{K}$, respectively.

Figure 4.31 gives an overview over the magnetisation reversal process. Panel *a* shows a dc magnetometry measurement of the *M*-*H*-hysteresis loop from $\mu_0 H_{\mathrm{appl}} = -7$ to $+7$ T. The points indicate the positions, where the polarised neutron reflectivity curves were measured that are displayed in panels *b* to *f*. These representative curves document the major stages of the reversal process like in remanence after the saturation in +7 T *b*, during the reversal *c* and *d*, after the reversal but before saturation *e* and in saturation *f*. In panel *b*, the reflectivity curve in remanence is compared to the reflectivity curve measured in the non-magnetic state at room temperature (grey curve). At the position of the edge of total reflection, it shows a splitting of the intensities of the two neutron spin states which indicates a sizeable net magnetic moment in the sample pointing along the direction of the applied magnetic field. As seen by the splitting of the intensities at the position of the 1$^{\mathrm{st}}$ superlattice Bragg reflex, the contrast between the scattering length densities of the YBCO and the ferromagnetic LCMO layers is different for the two neutron spin states. It is enhanced for the spin down neutrons while it is reduced for the spin up neutrons. At the position of the structurally forbidden 2$^{\mathrm{nd}}$ superlattice Bragg reflex, the intensity is for both neutron spin states slightly enhanced compared to the curve in the non-magnetic state. This indicates a deviation of the magnetic induction depth profile from the structural depth profile which has been discussed in great detail in section 4.2.

Before the coercive field is reached in the magnetisation reversal process, the intensity at the position of the 1$^{\mathrm{st}}$ superlattice Bragg reflex changes from being higher for the spin down neutrons to being higher for the spin up neutrons (panels *c* and *d*). This change happens between $\mu_0 H_{\mathrm{appl}} = -0.023\,\mathrm{T}$ and $-0.028\,\mathrm{T}$, where the contrast between the scattering length densities of the YBCO and LCMO layers is balanced for the two neutron states. At the coercive field ($\mu_0 H_{\mathrm{coerc}} = -0.028\,\mathrm{T}$, panel *d*), no net magnetisation is observed in the upper most layers as seen at the edge of total reflection by the absence of any splitting of the intensities of the two neutron spin states. Nonetheless, the contrast between the two layers is already reversed as seen by the change of the maximum intensity from the spin down neutrons to the spin up neutrons at the position of the 1$^{\mathrm{st}}$ superlattice Bragg reflex. After the reversal process, the splitting at the edge of total reflection and at the positions of the 1$^{\mathrm{st}}$, 2$^{\mathrm{nd}}$ and 3$^{\mathrm{rd}}$ superlattice Bragg reflex is reversed as shown for $\mu_0 H_{\mathrm{appl}} = -0.1\,\mathrm{T}$ in panel *e*. The change from higher intensity for the spin up neutrons to higher intensity for the spin down neutrons at the position of the 2$^{\mathrm{nd}}$ superlattice Bragg reflex occurs between the coercive field and the state of reversed magnetisation.

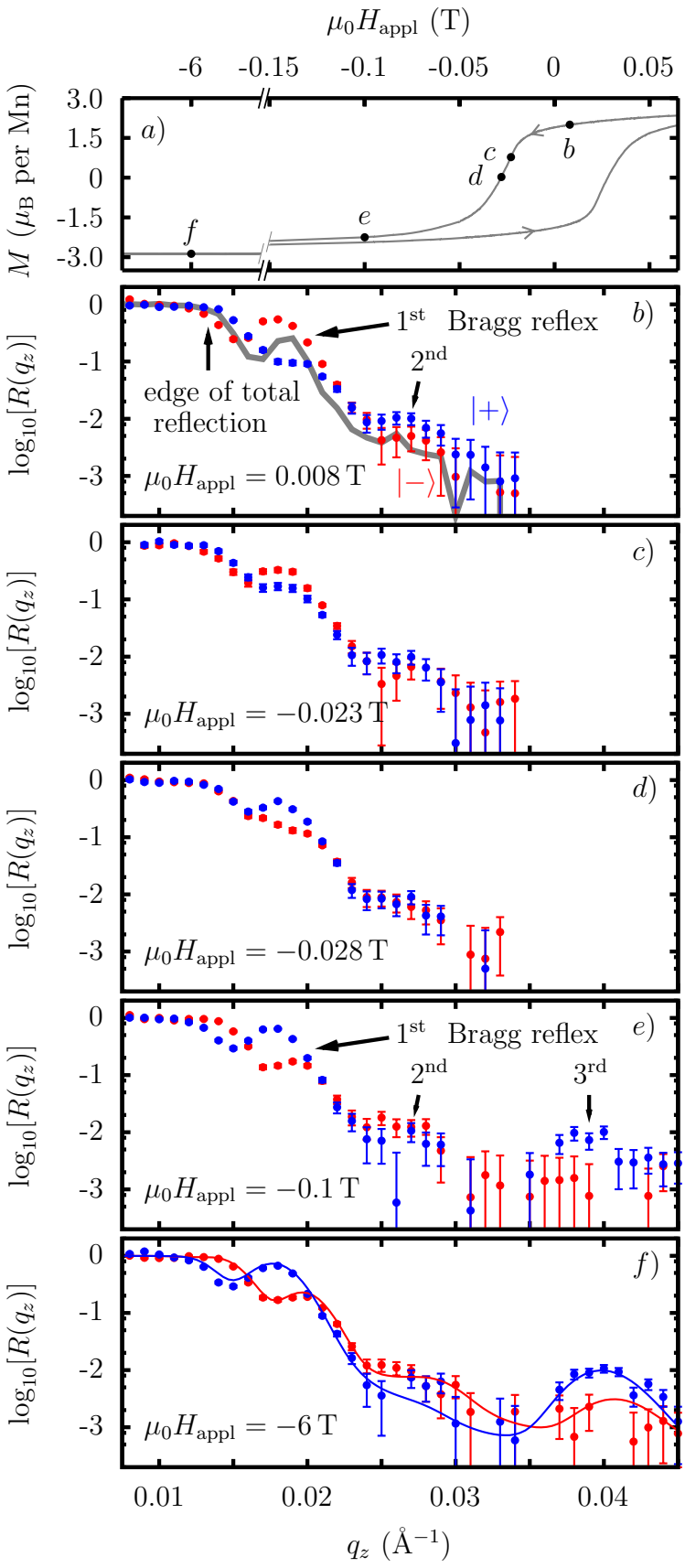

Figure 4.31: *a*) dc magnetometry measurement of the M-H-hysteresis loop with the diamagnetic signal of the STO substrate subtracted. The black points indicate the positions, where the polarised neutron reflectometry measurements shown in *b*) to *f*) have been measured: *b*) In remanence after the saturation in +7 T, *c*) before the coercive field, *d*) at the coercive field, *e*) after reversal and *f*) in saturation. The grey line in *b*) shows the measured reflectivity curve in the non-magnetic state at room temperature, while the solid lines in *f*) show reflectivity curves calculated from a theoretical model. The latter ones illustrate the compatibility with the theoretical modelling of the curves at large applied magnetic fields. During the reversal process, no theoretical model has been found to reproduce the data reasonably well. All reflectivity curves have been corrected for the polarisation efficiency of the instrument. Due to instrumental limitations, the measurements in *b*), *c*) and *f*) have been performed in opposite field direction than indicated (see subsection 4.4.1). Sample: Y-LCM70

Accordingly, one can conclude that the deviation of the magnetic induction depth profile from the structural one depends on the proper alignment of the ferromagnetic moments in the LCMO layers, since it reoccurs only when the magnetisation is reversed in major parts. Furthermore, it is interesting to note that this deviation persists even in saturation at -6 T (panel *f*). Both observations suggest a strong coupling between the occurrence of the deviation and the ferromagnetic moment in the LMCO layers.

In order to achieve a quantitative data evaluation, reflectivity curves were calculated for different models and compared with the experimental data. For higher magnetic fields, models of the magnetic induction depth profile were found that are similar to the ones discussed in subsection 4.2.2. This way, the magnetic moment in the ferromagnetic layers was determined as 3.0 to 3.5 μ_B per Mn atom. The precise value is model dependent. To illustrate the accuracy of the modelling at higher applied magnetic fields, one such simulation is compared in panel *f* with the experimental data obtained at $\mu_0 H_{appl} = -6\,T$. In contrast to this accurate modelling at higher applied magnetic fields, no suitable model of the magnetic induction depth profile could be found for the reflectivity curves obtained at applied magnetic fields around the coercive field. Neither a model which assumes a reversing of the magnetisation from positive to negative values in all layers simultaneously nor a model which assumes the reversal of the magnetisation of one layer after the other reproduced the experimental data reasonably well. This failure suggests that the magnetisation profile during the reversal process does not agree with the assumptions on which the matrix algorithm is based on (see subsection 2.2.1): The formalism assumes a depth profile of the magnetisation vertically to the layers. At each depth, a lateral average of the magnetisation is taken into account. Accordingly, the magnetisation is assumed to be either laterally homogeneous or to consist of magnetic domains that are smaller than the lateral coherence length of the neutrons. The failure of the modelling suggests therefore that I) a random reversal of small magnetic domains can be excluded, since it would be observed as a reversal of all layers simultaneously and that II) a reversal of small magnetic domains in one layer after the other can be excluded since it would be observed as a layer-by-layer reversal of the magnetisation.

The experimental data exclude further a uniform rotation of the magnetisation in the sample plane as reversal mechanism. As shown nicely by F. Radu *et al.* [98], the latter reversal process would be observed as a continuous intensity loss at the position of the edge of total reflection for the spin up neutrons combined with a continuous intensity gain at the position of the edge of total reflection for the spin down neutrons. Figures 4.31 and 4.33 illustrate that this is not applicable to the data presented here, since the edge of total reflection for the spin up and the spin down neutrons shift their positions in q_z during the reversal process instead of remaining at the same position and swapping intensity. Further, the data exclude a rotation of the magnetisation out of the sample plane because it would be observed as a reversal of the magnetisation in all layers. This is also unlikely since the out-of-plane axis is a hard axis for the magnetisation in YBCO / LCMO multilayers.

In order to shine more light on the mechanism of the magnetisation reversal process, more detailed measurements were performed in the range of $\mu_0 H_{appl} = 0.008\,T$ to $-0.048\,T$ around the coercive field (see Figure 4.33). It turned out that the curves at the intermediate applied fields can be reasonably well reproduced in terms of a linear

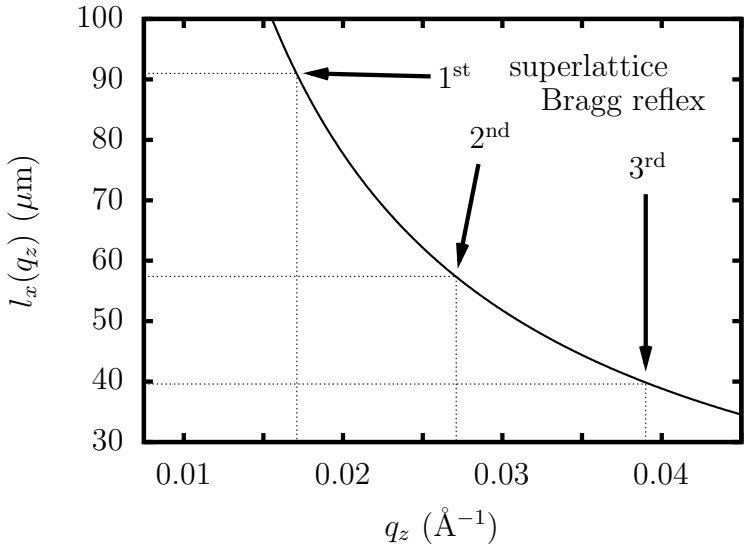

Figure 4.32: Lateral coherence length l_x of the probe beam according to Equation (2.58). This is an estimate of the upper limit of the coherence length. The positions in q_z of the 1st, 2nd and 3rd superlattice Bragg reflex of the investigated sample are indicated with black arrows.

combination of the measurements at $\mu_0 H_{\text{appl}} = 0.008\,\text{T}$ and $-0.048\,\text{T}$ according to the equation

$$R^{\pm} = xR^{\pm}_{-0.048\,\text{T}} + (1-x)R^{\pm}_{0.008\,\text{T}}. \tag{4.4}$$

Here, $R^{\pm}$ is the reflectivity for the spin up and the spin down neutrons, respectively, and x is a number that increases from 0 to 1 as a function of increasing field strength. This model assumes an incoherent superposition of simultaneously measured reflectivity curves (see page 37 and Figure 2.18) from magnetic depth profiles still in the remanent state and from profiles with an already reversed magnetisation. It implies that there are laterally in the sample plane different zones. In the reversal process, the magnetisation depth profile reverses in some of these zones earlier than in others. Since the neutrons average the magnetic depth profile over their coherence length, these zones must exceed the neutron coherence length which was in the present case several tens of micrometers (see Figure 4.32).

This result speaks for a rather complex reversal mechanism where most likely a fairly complex magnetic domain structure plays an important role. In order to develop a domain picture to describe the observed phenomena, the magnetisation reversal in a single layer is discussed first. There, the magnetisation may reverse in different ways. It may for example reverse in the form of moving domain walls. Then, the sample volume with reversed magnetisation increases continuously with progressing reversal. The magnetisation may also reverse in the form of a flipping of the domains, a rotation of the domains or even a rotation of the magnetisation of an entire layer. Which mechanism is the leading one depends crucially on the structural properties of the layer and on the homogeneity of the magnetisation or the intrinsic domain pattern. These factors steer the lateral coupling between the magnetic domains. If the layer consists for example of structural grains with a lateral extent of several micrometers, these will influence the reversal behaviour. If there are smaller domains within one grain, a collective reversal behaviour of the domains will be limited to the grain's volume. Also a moving domain wall will just reverse the magnetisation inside of the grain, while the neighbouring grains will be barely affected.

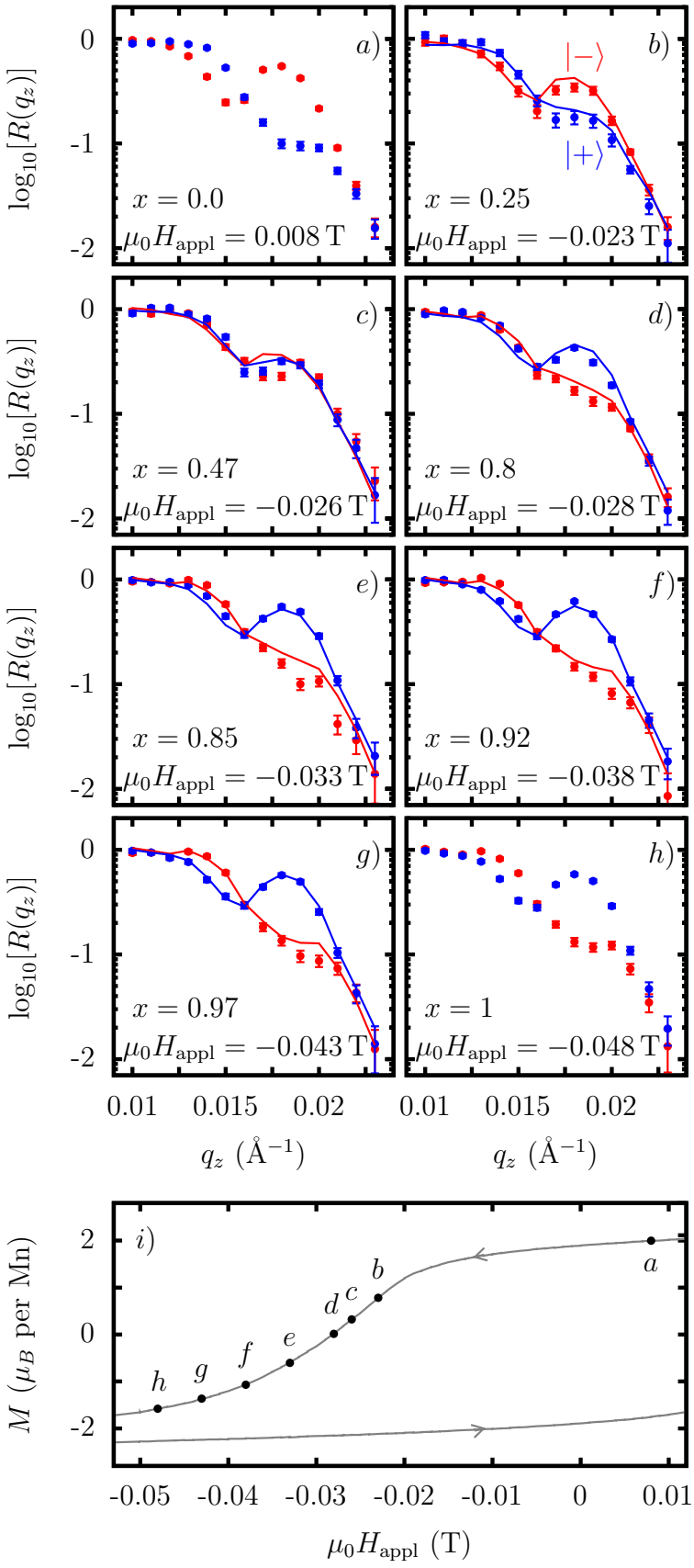

Figure 4.33: *a*) - *h*) Polarised neutron reflectivity curves measured during the magnetisation reversal process. The curves measured at the intermediate applied magnetic fields can be described in terms of a linear combination of the curves measured at $\mu_0 H_{\rm appl} = 0.008\,\mathrm{T}$ and $\mu_0 H_{\rm appl} = -0.048\,\mathrm{T}$. The points with the errorbars correspond to the measured data and the lines correspond to the linear combinations calculated with Equation (4.4) with x given in the respective figure. All curves are corrected for the polarisation efficiency of the instrument. *i*) M-H-hysteresis loop with the points indicated, where the reflectivity curves *a*) - *h*) have been measured. The M-H-hysteresis loop is corrected for the diamagnetic signal of the STO substrate. Sample: Y-LCM70

In the case of a multilayer system where every second layer is ferromagnetic, the magnetisation reversal process can be even more complex. In that case, the ferromagnetic layers may couple to or even across the spacer layers. Subsequently, a vertical coupling may become important in addition to the lateral coupling between the domains within each layer. Since the lateral coupling favours a magnetisation reversal in an entire ferromagnetic layer and the vertical coupling favours a combined reversal of the magnetisation in neighbouring layers, the stronger one will dominate the reversal process.

In the neutron reflectometry data presented on the reversal process in a YBCO / LCMO superlattice, a successive reversal of the magnetic depth profile in different zones in the sample plane has been observed. The lateral extent of these zones has been estimated to be at least of the order of several tens of micrometers. This result suggests that the intrinsic magnetic domains in LCMO which have a size of some hundred nanometers [31, 36] do not determine the characteristic length scale that governs the magnetisation reversal process. Instead, it is conceivable that the structural surface facets induced by the substrate below $T_{\mathrm{STO}}^{\mathrm{II}} \approx 65\,\mathrm{K}$ (see section 4.1) divide the sample laterally into separate zones. Strain effects reaching vertically through the entire superlattice are likely to follow the borders of the facets. (A similar, if not the same effect has been observed with magneto-optical methods on an LCMO layer grown on STO [56].) These strain effects may limit the collective reversal of the domains laterally to the area of the zones. Since the reversal of entire magnetic depth profiles has been observed, the magnetisation within the lateral zones appears to be coupled vertically. This means that the magnetisation in one zone reverses simultaneously in all ferromagnetic layers. This indicates that there is a vertical coupling through the superconducting YBCO layers which is stronger than the lateral coupling between the zones.

As a consequence of this model, it should be possible to describe the macroscopic magnetisation data with a similar kind of model which accounts for the evolution of the M-H-hysteresis loop in terms of a linear combination of the values measured at $\mu_0 H_{\mathrm{appl}} = 0.008\,\mathrm{T}$ and $\mu_0 H_{\mathrm{appl}} = -0.048\,\mathrm{T}$. Table 4.1 shows the corresponding x-values obtained for the reflectivity data and for the magnetometry data according to equation

$$M = xM_{-0.048\,\mathrm{T}} + (1-x)M_{0.008\,\mathrm{T}}. \tag{4.5}$$

Concerning the general trend, there is quite a good agreement, albeit there are some significant differences in the values which suggest that the vertical coupling is not strong

$\mu_0 H_{\mathrm{appl}}$	$x_{\mathrm{magnetometry}}$	$x_{\mathrm{reflectometry}}$
0.008 T	0.0	0.0
-0.023 T	0.34	0.25
-0.026 T	0.47	0.47
-0.028 T	0.56	0.8
-0.033 T	0.73	0.85
-0.038 T	086	0.92
-0.043 T	0.94	0.97
-0.048 T	1.0	1.0

Table 4.1: x-values of the linear combination $M = xM_{-0.048\,\mathrm{T}} + (1-x)M_{0.008\,\mathrm{T}}$ as determined from magnetometry measurements compared with x-values as determined from polarised neutron reflectometry measurements by $R^{\pm} = xR^{\pm}_{-0.048\,\mathrm{T}} + (1-x)R^{\pm}_{0.008\,\mathrm{T}}$.

enough to ensure that the magnetisation within each zone is reversed simultaneously in all ferromagnetic layers. This could also explain the deviations of the data from the linear combinations shown in Figure 4.33.

4.4.3 Results and Interpretation

Polarised neutron reflectometry measurements were performed at several positions of an M-H-hysteresis loop on a YBCO (25.6 nm) / LCMO (25.6 nm) superlattice grown on a (001)-oriented STO substrate. Initially, the sample was cooled in zero field to 5 K, which lies well below the ferromagnetic phase transition temperature $T_{\mathrm{Curie}} = 240\,\mathrm{K}$ and the superconducting phase transition temperature $T_{\mathrm{sc}} = 80\,\mathrm{K}$. The sample was saturated in $\pm 7\,\mathrm{T}$ before driving the external magnetic field to the values where the measurements were performed.

A fairly complex magnetisation reversal process was found. There are laterally in the sample plane different zones with an extent of at least several tens of micrometers. Within these zones, the magnetisation of the ferromagnetic layers is coupled across the YBCO layers and reverses in most, if not in all LCMO layers at the same time. Throughout the sample, it reverses successively in one zone after the other. This result is remarkable, since LCMO is known to segregate into domains that have a diameter of some hundred nanometers [31, 36] which is much smaller than the extent of the observed zones. Accordingly, the zones cannot be defined by the LCMO domains. Since the size of the zones corresponds to the size of the surface facets which evolve in STO substrates at temperatures below $T_{\mathrm{STO}}^{\mathrm{II}} \approx 65\,\mathrm{K}$, it is conceivable that the zones are formed by a strain pattern in the superlattice induced by the facets.

Besides the length scale of the lateral extent of the observed zones, the vertical coupling through the superconducting YBCO layers is the most important result presented in this section. Its origin is presently unknown. In addition to a dipolar coupling of the LCMO layers, there may be involved an electromagnetic coupling mechanism via the YBCO layers. The dipolar coupling is rather unlikely, since the dipolar fields in a distance of 25.6 nm from the next ferromagnetic layer are weak. The electromagnetic coupling is therefore more conceivable, even though it is unknown how this mechanism could work in detail. It could be either related to superconductivity or to a spin density wave as it was observed in some cuprate high-T_{c} superconductors [75, 76].

It is interesting to note that the reversal mechanism observed here is different from the one reported by V. Peña and co-workers for YBCO / LCMO superlattices [27] and by N.M. Nemes and co-workers for LCMO / YBCO / LCMO trilayers [99]. In both studies, the M-H-hysteresis loop showed for a YBCO layer thickness of less than 35 nm a step-like behaviour which indicates a layer-by-layer magnetisation reversal. Most likely, this difference is related to the different growth processes for the samples: The ones used here have been grown by pulsed laser deposition, while the ones used by V. Peña, N.M. Nemes and co-workers have been grown by high-pressure dc sputtering. The latter samples show a saturation magnetic moment of less than $2\,\mu_{\mathrm{B}}$ per Mn atom, which is considerably less than the $2.9\,\mu_{\mathrm{B}}$ per Mn atom of the sample investigated here. Additionally, in the sample investigated here, a YBCO layer has been grown first on the STO substrate. This is

different from the trilayers used by N.M. Nemes and co-workers, where an LCMO layer has been grown directly on top of the STO substrate. The latter leads to different stress conditions for the bottom LCMO layer and the top LCMO layer which is grown on the YBCO spacer layer. This leads most likely to the different reversal mechanism of the trilayers where one layer reverses after the other.

The investigation of the magnetisation reversal mechanism in YBCO / LCMO superlattices as presented here is not completed. One aspect which should be further investigated is the influence of the $SrTiO_3$ substrate on the formation of the lateral zones. This can be achieved relatively easily by performing the same measurements on a superlattice with the same thickness which is grown on a different substrate. Preferentially, this substrate should not undergo any structural phase transition in the temperature range from 5 K to room temperature. Possible candidates are thus (110)-oriented $NdGaO_3$ and (001)-oriented $LaAlO_3$.

Other interesting aspects which should be further investigated are the influence of the superconductivity on the vertical coupling of the magnetic domains and the length scale of the coupling. The former could be tested by performing the same measurements on the same sample at different temperatures around the superconducting phase transition at $T_{sc} = 80\,\mathrm{K}$, while the latter could be examined with experiments on samples where the YBCO layers have a different thickness.

5 Conclusions

The magnetic induction in heterostructures comprising thin layers of the high-T_c superconductor $YBa_2Cu_3O_7$ (YBCO) and the ferromagnet $La_{2/3}Ca_{1/3}MnO_3$ (LCMO) has been investigated by polarised neutron reflectometry. The samples comprised several repetitions of YBCO / LCMO double layers which were grown on (001)-oriented $SrTiO_3$ (STO) substrates. Supplementary hard x-ray measurements have been performed to examine the extrinsic influence of the structural phase transitions of STO on the magnetic induction in the heterostructures. The latter measurements revealed that at about 150 K a weak buckling of the substrate surface develops. This buckling can be attributed to the cubic-to-tetragonal phase transition of STO which occurs at $T_{\mathrm{STO}}^{\mathrm{I}'} \approx 150\,\mathrm{K}$ in the near-surface region and at $T_{\mathrm{STO}}^{\mathrm{I}} \approx 104\,\mathrm{K}$ in the bulk material. They revealed further that below 65 K the substrates bend. This bending is most likely induced by a structural phase transition at $T_{\mathrm{STO}}^{\mathrm{II}} \approx 65\,\mathrm{K}$, where crystallites with a rhombohedral structure evolve in the otherwise tetragonal crystal matrix. The formation of these crystallites leads to a stress which is relaxed by the bending. Subsequently, anisotropic facets evolve at the substrate surface which are tilted by up to 0.5° with respect to each other. Along their shorter extent, these facets have an extent of at least several tens of micrometers. It is conceivable that they cause a strain pattern in heterostructures that are grown heteroepitaxially on the STO surface. This pattern consists of a homogeneous strain on the area of the facets and a variation of the strain at the borders of the facets. It is very likely to influence the magnetic induction in the investigated heterostructures.

At the interfaces between the YBCO and LCMO layers, a deviation of the magnetic induction depth profile from the structural depth profile has been observed. Independently of the individual layer thickness, this deviation occurs below a temperature $T' \approx 120$ - 150 K and exhibits a length scale of about 1 - 2 nm around the interfaces. Most likely, it consists of a combination of a reduced ferromagnetic moment on the LCMO side of the interfaces and a ferromagnetic moment induced on the YBCO side of the interfaces that is aligned antiparallel to the one in the LCMO layers. The latter is less than $0.2\,\mu_{\mathrm{B}}$ per Cu atom and may either be induced by a precursor superconductivity or by a Cu-O-Mn super exchange which couples the Cu-spins and the Mn-spins antiparallel through the interfaces. The reduced magnetic moment on the LCMO side of the interfaces may be caused by a coupling of the ferromagnetic order parameter to the superconducting order parameter, a charge transfer across the interfaces, a change in the oxygen stochiometry or a strain due to a lateral lattice mismatch with the YBCO layers. The occurrence of this deviation may additionally be supported by an extrinsic stress induced by the cubic-to-tetragonal phase transition of the STO substrate surface at around $T_{\mathrm{STO}}^{\mathrm{I}'} \approx 150\,\mathrm{K}$.

Besides the deviation of the magnetic induction depth profile from the structural one, a coupling of the ferromagnetic layers through the superconducting layers has been observed. This coupling leads to a complex reversal behaviour of the magnetisation. Laterally, the magnetisation is segregated into zones with an extent of at least several tens of micrometers. Within each such zone, the magnetisation reverses in most, if not all layers at the same time. Throughout the sample, it reverses successively in one zone after the other. This is remarkable, since LCMO is known to segregate into domains that are in a ferromagnetic state and domains that are in a non-magnetic or antiferromagnetic state. These domains have a diameter of some hundred nanometers and are thus much smaller than the area of the zones within which the magnetisation reverses correlated. Since the reversal process has been only investigated at 5 K, it is unknown, whether the coupling across the superconducting layers is driven by superconductivity, by the dipolar fields that originate from the interface roughness or by a spin density wave that is induced in the YBCO layer due to the adjacency to the ferromagnetic LCMO layers. A distinction between these three options has not been possible. Nonetheless, a coupling of the dipolar fields is least likely, since the stray fields decay rapidly into the YBCO layers and are thus weak in the next LCMO layer. Most likely, the segregation of the magnetisation into the lateral zones is induced by the structural phase transition of the STO substrate at $T_{\mathrm{STO}}^{\mathrm{II}} \approx 65\,\mathrm{K}$. Below this temperature, anisotropic surface facets evolve that are tilted with respect to each other. Since the size of these facets and the size of the zones are about the same, it is conceivable that these facets induce a strain in the superlattice which is homogeneous on the area of the facets and different at the borders of the facets. Accordingly, the zones can be assigned to the surface facets of the substrate.

If underdoped YBCO ($Y_{0.6}Pr_{0.4}Ba_2Cu_3O_7$) is substituted for the optimally doped YBCO in the superlattices, below the superconducting phase transition temperature $T_{\mathrm{sc}} \approx 40\,\mathrm{K}$ a modulation of the ferromagnetic moment from one LCMO layer to the next one occurs. This modulation is superposed to the depth profile of the magnetic induction above T_{sc}. There, the average magnetic moment of the LCMO layers is uniformly about $2.1\,\mu_{\mathrm{B}}$ per Mn atom. Below T_{sc}, the maximum and minimum magnetic moments of the LCMO layers are about $4.0\,\mu_{\mathrm{B}}$ per Mn atom and $0.2\,\mu_{\mathrm{B}}$ per Mn atom, respectively. Most likely, the large amplitude of the modulation of about $1.9\,\mu_{\mathrm{B}}$ per Mn atom is enabled by the highly versatile electronic and magnetic properties of LCMO. This is further supported by the fact that very specific extrinsic stress conditions are required for the modulation to occur. In the present case, these conditions have been achieved by influencing a structural phase transition of the STO substrates at $T_{\mathrm{STO}}^{\mathrm{II}} \approx 65\,\mathrm{K}$, where crystallites with an rhombohedral structure evolve in the otherwise tetragonal matrix: A uniaxial pressure of 400 kPa applied laterally on the substrate turned out to be enough to either align these crystallites or to increase their volume fraction in the substrate and to subsequently create the stress conditions in the superlattice which allow for the superconductivity to induce the modulation below T_{sc}.

6 Outlook

The presented investigations should be extended in a rigorous manner to parameters like the thickness of the individual layers, the doping level of $YBa_2Cu_3O_7$ (YBCO), the highly versatile electronic properties of $La_{2/3}Ca_{1/3}MnO_3$ (LCMO) and the substrate-induced stress on the heterostructures. This would allow for a more profound understanding of the observed phenomena and might even reveal additional effects which have not yet been discovered.

- A variation of the individual layer thickness would indicate the length scales of the observed coupling of the ferromagnetic layers through the superconducting layers.
- Varying the doping level of the YBCO layers would reveal the influence of superconductivity on the observed phenomena. This could either be achieved by substituting a fraction of Pr-atoms for Y-atoms ($Y_{1-x}Pr_xBa_2Cu_3O_7$) or by controlling the oxygen content of the YBCO layers.
- The use of a ferromagnet with less versatile electronic properties than LCMO would reveal the sensitivity of the observed couplings with respect to the electronic properties of the ferromagnet. Therefore, LCMO should be replaced by a ferromagnet like for example $La_{2/3}Sr_{1/3}MnO_3$ (LSMO) which has similar in-plane lattice parameters as YBCO and thus would allow for a heteroepitaxial growth of heterostructures.
- Varying the extrinsic strain conditions in the heterostructures would allow for a better differentiation between intrinsic and extrinsic phenomena. This could be achieved by using substrate materials which do not undergo any structural phase transition in the investigated temperature range. Promising candidates for such substrates would be (110)-oriented $NdGaO_3$, (001)-oriented $LaAlO_3$ or (001)-oriented $BaTiO_3$. At lower temperatures, the latter material is brittle but shows a piezoelectric effect. This would allow for an intentional tuning of the stress conditions in one and the same superlattice by the simple application of an electric field.

This parameter space has already partially been probed during the presented investigations. The question, which parameters should be varied additionally to get more knowledge of which phenomena is discussed in the following paragraphs. Ideas for the further investigation of the structural phase transitions of the $SrTiO_3$ substrates are not discussed because these structural investigations were not the main topic of this thesis.

In order to further investigate the origin of the deviation of the magnetic induction depth profile from the structural depth profile, the doping level of the YBCO layers should

be varied first. If T' changes with the doping of the YBCO layers, the antiparallel magnetic moment on the YBCO side of the interfaces is most likely related to a precursor superconducting state. Polarised neutron reflectometry measurements would reveal the temperature dependence and the size of the region around the interfaces where the deviation occurs. In addition, x-ray magnetic circular dichroism (XMCD) measurements should be performed. Due to the element specific nature of this method, they would show more clearly on which side of the interfaces which changes occur. In a second step, experiments on samples with different substrates should be performed. This would probe the deviation for the possible influence of extrinsic strain which is possibly induced by a structural phase transition of the $SrTiO_3$ (STO) substrate surface.

So far, the magnetisation reversal process has only been investigated at 5 K. Therefore, it makes sense to investigate it in a first step as a function of temperature. If the coupling becomes reduced at $T_{sc} = 80\,K$, a superconductivity-induced origin is the most likely one. If the coupling becomes reduced at the structural phase transition temperature $T^{II}_{STO} \approx 65\,K$ of the substrate, the origin is more likely related to extrinsic strain effects. But since T_{sc} and T^{II}_{STO} are relatively close, additional YBCO doping dependent and substrate material dependent measurements should be performed to verify the interpretation. The latter of these two measurement series is of special interest, since the magnetisation of the sample was found to be laterally segregated into zones. The size of these zones corresponds to the one of the surface facets that evolve in STO substrates at T^{II}_{STO}. Therefore, it is conceivable that the magnetisation reversal process looks different if the facet-induced strain pattern is missing. In addition to these measurement series, a third series should be performed as a function of the individual layer thickness. This would reveal the length scale of the observed coupling.

The modulation of the magnetic induction depth profile observed in superlattices with underdoped YBCO ($Y_{0.6}Pr_{0.4}Ba_2Cu_3O_7$) in place of optimally doped YBCO should be investigated further. In a first step, the doping dependence of this modulation should be explored. In this context, it would also be interesting to probe the energy scale of the modulation in dependence of the doping of the YBCO layers. This could be achieved by cooling the samples in a large magnetic field. The strength of the applied magnetic field which is sufficient to suppress the modulation would indicate the mean energy which the system gains for the formation of the modulation. In a second step, the influence on the modulation of the versatile electronic and magnetic properties of LCMO should be probed. Therefore, $La_{2/3}Sr_{1/3}MnO_3$ (LSMO) could be substituted for LCMO, since it has very similar in-plane lattice parameters as LCMO but shows less versatile electromagnetic properties. In a third step, the length scale of the coupling of the magnetisation across the superconducting layers should be examined. This could be achieved by varying the thickness of the underdoped YBCO layers. In a fourth step, possible applications of the modulation should be investigated. For example, it could be tried to influence the modulation more intentionally via the extrinsic strain conditions. One option would be to align the rhombohedral crystallites in the STO substrate by applying an electric field during the cooling of the sample. A second, maybe even more elegant way, would be the use of a substrate which shows a piezo-electric effect. This might allow for a switching of the magnetic modulation at temperatures below T_{sc} by applying an electric field.

Appendix

Publications and Presentations

Publications as First Author

Giant superconductivity-induced modulation of the ferromagnetic magnetisation in a cuprate-manganite superlattice

J. Hoppler, J. Stahn, Ch. Niedermayer, V. K. Malik, H. Bouyanfif, A. J. Drew, M. Rössle, A. Buzdin, G. Cristiani, H.-U. Habermeier, B. Keimer and C. Bernhard

Nature Materials **8**, 315-319 (2009)

X-ray study of structural domains in the near-surface region of $SrTiO_3$ substrates with $Y_{0.6}Pr_{0.4}Ba_2Cu_3O_7$ / $La_{2/3}Ca_{1/3}MnO_3$ superlattices grown on top

J. Hoppler, J. Stahn, H. Bouyanfif, V. K. Malik, B. D. Patterson, P. R. Willmott, G. Cristiani, H.-U. Habermeier and C. Bernhard

Physical Review B **78**, 134111 (2008)

Publications as Co-Author

Direct measurement of the electronic spin diffusion length in a fully functional organic spin valve by low-energy muon spin rotation

A. J. Drew, J. Hoppler, L. Schulz, F. L. Pratt, P. Desai, P. Shakya, T. Kreouzis, W. P. Gillin, A. Suter, N. A. Morley, V. K. Malik, A. Dubroka, K. W. Kim, H. Bouyanfif, F. Bourqui, C. Bernhard, R. Scheuermann, G. J. Nieuwenhuys, T. Prokscha and E. Morenzoni

Nature Materials **8**, 109-114 (2009)

Intrinsic Mobility Limit for Anisotropic Electron Transport in Alq3

A. J. Drew, F. L. Pratt, J. Hoppler, L. Schulz, V. Malik-Kumar, N. A. Morley, P. Desai, P. Shakya, T. Kreouzis, K. W. Kim, A. Dubroka and R. Scheuermann

Physical Review Letters **100**, 116601 (2008)

Magnetic proximity effect in perovskite superconductor / ferromagnet multilayers

J. Stahn, J. Chakhalian, Ch. Niedermayer, J. Hoppler, T. Gutberlet, J. Voigt, F. Treubel, H.-U. Habermeier, G. Cristiani, B. Keimer and C. Bernhard

Physical Review B **71**, 140509(R) (2005)

Seminars

Giant modulation of the magnetic profile in $Y_{0.6}Pr_{0.4}Ba_2Cu_3O_7 / La_{2/3}Ca_{1/3}MnO_3$ superlattices

Laboratory for Neutron Scattering, Paul Scherrer Institut, Switzerland, 08.11.2007

Depth-profile of the magnetic induction in high-T_C superconductor / ferromagnet multilayers

Laboratory for Neutron Scattering, Paul Scherrer Institut, Switzerland, 20.12.2005

Contributed Talk

Polarized neutron reflectometry measurements on perovskite superconductor / ferromagnet multilayers

PNCMI 2006, Berlin, Germany, 25.09.2006

Invited Talks

Stress induced modulation of the magnetic profile in $Y_{0.6}Pr_{0.4}Ba_2Cu_3O_7 / La_{2/3}Ca_{1/3}MnO_3$ superlattices

Max-Planck-Institut für Festkörperforschung Stuttgart, Germany, 14.03.2008

Investigation on the magnetic ordering in perovskite-like Superconductor / Ferromagnet Multilayers

National Research Council, Chalk River, Canada, 29.03.2007

Posters

Superconductivity-induced modulation of the magnetisation profile in $Y_{0.6}Pr_{0.4}Ba_2Cu_3O_7 / La_{2/3}Ca_{1/3}MnO_3$ superlattices

J. Hoppler, J. Stahn, Ch. Niedermayer, H. Bouyanfif, V. K. Malik, P. Willmott, B. Patterson, D. Meister, G. Cristiani, H.-U. Habermeier, B. Keimer, A. Drew and C. Bernhard

NCCR Workshop on Nanoscience, Davos, Switzerland, 4. - 6. June 2008

Superconductivity-induced modulation of the magnetisation profile in $Y_{0.6}Pr_{0.4}Ba_2Cu_3O_7 / La_{2/3}Ca_{1/3}MnO_3$ superlattices

J. Hoppler, J. Stahn, Ch. Niedermayer, H. Bouyanfif, V. K. Malik, P. Willmott, B. Patterson, D. Meister, G. Cristiani, H.-U. Habermeier, B. Keimer, A. Drew and C. Bernhard

International Symposium on Neutron Scattering, Bhabha Atomic Research Center, Mumbai, India, 15. - 18. January 2008

Superconductivity-induced modulation of the magnetisation profile in $Y_{0.6}Pr_{0.4}Ba_2Cu_3O_7 / La_{2/3}Ca_{1/3}MnO_3$ superlattices

J. Hoppler, J. Stahn, Ch. Niedermayer, H. Bouyanfif, V. K. Malik, P. Willmott, B. Patterson, D. Meister, G. Cristiani, H.-U. Habermeier, B. Keimer, A. Drew and C. Bernhard

2007 Swiss Workshop on Materials with Novel Electronic Properties, Les Diablerets, Switzerland 28. - 30. September 2007

Magnetic Induction Profile in Perovskite Superconductor / Ferromagnet Multilayers

J. Hoppler, J. Stahn, A. Drew, C. Niedermayer, E. Kentzinger, U. Rücker, H. Lütkens, A. Suter, T. Prokscha, E. Morenzoni, G. Cristiani, H.-U. Habermeier, B. Keimer and C. Bernhard

Swiss Physical Society Annual Meeting 2007, Zuerich, Switzerland, 21. - 22. February 2007

Interaction between Superconductivity and Magnetism in $YBa_2Cu_3O_7 / La_{2/3}Ca_{1/3}MnO_3$ Superlattices

J. Hoppler, J. Stahn, C. Niedermayer, E. Kentzinger, U. Rücker, A. Drew, A. Suter, H. Lütkens, T. Prokscha, E. Morenzoni, H.-U. Habermeier, G. Cristiani, B. Keimer and C. Bernhard

5$^{\text{th}}$ PSI Summerschool on Condensed Matter Research, Zuoz, Switzerland, 19. - 26. August 2006

List of the Experimental Instruments

Instrument:	Figures:
Morpheus, neutron reflectometer[1]	4.6, 4.7, 4.8, 4.9, 4.15, 4.16, 4.18, 4.20 and 4.23
Amor, neutron reflectometer[1]	4.4, 4.17, 4.19, 4.26, 4.28 and 4.29
Adam, neutron reflectometer[2]	4.3 *a* and 4.24
Hadas, neutron reflectometer[3]	4.10 and 4.12
C5 neutron reflectometer and diffractometer[4]	4.30 *b* - *f* and 4.33 *a* - *h*
MS Beamline, surface diffraction port[5]	4.1, 4.2 and 4.5

1) Located at SINQ at Paul Scherrer Insitut, Villigen, Switzerland
2) Located at Insitut Laue-Langevin, Grenoble, France
3) Located at FRJ-2 at Forschungszentrum Jülich, Jülich, Germany
4) Located at Canadian Neutron Beam Centre at Chalk River Laboratories, Chalk River, Canada
5) Located at SLS at Paul Scherrer Insitut, Villigen, Switzerland

Fundings

- This research project has been funded by the Schweizerische Nationalfonds zur Förderung der Wissenschaften through the grants with number 200020-119784 / 1, 200021-111690 / 1 and 206021-113057 / 1.
- This research project has been funded by the NCCR program Materials with Novel Electronic Properties MANEP.
- This research project has been supported by the European Commission under the 6th Framework Programme through the Key Action: Strengthening the European Research Area, Research Infrastructures. Contact n°: RII3-CT-2003-505925
- This research project has been funded by Paul Scherrer Institut, CH-5232 Villigen PSI, Switzerland
- This research project has been funded by the Fribourg Centre for Nanomaterials (Frimat) at the University of Fribourg and by the University of Fribourg, Switzerland.
- This research project has been funded by grant BE2684 / 1 within the Forschergruppe on cuprate high-T_c superconductors of the Deutsche Forschungsgemeinschaft (FOR 538)

Acknowledgements

The completion of this thesis would not have been possible without the contribution of a large number of persons with whom I worked, discussed or spent my time for recreation.

In the first place, I would like to thank my supervisors Christian Bernhard and Jochen Stahn for supporting me and my work in a patient and uncomplicated manner.

Explicitly, I would like to thank Christian Bernhard for giving me the opportunity to do a PhD in the open and inspiring atmosphere in his group, where I experienced an enormous freedom in doing whatever I wanted to. Further, I would like to thank him for encouraging me to travel so frequently. – I have benefited a lot during all the journeys, beamtimes, conferences, workshops and schools.

I would also like to thank explicitly Jochen Stahn for the excellent backing and co-operation since my traineeship at PSI in summer 2003. I specially appreciate his endless patience in elucidating reflectometry and the time he took for the countless discussions on all sorts of subjects. My understanding of reflectometry would not be half as deep without his support.

Since no research is possible without good samples, I would like to thank Georg Cristiani from Max Planck Institut für Festkörperforschung in Stuttgart, Germany, for the growth of the excellent samples. They are the basis of this work.

During the numberless experiments I performed on large scale facilities, I have experienced an excellent support from other researchers, beamline scientists and technicians. I am extremely thankful for their tremendous help not only during normal working hours but also on weekends, public holidays and sometimes in the middle of the night:

Bruce Patterson, Phil Willmott and Dominik Meister at the MS beamline at the SLS at PSI in Switzerland, Jochen Stahn, Christof Niedermayer, Thomas Gutberlet, Thomas Geue, Lothar Holitzner, Christian Kägi and Roman Bürge und Dominik Hohl on Amor and on Morpheus at SINQ at PSI in Switzerland, Emmanuel Kentzinger and Ulrich Rücker on Hadas at FRJ-2 in Jülich in Germany and Helmut Fritzsche in Chalk River in Canada.

Even though the data obtained at some beamlines did finally not find its way into this thesis, I would like to thank:

Elvezio Morenzoni, Thomas Prokscha, Andreas Suter, Hubertus Lütkens and Hans-Peter Weber at the Low energy muon beamline at PSI in Switzerland as well as Esther Dudzik and Ralf Feyerherm at BESSY II in Berlin in Germany for their great help.

Furthermore, I would like to thank Murat Ay, Christian Schanzer, Houssny Bouyanfif, Thomas Gutberlet, Jochen Stahn, Christian Bernhard, Christof Niedermayer, Alan Drew,

Vivek Malik, Brendan Doggett, Heon-Jung Kim and Eberhard Goering to join me for experiments.

During some of the experiments, I had the chance to experience a generous hospitality by Jochen Stahn, Emmanuel Kentzinger and Helmut Fritzsche. – I cannot tell how I appreciate that.

Mainly in the first half of my work on this thesis, I was working also on other projects and helped out during beamtimes. For the time and the experiences there I would like to thank Alan Drew and Leander Schulz as well as Vivek Malik, Christof Schneider and Brendan Doggett.

For their help for the sample characterisation, I would like to thank Vivek Malik, Matthias Rössle and Leander Schulz. A special thank concerning the help for the stress dependent magnetometry measurements is dedicated to Vivek Malik.

At PSI, I would like to thank explicitly Christof Niedermayer for backing and supporting me since my traineeship in summer 2003.

Also at PSI, I would like to thank Joël Mesot, Albert Furrer, Kurt Clausen, Hans Grimmer, Lukas Keller and Michael Horisberger and everyone from the Laboratory for Neutron Scattering for their support.

At the University of Fribourg, I would like to thank all the current and former group members which made my stay and work a pleasure. Additionally, I would like to thank Eliane Esseiva, Martial Barras, Oswald Raetzo for the technical and administrative support and Mathias Reufer and Claudia Pacholski for the great time we spent. Specially, I would like to thank Rosy Dupré for taking care of the flowers in my office during all the months I have been off to beamtimes and conferences.

Since I unfortunately the tendency have, English with a Swiss-German grammar to write, would like I Karl Zbinden for the excellent proof-reading to thank.

Besides the work environment, I am thanking my parents and Jöri & Anna for supporting me during all my career. Without their backing, I would not have finished or even started this Thesis.

Last but not least, I am thanking Surbhi for the cosy and homely life apart from work. She was always a source of motivation, inspiration and fresh energy to continue whatever I was doing.

— THANK YOU —

Curriculum Vitae

Personal Details

Name:	Hoppler
First name:	Justin
Date of birth:	November 13, 1979
Place of birth:	Bern, Switzerland
Nationality:	Swiss and French
Maritial Stauts:	Married

Studies

2006 - 2009:	Graduate student at Physics Department and Fribourg Center for Nanomaterials (FriMat), University of Fribourg, Chemin du Musée 3, CH-1700 Fribourg, Switzerland and Laboratory for Neutron Scattering, ETH Zurich & Paul Scherrer Institut, CH-5232 Villigen PSI, Switzerland
2005:	Graduation as Dipl. phil.-nat. Physiker
2004 - 2005:	Diploma work at Laboratory for Neutron Scattering, ETH Zurich & Paul Scherrer Institut, CH-5232 Villigen PSI, Switzerland
2001 - 2005:	Studies at the University of Bern, Switzerland Major: Physics Minor: Mathematics Second Minor: Geography

School

2000:	Matura Typus E
1995 - 2000:	Tertiary Education in Bern, Switzerland
1991 - 1995:	Secondary Education in Ostermundigen and Bolligen, Switzerland
1986 - 1991:	Primary Education in Ostermundigen, Switzerland

Bibliography

[1] W. Gerlach and O. Stern, Zeitschrift für Physik **9**, 349 (1922).

[2] A.H. Compton, Journal of the Franklin Institute **192**, 145 (1921).

[3] G.E. Uhlenbeck and S. Goudsmit, Nature **117**, 264 (1926).

[4] P.A.M. Dirac, Proceedings of the Royal Society of London Series A-containing Papers of a Mathematical and Physical Character **117**, 610 (1928).

[5] E. Ising, Zeitschrift für Physik **31**, 253 (1925).

[6] W. Heisenberg, Zeitschrift für Physik **49**, 619 (1928).

[7] J.C. Slater, Reviews of Modern Physics **25**, 199 (1953).

[8] E.P. Wohlfarth, Reviews of Modern Physics **25**, 211 (1953).

[9] M.B. Salamon and M. Jaime, Reviews of Modern Physics **73**, 583 (2001).

[10] H.K. Onnes, Proceedings of the Koninklijke Akademie Van Wetenschappen te Amsterdam **14**, 113 (1911).

[11] J. Bardeen, L.N. Cooper and J.R. Schrieffer, The Physical Review **108**, 1175 (1957).

[12] P.G. De Gennes, Reviews of Modern Physics **36**, 225 (1964).

[13] K.D. Usadel, Physical Review Letters **25**, 507 (1970).

[14] J.G. Bednorz and K.A. Müller, Zeitschrift für Physik B: Condensed Matter **64**, 189 (1986).

[15] Y. Kamihara, T. Watanabe, M. Hirano and H. Hosono, Journal of the American Chemical Society **130**, 3296 (2008).

[16] X.H. Chen, T. Wu, G. Wu, R.H. Liu, H. Chen and D.F. Fang, Nature **453**, 761 (2008).

[17] A.J. Drew, Ch. Niedermayer, P.J. Baker, F.L. Pratt, S.J. Blundell, T. Lancaster, R.H. Liu, G. Wu, X.H. Chen, I. Watanabe, V.K. Malik, A. Dubroka, M. Rössle, K.W. Kim, C. Baines and C. Bernhard, Nature Materials **8**, 310 (2009).

[18] H.K. Wong, B.Y. Jin, H.Q. Yang, J.B. Ketterson and J.E. Hilliard, Journal of Low Temperature Physics **63**, 307 (1986).

[19] C. Strunk, C. Sürgers, U. Paschen and H.v. Löhneysen, Physical Review B **49**, 4053 (1994).

[20] Th. Mühge, N.N. Garif'yanov, Yu.V. Goryunov, G.G. Khaliullin, L.R. Tagirov, K. Westerholt, I.A. Garifullin and H. Zabel, Physical Review Letters **77**, 1857 (1996).

[21] Z. Radović, M. Ledvij, L. Dobrosavljević-Gurjić, A.I. Buzdin and J.R. Clem, Physical Review B **44**, 759 (1991).

[22] G. Jakob, V.V. Moshchalkov and Y. Bruynseraede, Applied Physics Letters **66**, 2564 (1995).

[23] A.M. Goldman, V. Vas'ko, P. Kraus, K. Nikolaev and V.A. Larkin, Journal of Magnetism and Magnetic Materials **200**, 69 (1999).

[24] Z. Sefrioui, D. Arias, V. Peña, J.E. Villegas, M. Varela, P. Prieto, C. León, J.L. Martinez and J. Santamaria, Physical Review B **67**, 214511 (2003).

[25] T. Holden, H.-U. Habermeier, G. Cristiani, A. Golnik, A. Boris, A. Pimenov, J. Humlíček, O.I. Lebedev, G. Van Tendeloo, B. Keimer and C. Bernhard, Physical Review B **69**, 064505 (2004).

[26] N. Haberkorn, J. Guimpel, M. Sirena, L.B. Steren, W. Saldarriaga, E. Baca and M.E. Gómez, Applied Physics Letters **84**, 3927 (2004).

[27] V. Peña, Z. Sefrioui, D. Arias, C. León, J. Santamaria, J.L. Martinez, S.G.E. te Velthuis and A. Hoffmann, Phys. Rev. Lett. **94**, 057002 (2005).

[28] J. Stahn, J. Chakhalian, Ch. Niedermayer, J. Hoppler, T. Gutberlet, J. Voigt, F. Treubel, H.-U. Habermeier, G. Cristiani, B. Keimer and C. Bernhard, Physical Review B **71**, 140509(R) (2005).

[29] S. Jin, M. McCormack, T.H. Tiefel and R. Ramesh, Journal of Applied Physics **76**, 6929 (1994).

[30] F. Duan and J. Guojun, *Introduction to Condensed Matter Physics*, 1 ed. (World Scientific Publishing Co. Pte. Ltd., 5 Toh Tuck Link, Singapore 596224, 2005), Vol. 1.

[31] E. Dagotto, T. Hotta and A. Moreo, Physics Reports **344**, 1 (2001).

[32] G. Papavassiliou, M. Fardis, M. Belesi, T.G. Maris, G. Kallias, M. Pissas, D. Niarchos, C. Dimitropoulos and J. Dolinsek, Physical Review Letters **84**, 761 (2000).

[33] A. Asamitsu, Y. Moritomo, Y. Tomioka, T. Arima and Y. Tokura, Nature **373**, 407 (1995).

[34] G. Venkataiah, V. Prasad and P. Venugopal Reddy, Journal of Alloys and Compounds **429**, 1 (2006).

[35] C. Şen, G. Alvarez, H. Aliaga and E. Dagotto, Physical Review B **73**, 224441 (2006).

[36] C. Şen, G. Alvarez and E. Dagotto, Physical Review Letters **98**, 127202 (2007).

[37] E.O. Wollan and W.C. Koehler, Physical Review **100**, 545 (1955).

[38] H. Casalta, P. Schleger, P. Harris, B. Lebech, N.H. Andersen, R. Liang, P. Dosanjh and W.N. Hardy, Physica C **258**, 321 (1996).

[39] A. Damascelli, Z. Hussian and Z.-X. Shen, Reviews of Modern Physics **75**, 473 (2003).

[40] C. Bernhard and J.L. Tallon, Physical Review B **54**, 10201 (1996).

[41] J. Orenstein and A.J. Millis, Science **288**, 468 (2000).

[42] C. Bernhard, T. Holden, A. Golnik, C.T. Lin and M. Cardona, Physical Review B **62**, 9138 (2000).

[43] P. Berastegui, S.-G. Eriksson, L.-G. Johansson, M. Käll, L. Böriesson, M. Kakihana and H. Mazaki, Physica C **259**, 97 (1996).

[44] L. Yu, D. Munzar, A.V. Boris, P. Yordanov, J. Chaloupka, Th. Wolf, C.T. Lin, B. Keimer and C. Bernhard, Physical Review Letters **100**, 177004 (2008).

[45] D. van der Marel and A. Tsvetkov, Czechoslovak Journal of Physics **46**, 3165 (1996).

[46] D. Munzar, C. Bernhard, A. Golnik, J. Humlíček and M. Cardona, Solid State Communications **112**, 365 (1999).

[47] R.-H. He, K. Tanaka, S.-K. Mo, T. Sasagawa, M. Fujita, T. Adachi, N. Mannella, K. Yamada, Y. Koike, Z. Hussain and Z.-X. Shen, Nature **5**, 119 (2009).

[48] R. Blinc, B. Zalar, Valentin V. Laguta and M. Itoh, Physical Review Letters **94**, 147601 (2005).

[49] T. Ohnishi, K. Shibuya, M. Lippmaa, D. Kobayashi, H. Kumigashira, M. Oshima and H. Koinuma, Applied Physics Letters **85**, 272 (2004).

[50] Farrel W. Lytle, Journal of Applied Physics **35**, 2212 (1964).

[51] M. Itoh, R. Wang, Y. Inaguma, T. Yamaguchi and T. Nakamura, Physical Review Letters **82**, 3540 (1999).

[52] H. Uwe and T. Sakuto, Physical Review B **13**, 271 (1976).

[53] H.-B. Neumann, U. Rütt, J.R. Schneider and G. Shirane, Physical Review B **52**, 3981 (1995).

[54] R. Wang, Y. Zhu and S.M. Shapiro, Physical Review Letters **80**, 2370 (1998).

[55] K. Hirota, J.P.Hill, S.M. Shapiro, G. Shirane and Y. Fujii, Physical Review B **52**, 13195 (1995).

[56] V.K. Vlasko-Vlasov, Y.K. Lin, D.J. Miller, U. Welp, G.W.Crabtree and V.I. Nikitenko, Physical Review Letters **84**, 2239 (2000).

[57] E.D. Mishina, T.V. Misuryaev, N.E. Sherstyuk, V.V. Lemanov, A.I. Morozov, A.S. Sigov and Th. Rasing, Physical Review Letters **85**, 3664 (2000).

[58] Z. Salman, R.F. Kiefl, K.H. Chow, M.D. Hossain, T.A. Keeler, S.R. Kreitzman, C.D.P. Levy, R.I. Miller, T.J. Parolin, M.R. Pearson, H. Saadaoui, J.D. Schultz, M. Smadella, D. Wang and W.A. MacFarlane, Physical Review Letters **96**, 147601 (2006).

[59] M. Holt, M. Sutton, P. Zschack, H. Hong and T.-C. Chiang, Physical Review Letters **98**, 065501 (2007).

[60] A. Ohtomo, D.A. Muller, H.L. Grazui and H.Y. Hwang, Nature **419**, 378 (2002).

[61] A. Ohtomo and H.Y. Hwang, Nature **427**, 423 (2004).

[62] P. Fulde and R.A. Ferrell, Physical Review **135**, A550 (1964).

[63] A. I. Larkin and Y.N. Ovchinnikov, Soviet Physics Journal for Experimental and Theoretical Physics **20**, 762 (1965).

[64] L.V. Mercaldo, C. Attanasio, C. Coccorese, L. Maritato, S.L. Prischepa and M. Salvato, Physical Review B **53**, 14040 (1996).

[65] J.S. Jiang, D. Davidović, D.H. Reich and C.L. Chien, Physical Review B **54**, 6119 (1996).

[66] I. Baladié and A.I. Buzdin, Physical Review B **67**, 014523 (2003).

[67] M. Giroud, H. Courtois, K. Hasselbach, D. Mailly and B. Pannetier, Physical Review B **58**, R11872 (1998).

[68] F.S. Bergeret, A.F. Volkov and K.B. Efetov, Physical Review Letters **86**, 4096 (2001).

[69] F.S. Bergeret, A.F. Volkov and K.B. Efetov, Physical Review B **69**, 174504 (2004).

[70] F.S. Bergeret, A.F. Volkov and K.B. Efetov, Reviews of Modern Physics **77**, 1321 (2005).

[71] V.A.Vas'ko, V.A. Larkin, P.A. Kraus, K.R. Nikolaev, D.E. Grupp, C.A. Nordman and A.M. Goldman, Physical Review Letters **78**, 1134 (1997).

[72] H.-U. Habermeier and G. Cristiani, Journal of Superconductivity: Incorporating Novel Magnetism **15**, 425 (2002).

[73] W.E. Pickett and D.J. Singh, Physical Review B **53**, 1146 (1996).

[74] L.B. Steren, M. Sirena and J. Guimpel, Physical Review B **65**, 094431 (2002).

[75] B. Lake, H.M. Rønnow, N.B. Christensen, G. Aeppli, K. Lefmann, D.F. McMorrow, P. Vorderwisch, P. Smeibidl, N. Mangkorntong, T. Sasagawa, M. Nohara, H. Takagi and T.E. Mason, Nature **415**, 299 (2002).

[76] B. Lake, K. Lefmann, N.B. Christensen, G. Aeppli, D.F. McMorrow, H.M. Rønnow, P. Vorderwisch, P. Smeibidl, N. Mangkorntong, T. Sasagawa, M. Nohara and H. Takagi, Nature Materials **4**, 658 (2005).

[77] J. Chang, A.P. Schnyder, R. Gilardi, H.M. Rønnow, S. Pailhes, N.B. Christensen, Ch. Niedermayer, D.F. McMorrow, A. Hiess, A. Stunault, M. Enderle, B. Lake, O. Sobolev, N. Momono, M. Oda, M. Ido, C. Mudry and J. Mesot, Physical Review Letters **98**, 077004 (2007).

[78] L.G. Parratt, Physical Review **95**, 359 (1954).

[79] G.P. Felcher, R.O. Hilleke, R.K. Crawford, J. Haumann, R. Kleb and G. Ostrowski, Reviews of Scientific Instruments **58**, 609 (1987).

[80] G.L. Squires, *Introduction to the theory of thermal neutron scattering* (Dover Publications, Inc., 31 East 2nd Street, Mineola, N.Y.11501, 1996).

[81] P. Mikulík, Ph.D. thesis, Université Joseph Fourier, Grenoble I, 1997.

[82] U. Pietsch, V. Holý and T. Baumbach, *High-Resolution X-Ray Scattering from Thin Films to Lateral Nanostructures*, 2^{nd} ed. (Springer, ADDRESS, 2004).

[83] S.K. Sinha, E.B. Sirota, S. Garoff and H.B. Stanley, Physical Review B **38**, 2297 (1988).

[84] V. Holý, J. Kuběna, I. Ohlídal, K. Lischka and W. Plotz, Physical Review B **47**, 15896 (1993).

[85] E. Kentzinger, U. Rücker, B.P. Toperverg, F. Ott and T. Brückel, Physical Review B **77**, (2008).

[86] R. Stömmer and U. Pietsch, Journal of Physics D: Applied Physics **29**, 3161 (1996).

[87] B.P. Toperverg, in *Polarized Neutron Scattering*, Vol. 12 of *Matter and Materials*, edited by T. Brückel and W. Schweika (Forschungszentrum Jülich GmbH, 52425 Jülich, Central Library, 52425 Jülich, Germany, 2002), book Polarized Neutron Reflection and Off-Specular Scattering, pp. 249 – 288.

[88] H. Fritzsche, Z. Yamani, R. Cowley and R.C.C. Ward, Physics in Canada **62**, 265 (2006).

[89] *http://www.qdusa.com*

[90] *Pulsed Laser Deposition of Thin Films: Application-Led Growth of Functional Materials*, edited by R. Eason (John Wiley & Sons, Inc., Hoboken, New Jersey, 2007).

[91] J. Hoppler, J. Stahn, H. Bouyanfif, V.K. Malik, B.D. Patterson, P.R. Willmott, G. Cristiani, H.-U. Habermeier and C. Bernhard, Physical Review B **78**, 134111 (2008).

[92] P.R. Willmott, C.M. Schlepütz, B.D. Patterson, R. Herger, M. Lange, D. Meister, D. Maden, Ch. Brönnimann, E.F. Eikenberry, G. Hülsen and A. Al-Adwan, Applied Surface Science **247**, 188 (2005).

[93] J. Chakhalian, J.W. Freeland, G. Srajer, J. Strempfer, G. Khaliullin, J.C. Cezar, T. Charlton, R. Dalgliesh, C. Bernhard, G. Cristiani, H.-U. Habermeier and B. Keimer, Nature Physics **2**, 244 (2006).

[94] W. Luo, S.J. Pennycook and S.T. Pantelides, Physical Review Letters **101**, 247204 (2008).

[95] J. Chakhalian, J.W. Freeland, H.-U. Habermeier, G. Cristiani, G. Khaliullin, M. van Veenendaal and B. Keimer, Science **318**, 1114 (2007).

[96] J. Hoppler, J. Stahn, Ch. Niedermayer, V.K. Malik, H. Bouyanfif, A.J. Drew, M. Rössle, A. Buzdin, G. Cristiani, H.-U. Habermeier, B. Keimer and C. Bernhard, Nature Materials **8**, 315 (2009).

[97] H. Fritzsche, Reviews of Scientific Instruments **76**, 115104 (2005).

[98] F. Radu, V. Leiner, M. Wolff, V.K. Ignatovich and H. Zabel, Physical Review B **71**, 214423 (2005).

[99] N.M. Nemes, M. García-Hernández, S.G.E. te Velthuis, A. Hoffmann, C. Visani, J. Garcia-Barriocanal, V. Peña, D. Arias, Z. Sefrioui, C. León and J. Santamaría, Physical Review B **78**, (2008).